Title
Ion solvation at air-water interfaces

Author
Shaffer, Patrick R.

Publication Date
2013

Peer reviewed|Thesis/dissertation

Ion solvation at air-water interfaces

by

Patrick Robert Shaffer

A dissertation submitted in partial satisfaction of the
requirements for the degree of
Doctor of Philosophy

in

Chemistry

in the

Graduate Division

of the

University of California, Berkeley

Committee in charge:

Professor Phillip Lewis Geissler, Chair
Professor Rich Saykally
Professor Clayton Radke

Fall 2013

Ion solvation at air-water interfaces

Abstract

Ion solvation at air-water interfaces

by

Patrick Robert Shaffer

Doctor of Philosophy in Chemistry

University of California, Berkeley

Professor Phillip Lewis Geissler, Chair

In this thesis we conduct a thorough study of the forces that act on ions when they are near air-water interfaces. These forces are important because they produce behavior which is very ion specific. That is, certain ions have a strong propensity for air-water interfaces and other ions avoid them completely. We will see that the dominant forces that allow ion adsorption to surfaces are fairly general and exist in a very broad class of liquids, so that even ions in a very simple model of a polar fluid exhibit a preference for the surface. In models of water, however, there are also forces which are very ion specific. In particular, the degree to which an ion is surface enhanced or surface repelled is very dependent on the sign of the charge. We will conduct a thorough study of this charge asymmetry in a simulated model of water and find that it is sensitive to various model details like ion size, the magnitude of the charge and polarizability. We will also study the way that solvent polarizability renormalizes the interactions between a pair of ions in solution, and a pair of ions at the interface and we will find that a simple effective model is fairly good at capturing the effects of polarizability. Finally, we will discuss attempts to improve dielectric continuum theory so that it is more useful for studying problems that involve solutes at interfaces.

In memory of Christopher Shaffer

Contents

List of Figures

List of Tables

Acknowledgments

The work described in this dissertation has been made possible thanks to the support and guidance of many people. First and foremost among these people is my advisor, Professor Phill Geissler. Phill has been the ideal mentor, role model and friend. He has taught me that the best science is inspired by curiosity and that your job as a scientist is by no means complete until you've figured out how to communicate what you've learned very clearly. Professor Rich Saykally has been a bottomless source of ideas and advice, I regret that I wasn't able to explore all the questions he passed my way.

I am extremely grateful to have learned from a number of senior grad students and postdocs in the Pitzer center when I joined Phill's group. Joyce Noah-Vanhoucke, Lutz Maibaum, Will Browne, Brian Gin, Michael Gruenwald, Jiyeon Ku, Adam Willard, Lester Hedges and Amish Patel all made those difficult early years much easier and many of them continue to be reliable sources of advice, even after they've moved on. In my later years I was lucky to have Suri Vaikuntanathan as a mentor. I feel especially thankful for the many close friends I've made among my peers. Ayelet Benjamini, Todd Gingrich, Anna Schneider, David Limmer, Eric Sundstrom, Patrick Varilly, Chris Ryan and I have shared many of the same disappointments and successes over the past several years, which made the successes sweeter and the disappointments easier to bear.

The love and support of my family has been indispensable and inexhaustible. I can easily imagine how having a child do a PhD can be difficult for the sort of extremely loving and attentive parents that I have. Having a child far away, working for many years with few visible signs of progress might make any parent have doubts about their son's choices. My parents never had any doubt in me, and even encouraged me to take my time. I am very proud to now have a degree to show them, and I'm sorry to have chosen a slightly inaccessible field. My sister Kathleen and brother-in-law Brad helped me get situated in Berkeley and it was such a huge relief to have a piece of my family so close by during my first two years in Berkeley. My brothers Matt and Chris have always inspired me. I trace my interest in science to early lessons from my older brother Chris. I remember peering into a microscope and discussing how gravity works with him when I was in elementary school. It brings me immense sadness that I cannot share my achievement with him.

Finally, Hoppy Maffione has been the most patient and loving of girlfriends for the past two years. I know that this has been as hard for you as it has been for me and I feel tremendous gratitude for your sacrifices.

Chapter 1

Introduction

1.1 Early examples of specific ion effects

There are many properties of aqueous electrolyte solutions that have a pronounced ion-specificity. Furthermore, there are large collections of these properties for which the same, or almost the same, ordering of ions dictates the strength of the ion-specific effect. Chemical specificity is of course not surprising when it involves chemical transformations of some sort. However many of these properties involve no chemistry at all. Prototypical examples are surface tensions of solutions and protein solubility, however there is an entire zoo of effects which we ordinarily would not group together were it not for the fact that they obey the same ordering of ions. More exotic examples include bubble coalescence inhibition and phase behavior of micro emulsions, which exhibit extraordinary sensitivity to even trace amounts of salts ([39, 21, 19, 20]). This ordering is known as the Hofmeister series. Studies of these effects date back to 1888 when Franz Hofmeister looked at the dependence of protein solubility on which salts were in solution [33]. The ordering for anions is as follows:

$$SO_4^{2-} > HPO_4^{2-} > Cl^- > NO_3^- > Br^- > ClO_3^- > I^- > SCN^-, \tag{1.1}$$

and the ordering for cations is given by:

$$NH_4^+ > K^+ > Na^+ > LI^+ > Mg^{2+} > Ca^{2+}. \tag{1.2}$$

One common ingredient underlying many of the Hofmeister effects is the presence of an interface, such as an interface between liquid water and air, liquid water and a protein, or liquid water and a hydrophobic colloid. About 10 years ago it became clear that there is a major gap in our understanding of the way that salts interact with such interfaces. Experiments on the uptake of halogen gases by aqueous aerosols suggested that there must be some halide ions present at the interface [22], and Jungwirth and Tobias showed that certain ions in simulated solutions exhibit a pronounced preference for the interface between the liquid and the vapor phase [62]. This observation came as a surprise because it is starkly

at odds with dielectric continuum theory, which provides us with perhaps the simplest way of thinking about the forces that dictate interactions between ions and interfaces.

1.2 Dielectric continuum theory (DCT) as a simple framework

In a dielectric medium with dielectric constant ϵ_1, and a charge density $\rho(r)$, the electrostatic potential must satisfy Poisson's equation:

$$\nabla^2\phi(r) = -\frac{4\pi\rho(r)}{\epsilon_1}. \tag{1.3}$$

For a delta function charge distribution where $\rho(r) = q\delta(r - r')$ the well known solution to this is just $\phi(r, r') = \frac{q}{\epsilon_1|r-r'|}$, which illustrates the simple fact that that a dielectric medium has the effect of screening electrostatic forces by a factor of ϵ_1^{-1}. If there is a flat, infinite, boundary between a medium of dielectric constant ϵ_1 and a medium of dielectric constant ϵ_2, Gauss's law demands that the the components of the electric field normal to the surface satisfy:

$$\lim_{z\to 0^-} \epsilon_1 E_z(r) = \lim_{z\to 0^+} \epsilon_2 E_z(r), \tag{1.4}$$

where E_z is the z component of the electric field. This boundary condition, together with the condition that the curl of the electric field vanishes, is uniquely satisfied by an image charge. To be explicit, the electrostatic potential due to a charge at position z is:

$$\phi(r) = \frac{q}{\epsilon_1|r - z|} + \frac{q'}{\epsilon_1|r - z'|}, \tag{1.5}$$

where z', is point z reflected through the boundary. If we apply this description to the air water interface we have $\epsilon_1 = 80$ and $\epsilon_2 = 1$, in which case the magnitude of the image charge is $q' = \frac{q(80-1)}{80+1} \simeq q$. The image charge then has the effect of repelling the charge from the surface. The energy required to move the charge from infinitely far way to a distance z from the surface is (see Fig. 1.1b):

$$W(z) = \frac{\epsilon_1 - 1}{\epsilon_1(\epsilon_1 + 1)}\frac{q^2}{2z}. \tag{1.6}$$

This treatment clearly involves several approximations. One such approximation is that it entirely neglects the finite size of the ion. We expect this to be a safe approximation if the spatial range of interactions between the ion and solvent is large compared to the size of the ion. This separation of length scales was unquestioned for many years, but these length scales are in fact commensurate for realistic ion sizes in water. We will discuss in detail how this assumption breaks down, and how that breakdown leads to qualitative failure of the DCT description above.

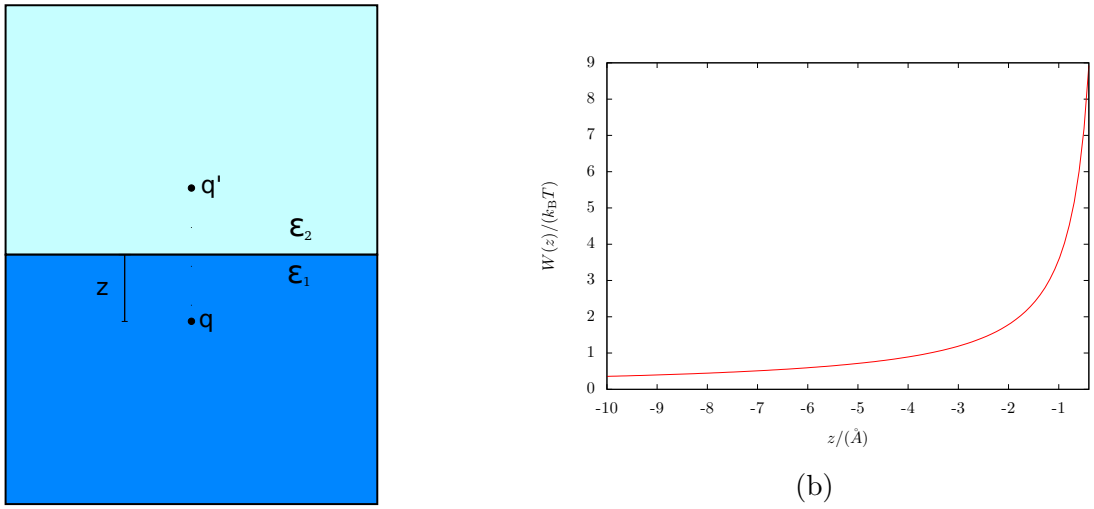

(a) (b)

Figure 1.1: A schematic illustration of the boundary between two dielectric media. The field due to the charge q is augmented by the image charge q'. If we assume that $\epsilon_1 = 80$ and $\epsilon_2 = 1$, which mimics a water-vapor interface, then the charge q is repelled from the interface as in (b), see Eq. 1.6

Another flaw in the above treatment is that it entirely neglects interactions between ions. Including these interactions, even in a very approximate way, restores charge neutrality and rectifies the spurious prediction of an infinite negative surface adsorption. This infinite negative surface adsorption makes thermodynamically unrealistic predictions via the Gibbs adsorption isotherm. To see how this problem arises, consider what would happen if we had a solution of ions interacting with an interface according Eq. 1.6, with $q^+ = -q^- = 1$. The density profiles of either species would be

$$\rho^+(z) = \rho^-(z) = \exp[-\beta \frac{q^2}{\epsilon_1 2z}], \tag{1.7}$$

where I have adopted the approximation $\frac{\epsilon-1}{\epsilon+1} = 1$. The surface adsorption is an example of a surface excess quantity. Surface excesses arise whenever we consider two bulk homogeneous phases, α and β separated by an interface. For any extensive quantity X, it's surface excess is defined as:

$$X^s = X - X^\alpha - X^\beta. \tag{1.8}$$

This equation requires us to define X^α and X^β. The traditional approach is to imagine that there is a mathematical dividing surface between phases α and β, and then to define X^α and X^β by assuming that the two phases maintain their bulk properties right up to this surface, see [11]. We can make any choice we like, but one natural choice is where the surface excess

of the number of particles is zero. This choice is known as the Gibbs dividing surface, and in general we can only satisfy this constraint for a single component (typically the solvent), while other components will have a nonvanishing surface excess of number of particles (or surface adsorption). If we know the density profiles $\rho^+(z)$ or $\rho^-(z)$, we can compute the surface adsorption as follows:

$$n^+ = \int_{-\infty}^{0} dz[\rho^+(z) - \rho_l^+] + \int_0^{\infty} dz[\rho^+(z) - \rho_v^+]. \tag{1.9}$$

Where we've chosen $z = 0$ as the Gibbs dividing surface, and ρ_l and ρ_v are the bulk liquid and vapor densities. To satisfy charge neutrality the anion and cation surface adsorptions must be the same. The Gibbs adsorption isotherm relates this quantity to the surface tension in a simple way:

$$\frac{d\gamma}{d\mu} = -\frac{2n^+}{A}. \tag{1.10}$$

This equation says that if a component has a positive surface excess then the surface tension will drop when you increase it's concentration and it the surface excess is negative the surface tension will go up. The density profile predicted by Eq. 1.7, has a surface excess of $-\infty$, which has clearly non-physical consequences.

Onsager and Samaras studied this problem in 1934 and showed that this problem can be resolved by including interactions between ions at a mean field level [44]. The standard electrostatic mean field theory for studying electrolyte solutions is Poisson-Boltzmann theory. In this theory we assume that the charge density satisfies

$$\rho(r) = \exp[-\beta q\phi(r)]\rho_o. \tag{1.11}$$

Where for simplicity we don't distinguish between the positive and negative component of the charge density. The electrostatic potential, furthermore, must satisfy the Poisson equation (Eq. 1.3). Combining these two equations gives us the Poisson-Boltzmann equation

$$\nabla^2\phi(r) = -\frac{4\pi \exp[-\beta q\phi(r)]\rho_o}{\epsilon_1} \tag{1.12}$$

Onsager and Samaras studied a linearized version of this in which we make the substitution $\exp[-\beta q\phi(r)] \simeq 1 - \beta q\phi(r)$. Solving this equation analytically with the boundary condition 1.4 requires even more approximations still, but the end result is agreeable in the sense that it predicts finite (negative) surface adsorptions and hence positive surface tension increments. The original density profiles obtained by Onsager and Samaras are shown in Fig. 1.2. The limiting law they derived predicts that the surface tension increases proportionally to $c\ln(c)$ in the low concentration regime where c is simply the electrolyte concentration, not the activity.

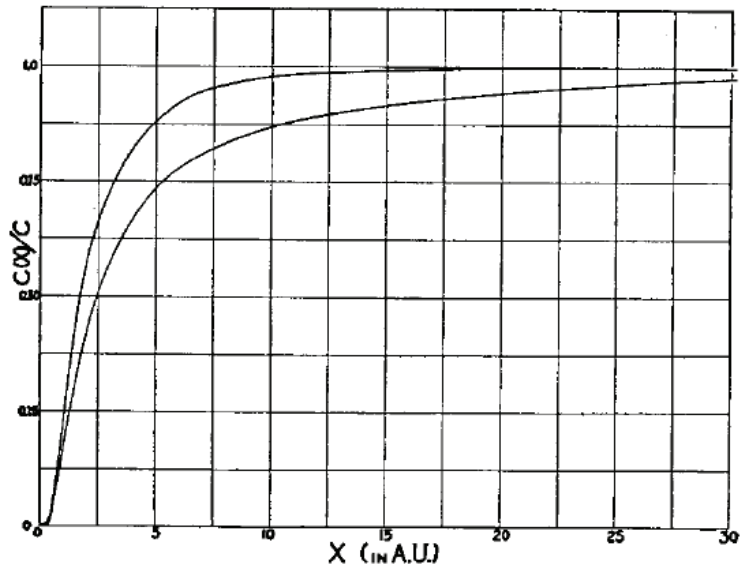

FIG. 2. Density distribution in the interface region for uni-univalent electrolytes. The concentrations are 0.1 mol./l. (upper curve) and 0.001 mol./l.

Figure 1.2: Original density profiles obtained by Onsager and Samaras in 1934. The positive x axis here indicates distance below the air-water interface. See [44]

1.3 Experiments challenge the traditional view

Onsager and Samaras were quick to acknowledge that their treatment involves several layers of approximations, and probably would not be valid above 0.2 M. However, within a few years there was evidence that even at low concentrations, this theory made qualitatively incorrect predictions. Jones and Ray published a famous set of surface tension measurements in which they showed that at low concentrations certain salts actually decrease the surface tension [48]. These data were controversial for a very long time, and even today it is considered difficult to accurately measure surface tension increments at low concentrations. However, were these results accurate, it would unambiguously imply that certain ions have a positive surface adsorption at low concentration. The surface tensions as a function of concentration for the 13 Jones-Ray salts are shown in Fig. 1.3.

Although a positive surface adsorption does imply that ions are present in enhanced concentrations at interfaces, it is now well understood that a negative surface adsorption does

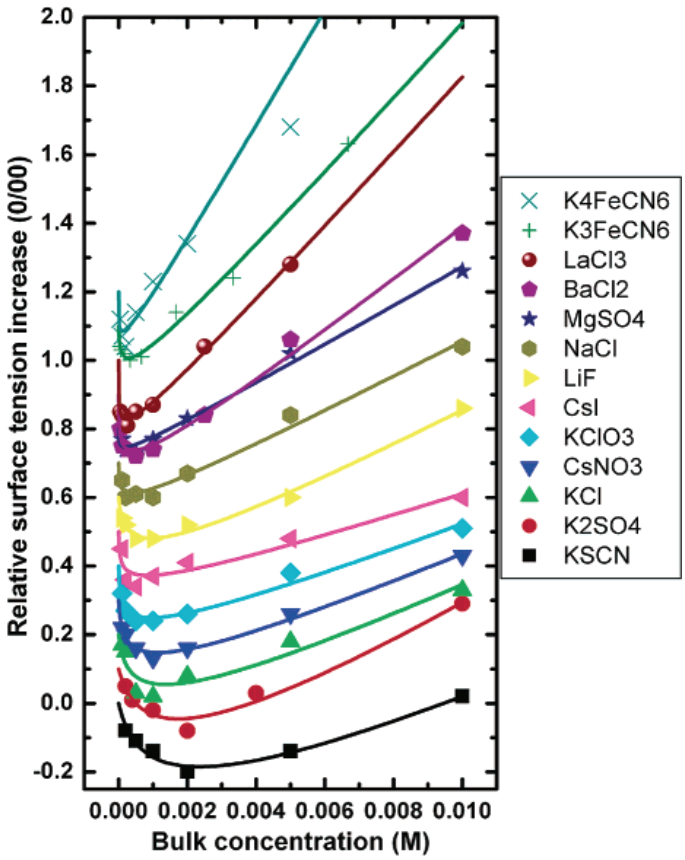

Figure 1.3: Liquid vapor surface tensions as a function of salt concentration from [48]

.

not necessarily imply the absence of ions from interfaces. The ion density profiles can be such that there is a subsurface depletion layer below a surface enhanced layer so that the overall surface adsorption is negative, and such cases are indeed seen in simulations [30]. This is not to imply that the simulated surface adsorptions are always consistent with experiments. Bhatt et al. have shown that low concentrations of NaCl and NaBr in simulations have negative surface adsorptions, whereas higher concentrations of each salt have positive surface adsorptions. This implies that the surface tensions of these solutions have a maximum as a function of concentration which, as the authors note, is not seen in experiments [6]. These studies expose the fact that simulations are still not a completely reliable guide when it comes to interpreting macroscopic measurements like the surface tension.

A more sophisticated set of experiments have become possible over the past 20 years that allow one to investigate the structure of the interface more directly using second order spectroscopies. Shen and coworkers first pointed out the utility of a second order spectroscopy as a surface sensitive probe [15]. In these experiments, you measure radiation from the polarization response to a pair of incident electric fields of different frequencies. This response

is described by the equation

$$P^2 \propto \chi^2 E_1 E_2. \tag{1.13}$$

In a medium with inversion symmetry, inverting the electric field will invert the polarization field. If we call the inverted polarization field P_i^2 this means that $P_i^2 = -P^2$ and

$$P_i^2 = \chi^2(-E_1)(-E_2) = \chi^2 E_1 E_2 = P^2. \tag{1.14}$$

Which means that

$$P^2 = -P^2, \tag{1.15}$$

so the polarization field must vanish when there is inversion symmetry. For systems with bulk inversion symmetry like liquid water, measuring the 2nd order response will therefore isolate a signal from the interface.

One of the most popular second order techniques for probing the air-water interface is sum frequency generation (SFG) spectroscopy. SFG studies measure the OH stretch of water molecules in the interfacial region. SFG cannot measure the presence of ions directly, but the SFG spectrum is very sensitive to the ions in solution. NaF, for example, does not affect the SFG spectrum at all, whereas NaI produces noticeable changes in the SFG signal [36]. Interpreting these signals is a very difficult problem but the relevant changes are unlikely to arise from the influence of the ion on it's immediate neighbors. It is more likely the case that the ion density polarizes the slightly subsurface layers [42].

Another class of experiments involves a technique called second harmonic generation (SHG) spectroscopy. This technique can be used to directly study a certain set of anions that have a charge-transfer-to-solvent transition in the UV. These anions include I- and SCN- and these produce an SHG signal which is proportional to the surface concentration [49, 45, 48]. SHG studies have been used to obtain an effective adsorption free energy by measuring the SHG signal as a function of concentration and fitting to a Langmuir adsorption isotherm [50, 46]. SHG experiments have presented the most convincing evidence that there are in fact ions at surfaces, and that their concentrations at the surface exceed their bulk concentrations.

1.4 Overview

The rest of this thesis is a thorough study of the forces that dictate the behavior of ions at interfaces. In chapter 2 we study in detail the thermodynamics of ion adsorption to interfaces. We find that there are certain thermodynamic trends associated with ion adsorption that are very general and we investigate the mechanisms underlying these trends. In chapter 3 we take a close look at what makes the forces that drive ions towards and away from interfaces so specific. In particular, we address the question of how anions are different from cations as far as their interactions with interfaces are concerned. In chapter 4

we study how solvent polarizability renormalizes the interactions between ions, particularly when those ions are near or at an interface. Chapter 5 is a discussion of ongoing work to improve the utility of dielectric continuum theory for studying systems with interfaces.

Chapter 2

General features of ion solvation at interfaces

2.1 Models and methods

Solvent models

As we saw in the last chapter, we will require a more detailed model than dielectric continuum theory to capture the interesting behavior of ions at interfaces. We will consider in detail two distinct atomistic solvent models. The first of these is the SPC/E water model. This model was developed in 1987 by Berendsen and coworkers [5]. It caricatures the charge distribution of a water molecule with positive charges of .4238 on each hydrogen atom and a negative charge of .8476 on each oxygen atom. It has a lennard-jones potential centered on the oxygen atom with lj parameters of $\sigma = 3.166\mathring{A}$ and $\epsilon = 0.650kj/mol$. This model is widely used and is particularly popular in studies of ion solvation [38, 24, 41].

The second solvent model we use is known as the Stockmayer solvent. The Stockmayer potential is merely a Lennard-Jones potential where each LJ particle center has a fixed permanent dipole. This model allows us to study ion solvation in a slightly simpler context than the SPC/E water model. Stockmayer parameters can be chosen so that it has a dielectric constant comparable to liquid water, but it is always distinct from water in that it has perfect charge inversion symmetry. This means that solvation of anions and cations is necessarily identical, both in bulk and near interfaces. Stockmayer liquids are also distinct from water in that they do not have hydrogen bonding. The interaction of ions with the hydrogen bonding network has important consequences for both bulk and interfacial solvation (see chapter 3), but these details are absent in Stockmayer which allows us to study features of ion adsorption in a much simpler context.

Sampling schemes

Studying the statistical mechanics of these models requires us to sample configurations from a Boltzmann distribution. The approach we use is a straightforward Metropolis Monte Carlo scheme. This objective of this scheme is to carry out a Markovian walk on the configuration space r such that the stationary probability distribution $P(r) = \exp[-\beta U(r)]$ is preserved. In order to preserve this probability distribution it must be the case that the fluxes into and out of state r are the same. The simplest way to guarantee this is to enforce a detailed balance criteria where the flux from state r to r' is the same as the flux from state r' to r. These fluxes, which I will call $k(r \to r')$, are a simple product of the probability that the system is in the original state times the probability that the system makes a transition to r', given that it started in r. This transition probability is composed of two parts, the probability of proposing the move $w(r \to r')$, and the probability of accepting the move $\alpha(r \to r')$. The detailed balance criteria is then:

$$P(r)w(r \to r')\alpha(r \to r') = P(r')w(r' \to r)\alpha(r' \to r). \tag{2.1}$$

If the proposal probabilities are symmetric in r and r' so that $w(r' \to r) = w(r \to r')$, the above equation simplifies to:

$$\frac{\alpha(r \to r')}{\alpha(r' \to r)} = \frac{P(r')}{P(r)} \tag{2.2}$$

This condition can be satisfied in many ways but one popular choice is:

$$\alpha(r \to r') = min[1, \exp[-\beta(U(r) - U(r'))]. \tag{2.3}$$

For the simple molecular systems we study we only propose single particle moves that update the configuration and position of a single, randomly chosen molecule at a time. For a detailed discussion of monte carlo algorithms see [17, 1].

All the simulations described in this chapter consist of a single ion embedded in a liquid slab at coexistence with its vapor. Electroneutrality is maintained by having a uniform background charge density. To satisfy periodic boundary conditions, the slab must have two liquid vapor interfaces, which by symmetry interact with the ion in identical ways. We will calculate various quantities that are a function of the distance between the ion and the liquid vapor interface. We do this by imposing constraints on the ion that require it to be in a certain height window, where the height is referenced to the center of mass of the slab. These constraints take the form of a hard wall where we reject any moves that take the ion outside of some lower bound z_{min} or upper bound z_{max}. Certain calculations in this chapter will involve making this window very narrow ($\simeq 0.05\mathring{A}$), and collecting data on the ensemble where the ion is at a specific height. In the other set of calculations we will allow the ion to diffuse in a set of larger overlapping height windows. We then combine the data from these windows using the MBAR equations to compute the ion density profile as a function of height. The MBAR equations are a statistically optimal way of estimating the

free energy differences between ensembles with different bias potentials, and for constructing the probability distribution for the unbiased ensemble. We will here present a brief discussion of the MBAR procedure which is based on the excellent and very complete discussion in [61], for the original derivation of these equations see [55]. Say we are interested in the statistics of some variable z and we sample this variable in K ensembles with different bias potentials $V_k(z)$. The results of this sampling are a collection of discrete values of z. The nth value of z obtained in the jth ensemble is $z_{n,j}$. We adopt the following model for the full probability distribution of z:

$$P(z) = Z^{-1} \sum_{j=1}^{K} \sum_{n=1}^{N_K} p_{n,j} \delta(z - z_{n,j}). \tag{2.4}$$

This probability distribution depends on the weights, $p_{n,j}$, and these weights are determined from the following equation:

$$\frac{p_{n,j}}{Z} = \frac{1}{\sum_{l=1}^{K} N_l \exp[\beta \Delta F_l - \beta V_l(z_{n,j})]}. \tag{2.5}$$

The free energy differences between the different ensembles ΔF_k are determined self consistently from the K equations,

$$\Delta F_i = -k_{\mathrm{B}} T \ln \left[\sum_{j=1}^{K} \sum_{n=1}^{N_j} \frac{\exp[-\beta V_i(z_{n,j})}{\sum_{l=1}^{K} N_l \exp[\beta \Delta F_l - \beta V_l(z_{n,j})]} \right]. \tag{2.6}$$

Once we solve these equations we can reconstruct the full probability distribution using equation 2.4. For our specific case the coordinate z will be the height of the ion and the bias potentials $V_k(z)$ will be hard wall potentials, which are infinity outside of some limits and zero everywhere else.

The simulations of SPC/E water all consisted of 252 solvent molecules in a box of $20\mathring{A}$x $20\mathring{A}$x$40\mathring{A}$ and were conducted at 300 K. Electrostatic energies were computed by the Ewald method using a convergence parameter $\alpha = 0.0784\mathring{A}$ and 10 wave vectors in the x and y dimensions along with 20 wave vectors in the z direction.

Stockmayer simulations consisted of 240 solvent particles in a box with dimensions 6.7σx6.7σx13.4σ. The Lennard-Jones parameter σ defines the length scale and the LJ parameter ϵ defines the energy scale. In terms of these units the natural unit of a dipole is $\mu^* = \sqrt{4\pi\epsilon_o\sigma^3\epsilon}$. The Stockmayer system we simulate has a dipole of $\mu = 1.5\mu^*$ and all simulations are conducted at a temperature of $T = 0.7\epsilon/k_{\mathrm{B}}$.

2.2 Competing forces in ion hydration

For simple ions it is natural to think of ion solvation thermodynamics in terms of two distinct steps. The first of these is cavity formation and the second of these is charging.

We can arrive at this decomposition from the exact statistical mechanical expression for solvation free energy as we will now show. Consider a system consisting of a single charged solute at position z, interacting with N solvent molecules. It has a potential energy that takes the form:

$$U(r^N) = U_{ss}(r^N) + U_{is}^{vdW}(r^N) + q\phi(r^N), \tag{2.7}$$

where U_{ss} describes the interaction between solvent molecules U_{is}^{vdW} is the non electrostatic component of the solute-solvent interaction, and ϕ is the electrostatic potential at z due to solvent molecules at positions r^N. We can write down the canonical partition function given this potential energy:

$$Z(z) \propto \int dr^N \exp[-\beta U_{ss}(r^N) - \beta U_{is}^{vdW}(r^N) - \beta q\phi(r^N; z)]. \tag{2.8}$$

If we insert a delta function and manipulate further we obtain a formula that highlights the role of the distribution of the potential inside a cavity,

$$Z(z) \propto \int d\phi' \int dr^N \delta(\phi' - \phi(r^N; z)) \exp[-\beta U_{ss}(r^N) - \beta U_{is}^{vdW}(r^N; z) - \beta q\phi'] \tag{2.9}$$

$$Z(z) \propto \int d\phi' \exp[-\beta q\phi')] \int dr^N \delta(\phi' - \phi(r^N; z)) \exp[-\beta U_{ss}(r^N) - \beta U_{is}^{vdW}(r^N; z)] \tag{2.10}$$

$$Z(z) \propto \int d\phi' \exp[-\beta q\phi'(r^N)] P_o(\phi'; z) Z_{uc}(z), \tag{2.11}$$

where $P_o(\phi')$ is the distribution of the electrostatic potential inside an uncharged solute and Z_{uc} is the partition function for the uncharged solute-solvent system. To make this more physically transparent, consider the ratio Z_{uc}/Z_o, where Z_o is the partition function of the solvent:

$$\frac{Z_{uc}(z)}{Z_o} = \frac{\int dr^N \exp[-\beta U_{ss}(r^N) - \beta U_{is}^{vdW}(r^N; z)]}{\int dr^N \exp[-\beta U_{ss}(r^N)]} = \langle \exp[-\beta U_{is}^{vdW}(r^N; z)] \rangle \tag{2.12}$$

This equation is known as the potential distribution theorem. We have not been specific about the form of U_{is}^{vdW}, but if it is a hard core repulsion then this last equation measures the probability that there are no solvent molecules inside of a solute sized cavity at z ($P_{cav}(N = 0; z)$). Rewriting eq. 6 we find:

$$Z(z) \propto \int d\phi' P_o(\phi'; z) \exp[-\beta q\phi'(r^N)] P_{cav}(N = 0; z) Z_o \tag{2.13}$$

$$F(z) = -k_B T \ln[Z(z)] \tag{2.14}$$

$$F(z) = -k_B T \left[\ln[P_{cav}(N = 0; z)] + \ln \int d\phi' P_o(\phi'; z) \exp[-\beta q\phi'] + \ln Z_o \right] \tag{2.15}$$

The first two terms in eq. 2.15 are the two physically distinct parts of the excess chemical potential. The first is the cavity formation free energy (F_{cav}), and the second is the free energy associated with endowing the cavity with a charge (F_{es}). To be explicit these quantities are

$$F_{cav} = -k_B T \ln[P_{cav}(N = 0; z)] \tag{2.16}$$

and

$$F_{es} = -k_B T \ln \int d\phi' P_o(\phi'; z) \exp[-\beta q \phi'] \tag{2.17}$$

The details of the cavity formation free energy are fairly well understood because these details underlie the hydrophobic effect. This behavior depends on the cavity size R in important ways and successful theories of the hydrophobic effect describe this length scale dependence very accurately [9, 37, 47]. For small cavity sizes, the probability that you will find N molecules inside the cavity, $P_{cav}(N)$ is Gaussian to a very good approximation (see ref. [23] and fig 2.1), and all we need to know to determine $P_{cav}(N = 0)$ is the variance and the mean of this distribution. The mean is clearly given by

$$\langle N \rangle = \rho_l v \tag{2.18}$$

where ρ_l is the bulk liquid phase density and v is the volume of the cavity. The variance is determined from the radial distribution function as:

$$\langle (\delta N)^2 \rangle = \rho_l v + \int_{r \in v} \int_{r' \in v} \rho_l^2 [g(r, r') - 1]. \tag{2.19}$$

In a straightforward manipulation of eq. 2.16 we can then show that

$$F_{cav} = \frac{k_B T}{2} \ln[2\pi \langle (\delta N)^2 \rangle] + \frac{k_B T \langle N \rangle^2}{2 \langle (\delta N)^2 \rangle}. \tag{2.20}$$

This equation provides a very accurate prediction of solvation free energies of ideal solutes with excluding volume radii up to 4 $\mathring{A}$ [23]. The failure of this equation is a sign that something collective is happening. Gaussian behavior of a fluctuating variable is a sign that that variable is statistically the sum of many independent events. When cavity sizes are large enough, it is much easier to evacuate the cavity by locally inducing a phase transition and forming a liquid-vapor interface than it is to add up all those independent events. When a liquid vapor interface forms the solvation free energy is substantially lower than predicted by eq. 2.20. In liquid water at ambient conditions this crossover happens somewhere around 1 nm. Above this length scale F_{cav} scales with the surface area of the cavity, where the proportionality constant is roughly the liquid-vapor surface tension. However, there is another thermodynamic signature of this crossover, which is that for short length scales the F_{cav} has a negative entropic component whereas for larger length scales this component is positive. That is, it is entropically costly to exclude small volumes, but entropically favorable to exclude large volumes. These two features are illustrated in fig. 2.2 adopted from ref. [10].

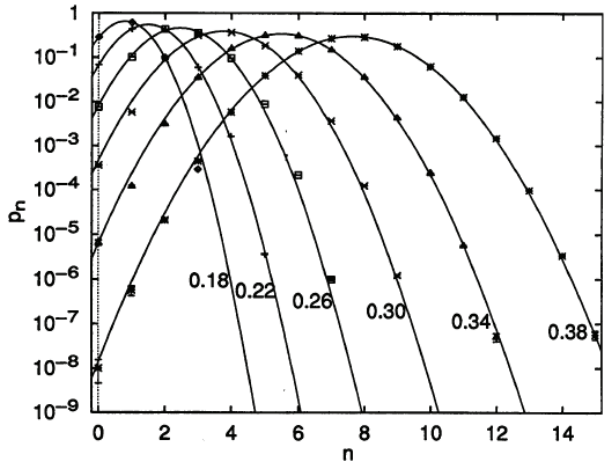

Figure 2.1: $P_{cav}(N)$ in bulk for various different cavity sizes (indicated in nanometers by the number next to the curve) taken from ref. [23], These are remarkably gaussian all the way down to $N = 0$.

Regardless of the length scale, the cavity formation free energy is always a force that would tend to drive solutes towards the vapor phase. We are mostly interested in ions that have cavity sizes in the small hydrophobe regime, which means that cavity formation has a negative entropic component, and this entropic cost ought to be alleviated when the ion moves to the interface. Fig. 2.3 shows explicitly cavity formation free energy as the ion moves across the surface, along with its energetic and entropic components. The energetic component is clearly decreasing as the solute approaches the interface and the entropic component is clearly increasing.

The second part of the solvation free energy is the charging free energy F_{es}. As we can see from equation 3.1 this quantity can be expressed in terms of the distribution of the potential inside the uncharged cavity. Empirically it is found that we can approximate this distribution as a gaussian with reasonable accuracy [24, 38]. Fig. 2.4 shows this probability distribution for a cavity with an excluded volume radius of 3.3 $\mathring{A}$ in bulk, along with the gaussian approximation to this distribution.

If we adopt the Gaussian approximation the charging free energy follows from a simple formula:

$$F_{es}(z,q) \simeq q\langle\phi\rangle(z) - \frac{1}{2}\beta q^2\langle(\delta\phi)^2\rangle(z) = F_{gauss}(z,q), \tag{2.21}$$

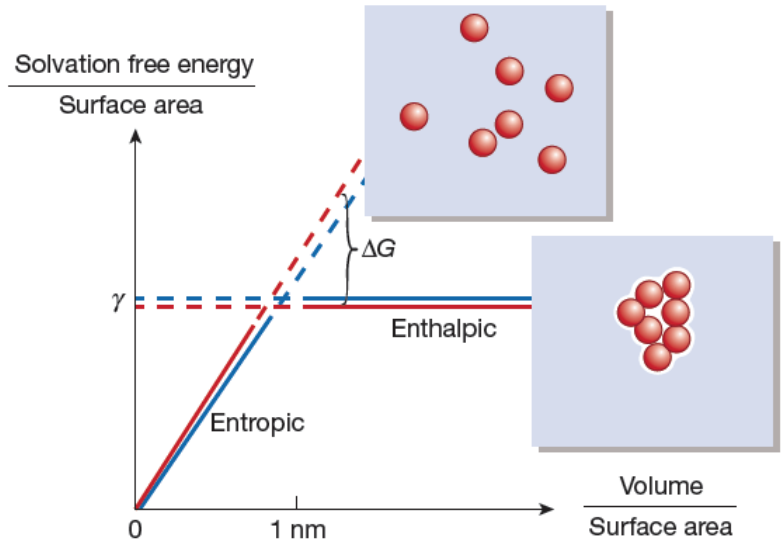

Figure 2.2: The hydrophobic crossover as illustrated in ref. [10]. At small length scales the solvation free energy scales with volume and goes up as you raise the temperature, indicating a negative entropy of solvation

.

where $\langle\phi\rangle$ and $\langle(\delta\phi)^2\rangle$ are the mean and variance of the electrostatic potential in an uncharged cavity. These quantities can of course be measured in a simulation, but they can also be estimated from dielectric continuum theory (see chapter 5). Figure 2.5 shows the charging free energy along with the gaussian approximation for the same 3.3 $\mathring{A}$ cavity studied in fig. 2.3, while the ion is in bulk. I have not decomposed this into energetic and entropic components but this decomposition has been studied and the entropy is quite small compared to the energy [38].

The energy scales associated with this charging free energy are clearly not concomitant with the energy scales associated with the cavity formation. Even at a relatively modest charge of 0.5 the charging free energy is nearly 100 kj/mol, all of which must be lost if the ion is removed from solution. It's difficult to imagine these two forces competing with one another in a way that ultimately stabilizes the ion at the interface.

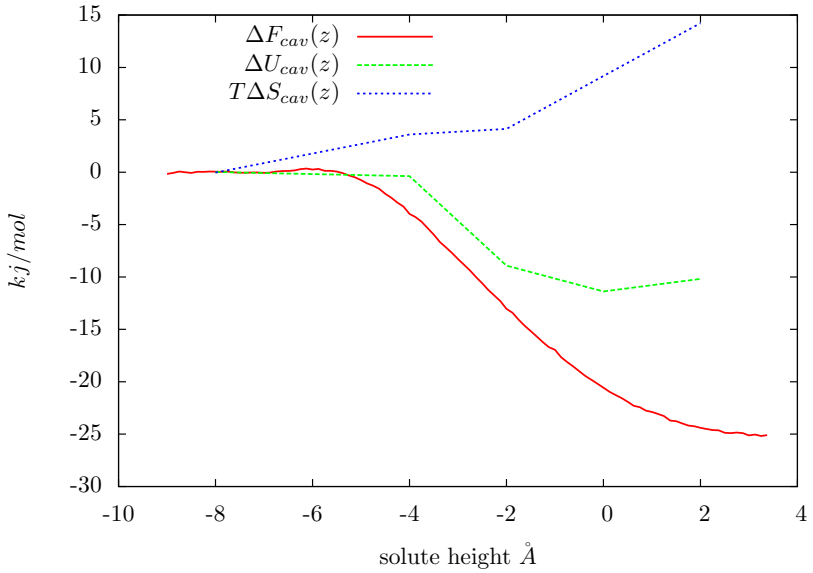

Figure 2.3: The change in the cavity formation free energy ΔF_{cav} as a solute with an excluding volume radius of 3.3 $\mathring{A}$ moves across the liquid vapor interface, together with its energetic and entropic components. The x-axis is distance from the Gibbs dividing surface, with negative values corresponding to liquid and positive values corresponding to vapor

.

This discussion of bulk solvation can be used to calibrate our expectations of what might happen when a charged solute migrates to the interface. The dominant energetic effect is likely to be associated with the charging free energy. The image charge picture described in chapter 1 ought to describe how the charging free energy changes as the ion approaches and crosses the surface, at least qualitatively. There may be a weak entropic effect associated with orientational restrictions imposed by the ion, but the main entropic effect is likely to be associated with the cavity formation term, which should be positive as the ion breaches the interface. In this picture the most likely scenario seems to be an entropy maximum but a much larger energy maximum when the ion is at the surface. While unlikely, its at least conceivable that for certain ion parameters the entropy maximum exceeds the energy maximum and there is a net driving force for moving the ion to the interface.

2.3 Generic features of surface adsorbing solutes

The above discussion highlights the fact that the energetic and entropic components of driving forces on ions near interfaces might shed some light on the adsorption mechanism. Studies of this nature on simple ions were surprisingly rare until very recently. In 2011, Caleman et al. studied the solvation thermodynamics for various ion parameters in small

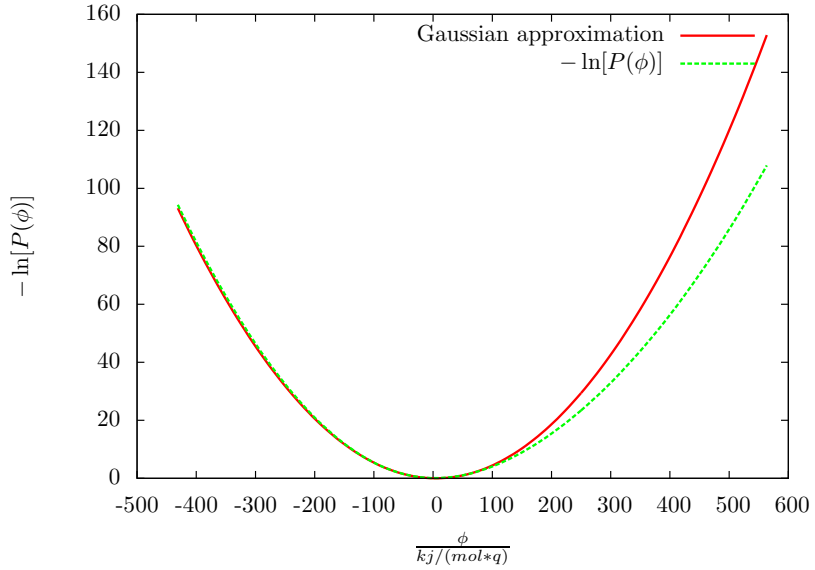

Figure 2.4: The distribution of the electrostatic potential inside an uncharged cavity of 3.3 Åin bulk SPC/E water. its plotted along side the gaussian distribution with the same mean and variance, and this is seen to be qualitatively a good approximation, even though it fails quantitatively.

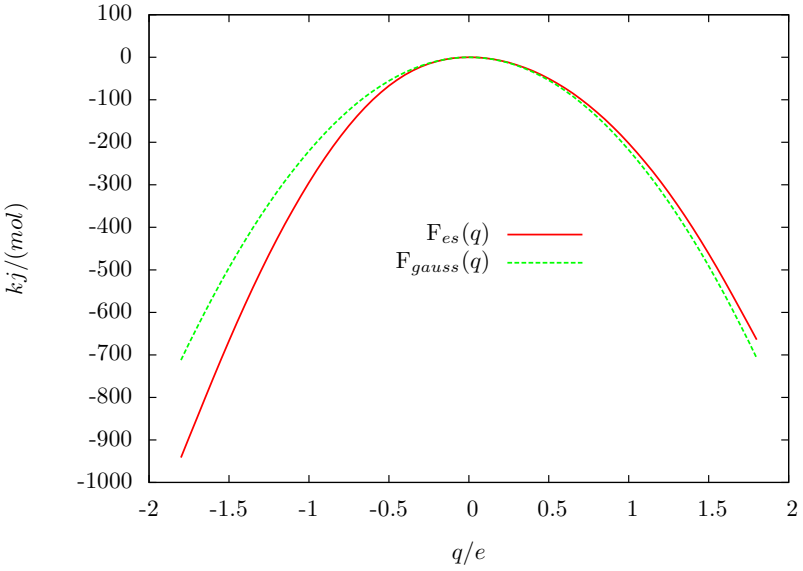

Figure 2.5: Charging free energy for a 3.3 $\mathring{A}$ cavity in bulk liquid, along with the gaussian approximation to this quantity.

droplets of liquid water [7]. They studied a variety of (mostly surface adsorbed) halide anions, and (all surface repelled) alkali metal cations. For every surface adsorbed anion they studied they found energetic and entropic minima for the ion at the surface. The authors computed a small collection of structural and orientational order parameters, but find nothing that is correlated to the relevant differences between the different ions, nor anything that explains what is missing from the solvation picture described in the last chapter. In a similar study a few years prior, Iuchi et al. studied the hydrated excess proton in water using empirical valence bond model simulations and found that it has a weak attraction to the interface, which is composed of an energetic and an entropic minimum [28]. Most importantly, experiments on the thiocyanate anion using SHG spectroscopy have confirmed that this ion adsorbs to the water vapor interface with both a negative entropy and a negative energy [46].

One of the surprising features of the Caleman work is that the entropy and energy minimum seem to be present for all of the surface adsorbing solutes they study which suggests that the underlying physics is not too ion specific. This implies that we can learn important things about this problem from studying a few ion parameters in great detail, rather than trying to study all of the physically relevant ion parameters. This also prompts the question, just how general is the behavior described?

The prototypical surface enhanced halide is the iodide anion. However, in non polarizable force fields, fully charged iodide is typically only weakly surface enhanced. Adding polarizability to the model is well known to facilitate the adsorption of ions to the surface [14, 35]. Polarizability is not, however, a necessary feature for ion adsorption and since we wish to study ion adsorption in the simplest context we exclude polarizability. One approach that has been used in simulations to study surface enhanced ions is making small changes to the charge of the ion. An iodide anion with the charge reduced to .8 e has a density at the surface which is nearly 100 times its density in bulk [41]. This small reduction of charge does not change the fact that it is a strongly solvated ion, it just allows us to tip the balance towards surface enhanced so that we can study the relevant driving forces more clearly. For this reason we study an iodide model with the charge reduced to .8 or .75 e.

Figure 2.6 shows the density profiles for $I^{-0.8}$ and $I^{-0.75}$, along with the free energy decomposition corresponding to these curves. The energetic and entropic minima observed by Caleman et al. are clearly present even without polarizability. This model is slightly simpler than the model studied by Caleman, but it still has all of the subtleties and complexities associated with hydrogen bonding. To remove these details we've also studied the Stockmayer solvent referred to above. As shown in fig. 2.7, the gross behavior is exactly the same as in the water models, which suggests that the discussion in section 1 is missing something fundamental about fluid interfaces, and not just solvent-specific details.

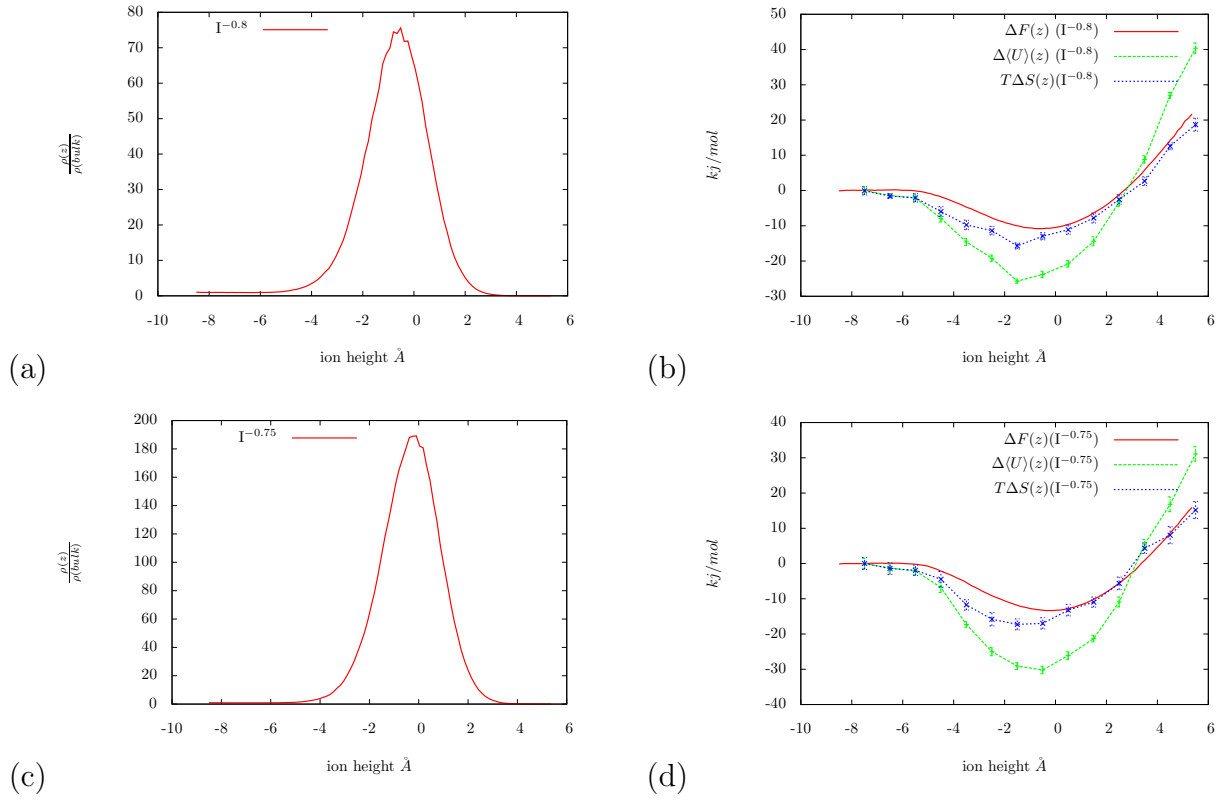

Figure 2.6: Ion density profiles and corresponding free energies, average energies and entropies for two versions of fractionally charged Iodide. The x-axis on this plot corresponds to distance from the Gibbs dividing surface, with negative values corresponding to the liquid phase and positive values corresponding to the vapor phase. Figure a shows how the $I^{-0.8}$ density changes as the ion crosses the interface. The free energy change for this process, along with its energetic and entropic components, are shown in figure b. Figures c and d show the same quantities for $I^{-0.75}$. The energy and entropy minima observed in these plots are fairly generic features of surface adsorption.

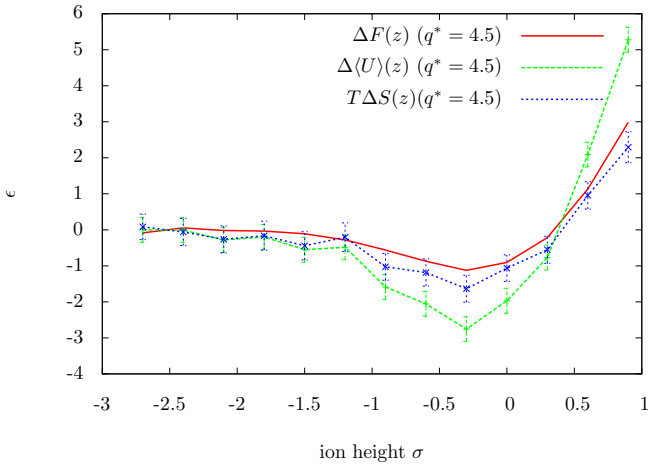

(a)

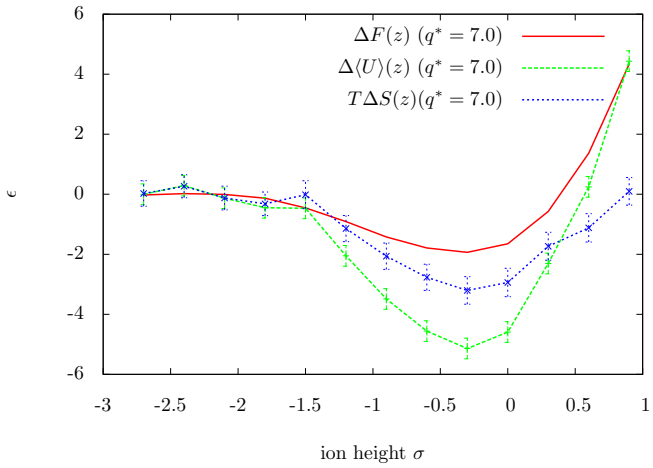

(b)

Figure 2.7: Free energy profiles for moving an ion across the interface for two ions in the Stockmayer solvent, along with their energetic and entropic components. The ion shown in figure a has a reduced charge of $q^* = 4.5$ and a Lennard-Jones diameter of 1.25σ, whereas the ion show in figure b has a reduced charge of $q^* = 7.0$ and Lennard-Jones diameter of 1.5σ.

2.4 A very simple energetic decomposition

In this section we describe how to spatially parse the relevant contributions to the average energy, and then describe an extremely simple approximation that recapitulates the relevant trends. We are ultimately interested in how the average energy depends on ion position, which means we can neglect contributions from the average kinetic energy, which depends only on the number of degrees of freedom. The potential energy functions for the models we study are pairwise decomposable, which means we can cleanly isolate contributions due to the ion-solvent interactions and contributions due to solvent-solvent interactions. The total potential energy is then the sum of these two terms. For an ion at position z, its interaction with solvent molecule i depends on its position r_i and orientation Ω_i, and we denote this by $u_{is}(r_i, z, \Omega_i)$. Likewise, the interaction between two solvent molecules depends on the positions and orientations of both molecules and we denote this by $u_{ss}(r_i, \Omega_i, r_j, \Omega_j)$. The interaction between the ion and all N solvent molecules is a straight forward sum

$$U_{is}(z) = \sum_{i=1}^{N} u_{is}(r_i, z, \Omega_i) = \int dr \sum_{i=1}^{N} \delta(r - r_i) u_{is}(r_i, z, \Omega_i). \tag{2.22}$$

If we then take the average of this equation we find

$$\langle U_{is}(z) \rangle = \sum_{i=1}^{N} u_{is}(r_i, z, \Omega_i) = \int dr \langle \sum_{i=1}^{N} \delta(r - r_i) u_{is}(r_i, z, \Omega_i) \rangle. \tag{2.23}$$

The quantity in brackets is the average solvent density at position r times the average interaction between a solvent molecule at r and an ion at position z ($\bar{u}_{is}(r, z)$). We can then rewrite this equation as:

$$\langle U_{is}(z) \rangle = \int dr \rho_s(r) \bar{u}_{is}(r, z) \tag{2.24}$$

A similar operation applies to the solvent-solvent interaction. We can write its average as

$$\langle U_{ss}(z) \rangle = \frac{1}{2} \sum_{i \neq j}^{N} u_{ss}(r_i, \Omega_i, r_j, \Omega_j) = \frac{1}{2} \int dr \sum_{i=1}^{N} \langle \delta(r - r_i) \sum_{j \neq i} u_{ss}(r_i, \Omega_i, r_j, \Omega_j) \rangle. \tag{2.25}$$

Denoting the average interaction between a solvent molecule at position r and every other solvent molecule as $\bar{u}_{ss}(r, z)$ we have the following compact formula:

$$\langle U_{ss}(z) \rangle = \frac{1}{2} \int dr \rho_s(r) \bar{u}_{ss}(r, z). \tag{2.26}$$

Equations 2.24 and 2.26 provide connections between spatially resolved quantities and the overall average energy as a function of ion position, and this spatial resolution can provide us with structural insight into the observed energetic trends.

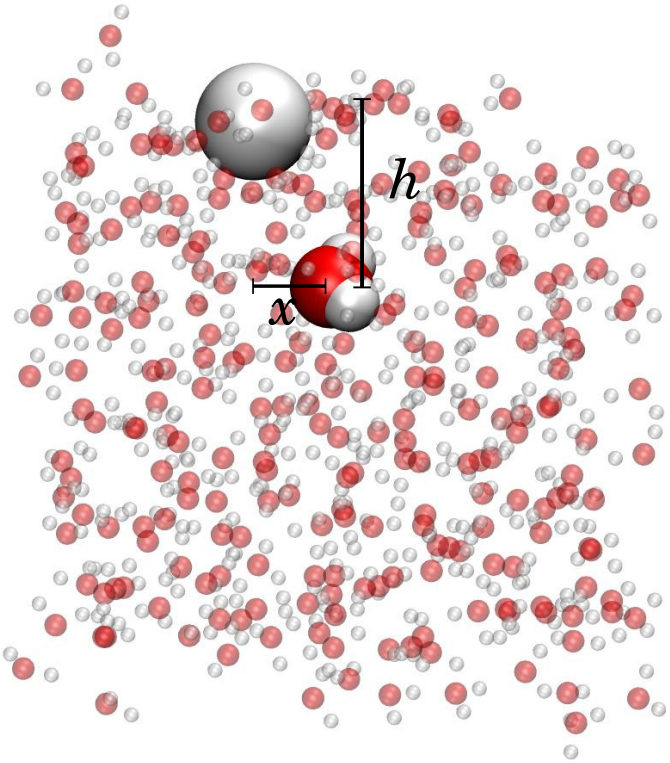

Figure 2.8: An illustration of the reference system used to spatially resolved contributions to the average energy and entropy. x is the perpendicular distance between a particular water molecule and the ion, and h is the vertical distance between that water molecule and the interface. In this illustration the ion position z is at the interface/

The systems studied here all have rotational symmetry about the axis connecting the ion to the interface, which means that quantities like $\bar{u}_{ss}(r, z)$ (for a given ion height) only depend on the perpendicular distance from the ion and the vertical distance from the interface, we denote this dependence by $\bar{u}_{ss}(x, h, z)$ (see figure 2.8). Figure 2.9 shows the quantities $\bar{u}_{ss}(x, h, z)$ and $\bar{u}_{is}(x, h, z)$ as a function of these two coordinates, for an ion in bulk, and an ion at the interface.

These energy maps highlight the fact that there are 3 important length scales in this problem. The first of these is the size of the ion, in this case its approximately 4 $\mathring{A}$, and we know that for realistic ions this will vary by $\simeq$ 1.5 $\mathring{A}$ in either direction. The second of these is the length scale of interaction between the ion and neighboring water molecules. This length scale appears to be about 3 $\mathring{A}$. Again we expect this to vary slightly depending on ion parameters like charge, size and polarizability. The third length scale is the depth of the interfacial region. As a rough estimate this length scale is approximately 3 or 4 $\mathring{A}$. None of these length scales dwarfs any of the others for this specific case, which is a sign of

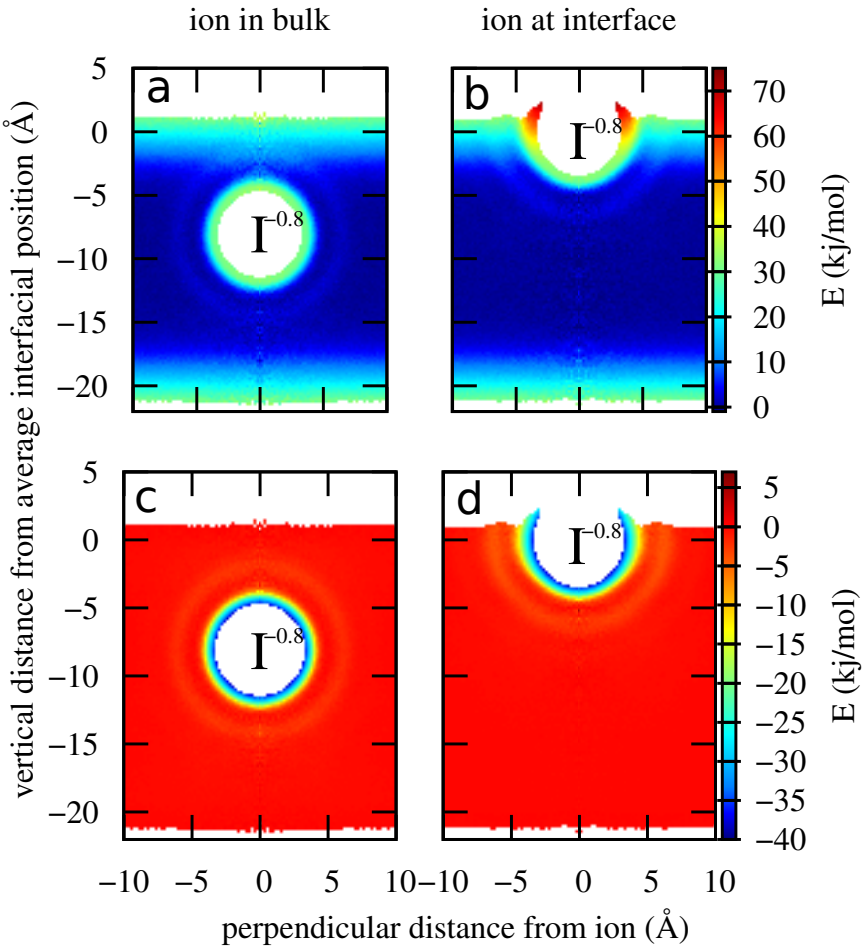

Figure 2.9: The spatially resolved contributions to the average potential energy described above. Plots A and B show $\bar{u}_{ss}(x, h, z)$, the average solvent-solvent interaction strength, where plots C and D show $\bar{u}_{is}(x, h, z)$, the average solvent-ion interaction strength for an $I^{-.8}$ anion in bulk (A and C) and at the Gibbs dividing surface (B and D). The x-axis is the perpendicular distance from the ion, x, and the y-axis is the distance to the interface, h. Whereas z simply denotes the distance between the fixed ion and the interface. The negative x-axis on these plot is merely a visual aid, in truth, the x-axis is a strictly positive quantity. It is defined as $x = \sqrt{(x_r - x_i)^2 + (y_r - y_i)^2}$ where x_r and y_r are the x and y coordinates of position r and x_i and y_i are the same coordinates of the ion. The white regions in these plots correspond to very low or no solvent density, either in the vapor phase or overlapping with the ion. It is important to note, however, that the effective diameter of this ion is actually the radius of the big white circles, and that these plots therefore make the ion appear twice as big as it is.

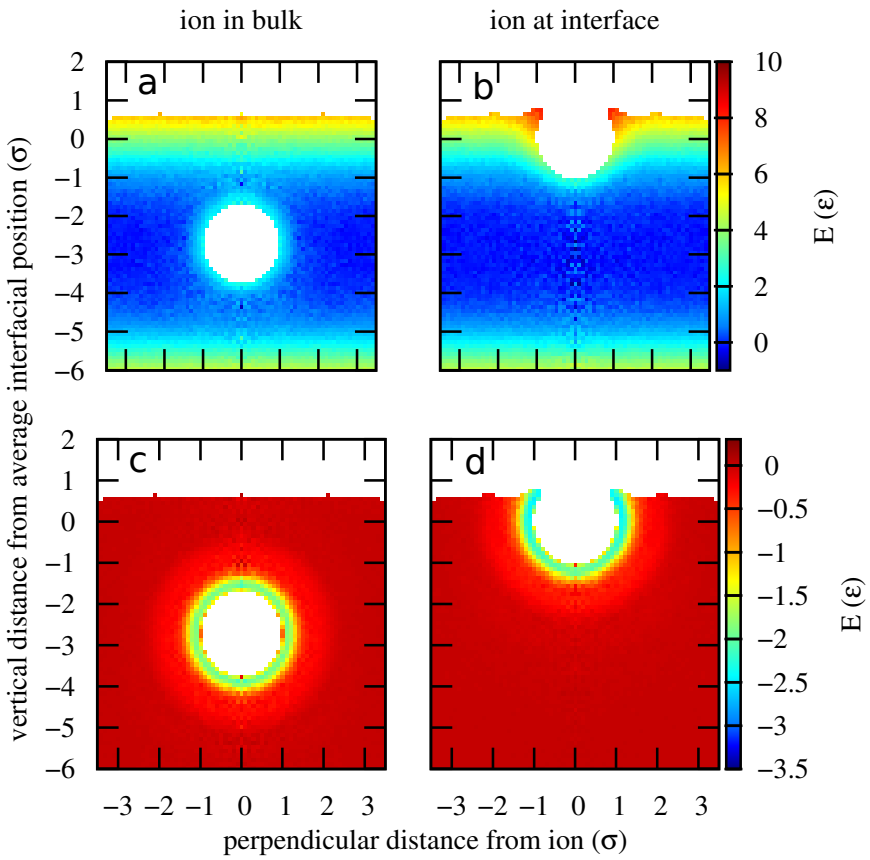

Figure 2.10: The spatially resolved contributions to the average potential energy, for an ion in a Stockmayer solvent. These quantities are the analogues of the quantities show in figure 2.9 for an ion in water. The ion considered here has a reduced charge of 4.5 and a diameter of 1.25 σ.

the fact that several forces are competing with one another. Consider what would happen if one of these length scales were significantly larger than the other two. If, for example, the length scale of interaction between ions and water molecules were 10 $\mathring{A}$, we would expect the dominant effect to be associated with how many water molecules the ion was interacting with as it crossed the interface, and that number might be a relatively simple, monotonically decreasing function of ion height. However, no such separation of length scales exists, which prevents us from making that sort of simplification.

Analogues of u_{is} and u_{ss} for an ion in the Stockmayer solvent are show in figure 2.10. There are indeed some noticeable differences between the features in these figures and features in fig. 2.9. For example, the interactions of solvent molecules with the ion look slightly less localized. And the decrease in solvent-solvent interactions for a solvent molecule neighboring the ion does not look quite as severe as it does for water. Furthermore, the solvent-ion interactions become noticeably slightly stronger when the ion is at the interface. However,

none of these features qualitatively change the picture described.

The ion described by figure 2.9 is a surface enhanced ion with an energy minimum at the surface of 20 kj/mol, however by making small adjustments to the size and charge of the ion we could easily make this energy minimum change sign. However, its hard to imagine the features in figure 2.9 making any dramatic changes (we certainly don't expect either $\bar{u}_{ss}$ or $\bar{u}_{is}$ to change sign), and this intuition is in fact correct. To get a better sense for how the balance between surface enhanced and surface repelled is tipped, we will compare this surface enhanced ion with a surface repelled one. The quantity we will compare arises from a combination of 2.24 and 2.26. Combining these two equations we find

$$\langle U(z)\rangle = \int dr\rho_s(r,z)[\bar{u}_{is}(r,z) + \frac{1}{2}\bar{u}_{ss}(r,z)] = \int dr\rho_s(r,z)\mathcal{E}(r), \tag{2.27}$$

where this last equation defines $\mathcal{E}$. In terms of the variables x and h, this integral becomes

$$\langle U(z)\rangle = \int_0^\infty \pi x dx \int_{-\infty}^\infty dh\rho_s(x,h,z)\mathcal{E}(x,h,z). \tag{2.28}$$

The quantity $\rho_s(x,h,z)\mathcal{E}(x,h,z)$, while not quite as simple as either $\bar{u}_{is}$ or $\bar{u}_{ss}$, has a very straightforward interpretation. It is the quantity that you integrate over to determine the total average energy. Figures 2.11 and 2.12 show these quantities for both the surface enhanced $I^{-.8}$ and the surface repelled Cl^-. For each ion we look at 3 different values of z as the ion approaches the interface, and beside each energy-density map is shown the plot of total average energy as a function of ion height, along with a green line indicating which height you are looking at on the left, so you can see exactly what that map integrates to. The $I^{-.8}$ and Cl^-, have very similar qualitative features from this perspective. Each ion has deeps wells around it, indicating that water molecules immediately coordinating the ion are in an energetically favorable state. The Cl^- has slightly deeper minima around it both in bulk and at the interface and it is slightly smaller but there are no qualitative differences. The other pronounced feature of these maps is the interface. The energy density rises at the interface, indicating that water molecules near the interface are in an energetically favorable state. In either case, when the ion is placed at the interface it is occupying volume in a high energy region which effectively lowers the overall energy, but it also loses some of the deep purple well around it, which raises the energy. The $I^{-.8}$ occupies a little more space in the interfacial region and doesn't lose as much when it sacrifices its solvation shell. The balance of these two forces ultimately determines whether or not the energy is minimized by putting it at the interface. This balance is tipped one way for the $I^{-.8}$ and another way for the Cl^-.

There is one surprisingly simple feature of the energy maps in 2.9. Certain features are independent of whether the ion is at the surface or in bulk. Plots C and D, for example, look nearly identical when referenced with respect to the ion, except for those regions with extremely low solvent density. There are in fact subtle differences between these plots, which are important when discussing aspects of charge asymmetry (see chapter 3), but for now we will ignore those differences. Plots A and B likewise, seem to have surprisingly predictable behavior when the ion moves to the interface. Furthermore, the dominant features in these

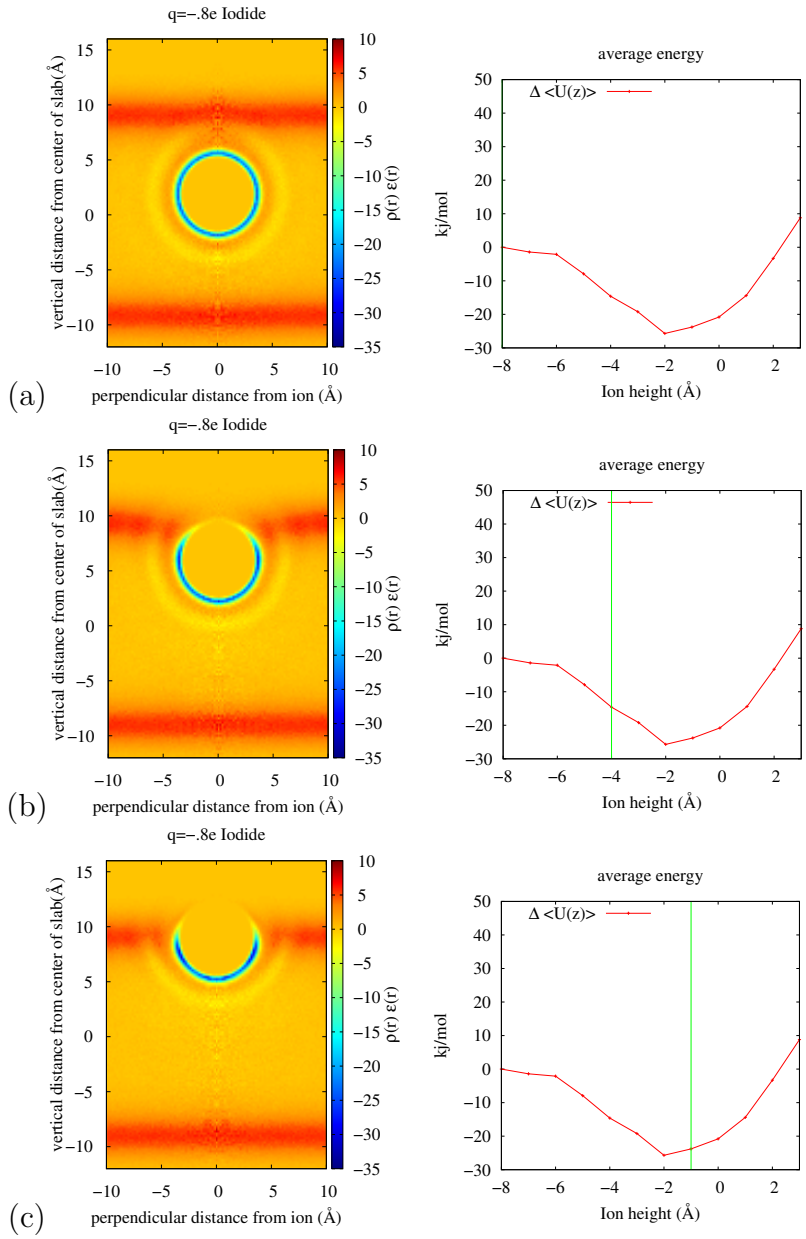

Figure 2.11: Plots of $\rho_s(x,h,z)\mathcal{E}(x,h,z)$, for three different values of ion height z (-8, -4 and -1 $\mathring{A}$) as the $I^{-.8}$ ion approaches the interface. The plots on the right show how the total energy changes as the ion moves, and the plots on the left must integrate to the value indicated on the right, which gives a sense for how the competing forces balance one another.

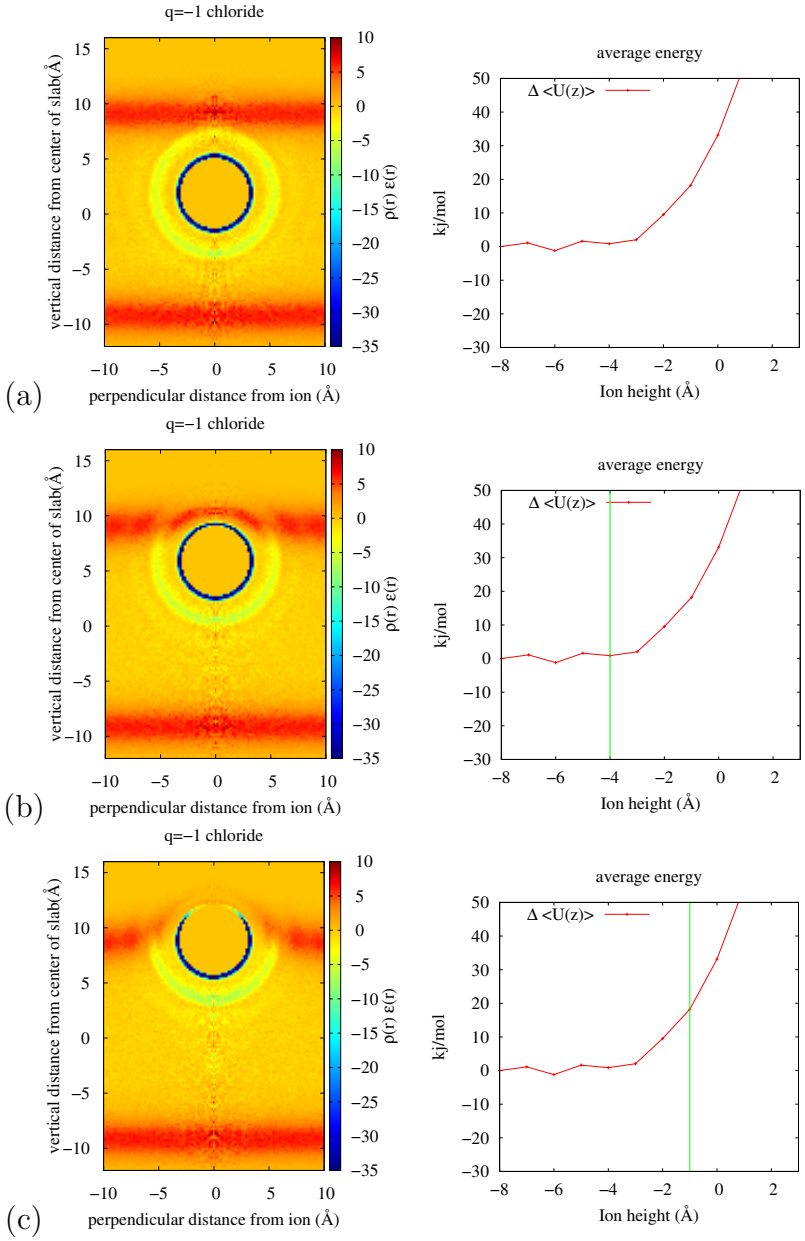

Figure 2.12: Same as above except for the Cl^- ion. We see some of the same competing forces as above, but in this case the balance is tipped in such a way that the chloride avoids the surface

maps have a relatively spatially local character. Motivated by these observations we will define what is called the local approximation. In the simplest version of this approximation, space is partitioned into three regions. The coordination region consists of all the water molecules with a certain cutoff distance l_{coord} from the center of the ion. The surface region consists of all water molecules within a certain distance of the Gibbs dividing surface l_{surf}. Molecules in the overlap between these two regions are assigned to the coordination region and all others are assigned to the bulk region. To arrive at the local approximation we partition the eq. 2.27 according to these three regions as

$$\langle U(z)\rangle = \int_{coord} dr\rho_s(r,z)\mathcal{E}(r) + \int_{surf} dr\rho_s(r,z)\mathcal{E}(r) + \int_{bulk} dr\rho_s(r,z)\mathcal{E}(r). \tag{2.29}$$

If we multiply and divide by the average number of particles in each region we arrive at:

$$\langle U(z)\rangle = n_{coord}(z)\frac{\int_{coord} dr\rho_s(r,z)\mathcal{E}(r)}{n_{coord}(z)} + n_{surf}(z)\frac{\int_{surf} dr\rho_s(r,z)\mathcal{E}(r)}{n_{surf}(z)} + n_{bulk}(z)\frac{\int_{bulk} dr\rho_s(r,z)\mathcal{E}(r)}{n_{bulk}(z)}. \tag{2.30}$$

This has the structure of an average energy per molecule in a given region, times the number of water molecules in that region. This average energy per molecule in region i is defined as:

$$\bar{\mathcal{E}}_i(z) = \frac{\int_i dr\rho_s(r,z)\mathcal{E}(r)}{n_i(z)}. \tag{2.31}$$

Equation 2.30 now simplifies to:

$$\langle U(z)\rangle = n_{coord}(z)\bar{\mathcal{E}}_{coord}(z) + n_{surf}(z)\bar{\mathcal{E}}_{surf}(z) + n_{bulk}(z)\bar{\mathcal{E}}_{bulk}(z). \tag{2.32}$$

This equation is an exact decomposition of the energy. The local approximation consists of assuming that we can replace $\bar{\mathcal{E}}_i(z)$ with its value in bulk $\bar{\mathcal{E}}_i$, which we will denote by just suppressing the z dependence. This gives us:

$$U_{loc}(z) = n_{coord}(z)\bar{\mathcal{E}}_{coord} + n_{surf}(z)\bar{\mathcal{E}}_{surf} + n_{bulk}(z)\bar{\mathcal{E}}_{bulk}. \tag{2.33}$$

We will be using this equation a lot so its worth discussing the approximate nature in detail. This equation is really an approximation in two distinct but related senses. The first of these is the assumption that we can define relatively short cutoff distances, either from the ion, or from the interface, beyond which a water molecules interactions are nearly the interactions of a water molecule in bulk. This approximation seems like a safe one based on the energy maps, however the scheme for partitioning water molecules into different regions introduces a different layer of approximation. Recall that if a water molecule is in the overlap between the surface and the coordination regions, we assign it to the coordination region. When the sphere defining the coordination region starts to penetrate the plane defining the surface region, it overlaps with low energy regions more than high energy regions.

This means that even if the ion itself did not effect any of the interactions outside of its cutoff l_{coord}, the assumption that $\bar{\mathcal{E}}_{surf}(z) = \bar{\mathcal{E}}_{surf}$ would still be invalid because these two quantities would involve averages over different geometries. Furthermore, the assumption that $\bar{\mathcal{E}}_{coord}(z) = \bar{\mathcal{E}}_{coord}$, will clearly breakdown when the coordination region is at the surface and is composed of water molecules that are both coordinating the ion and at the surface. The criteria for success of the local approximation clearly involves some subtleties (for more on this see chapter 3, and for an extension of these ideas that consider more than 3 regions see [59]). However it ought to capture some of the coarse features of adsorption energetics discussed above, for example, the way the ion at the surface excludes volume in a high energy region.

The local approximation emphasizes the fact that the most important structural changes induced by an ion are in its first solvation shell. This locality is slightly at odds with the long held notion that certain ions are structure makers and certain are structure breakers which holds that ions in water have a long range effect that either strengthens (structure makers) or weakens (structure breakers) the hydrogen bond network. There is mounting experimental evidence that there is no such long range effect, even at high concentrations and that this distinction may not be appropriate. One such study concerns the orientational dynamics of water molecules in solution with several different ions at concentrations up to 6M. Water molecules that are hydrogen bonded to an anion have a different O-H stretching frequency than water molecules that are hydrogen bonded to another water molecule. Pump-probe spectroscopy can then be used to study the orientational decorrelation of these distinct populations separately. The water molecules hydrogen bonded to the anion do have a slower orientational correlation time, but they have no effect on the orientational dynamics of the bulk water, even at higher concentrations [43, 65, 56].

For the case of the $I^{-0.8}$ we can choose parameters for which the local approximation is remarkably successful (see fig. 2.13). The cutoff for the coordination region used was 4.2 $\mathring{A}$ away from the ion, and the cutoff for the surface region was 3.8 $\mathring{A}$ below the Gibss dividing surface.

2.5 Possible origins of entropic costs

The last section introduces a new perspective on how solvation energies change as a solute crosses an interface. Such a straightforward decomposition is not possible for the solvation entropies and we are therefore faced with a slightly more challenging problem. We have attempted to quantify two different contributions to the solvation entropy to see how they vary with ion position. The first of these is a measure of orientational entropy. Ion solvation entropies in bulk are known to have some subtleties [38] which are usually associated with the orientational freedom of surrounding water molecules. How these effects play out near an interface is not very well studied. We find that a rough measure of orientational entropy predicts a very weak entropic effect which has the wrong sign for moving the ion to the interface. The second effect we study involves the entropy associated with fluctuations of

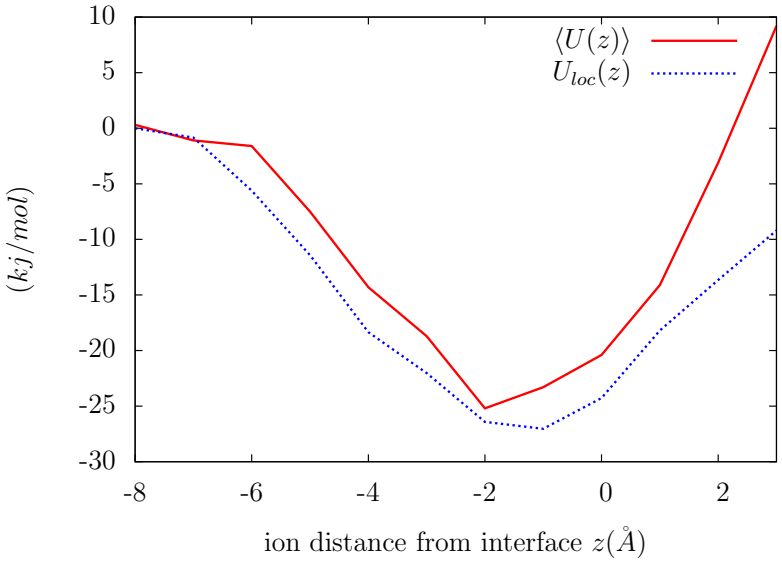

Figure 2.13: The local approximation to the average energy described in the text along with the true average energy. The local approximation agrees very well, predicting both the position and depth of the minimum with near quantitative accuracy.

the interface and this effect is shown to be a very large one, which furthermore predicts the correct sign for the entropy change as the in moves to the surface.

The orientational entropy described above is computed as follows. For a solvent molecule at position r we compute the probability distribution $p(cos(\theta), r)$ where θ is the angle that the molecule's dipole forms with the z-axis. We then compute the Gibbs entropy associated with this probability distribution as:

$$s(r) = -k_{\mathrm{B}} \int dcos(\theta) p(cos(\theta), r) \ln p(cos(\theta), r). \tag{2.34}$$

This is roughly an entropy per particle. To estimate the total entropy we multiply by density and integrate over space:

$$S_{local} = \int dr s(r) \rho_s(r). \tag{2.35}$$

Figure 2.14 shows $s(r)$ for the I^{-}[8] ion in bulk and at the interface. In either case we find that water molecules in the neighborhood of the ion are subject to orientational restrictions, as are water molecules at the interface. The natural expectation is that bringing to the ion to the interface releases some of these constraints and therefore the entropy goes up. By integrating over these maps that is indeed what we find, but the magnitude is a surprisingly small 0.8 k_{B}.

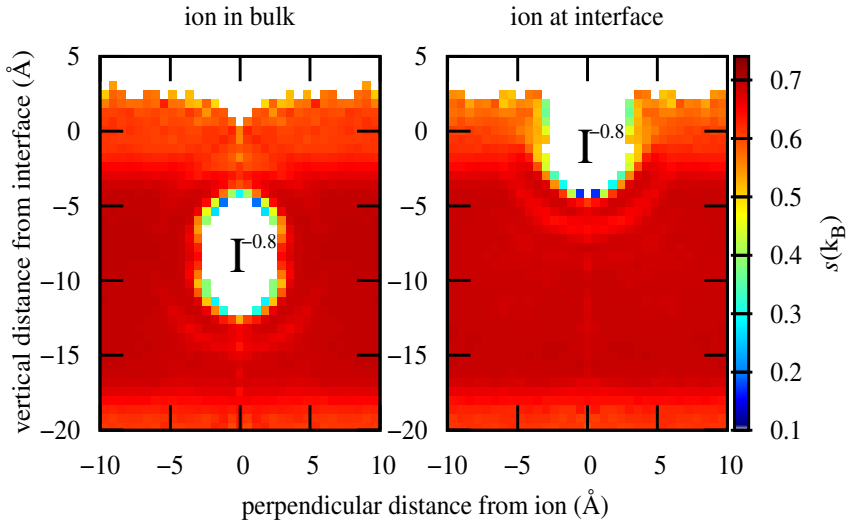

Figure 2.14: The spatially resolved orientational entropy per particle described in the text for two positions of the $I^{-.8}$ ion. The associated total entropy is higher when the ion is at the interface (b).

One feature of this analysis is that it supposes that all the water molecules are statistically independent and it will therefore not register any collective fluctuations. The failure of this analysis then suggests that perhaps the substantial entropy changes we see come from the ions influence on some collective modes. Liquid-vapor interfaces are known to have a set of very soft collective modes known as capillary waves. Inspired by this theory we will attempt to estimate the entropy contained in fluctuations of the liquid vapor interface.

Conventional definitions of an interface, such as the Gibbs dividing surface are statistical definitions in the sense that they require us to average over many configurations. In this work we need a definition that can assign an interface to a single configuration so that we can keep track of how it fluctuates. Such a definition was developed by Willard and Chandler [63]. In this prescription we use a coarse-grained density field that places a gaussian mass density on each oxygen atom. For each lateral position, we then determine the height of the interface as the place where this coarse-grained density drops below half of its bulk value. This scheme produces surface topographies that visually match our sense of where the interface should be (see figure 2.15).

The scheme described produces a height $h(\boldsymbol{x})$ at each point on a discrete two dimensional grid $\boldsymbol{x}$, where we may make the grid as coarse or as fine as we like. We then adopt the perspective that the heights at each grid point are a set of coupled harmonic oscillators. That is, we assume the potential energy has the form:

$$U([\delta h(x)]) = \frac{k_B T}{2} \sum_{x_i, x_j} \delta h(x_i) \chi^{-1}(x_i, x_j) \delta h(x_j). \tag{2.36}$$

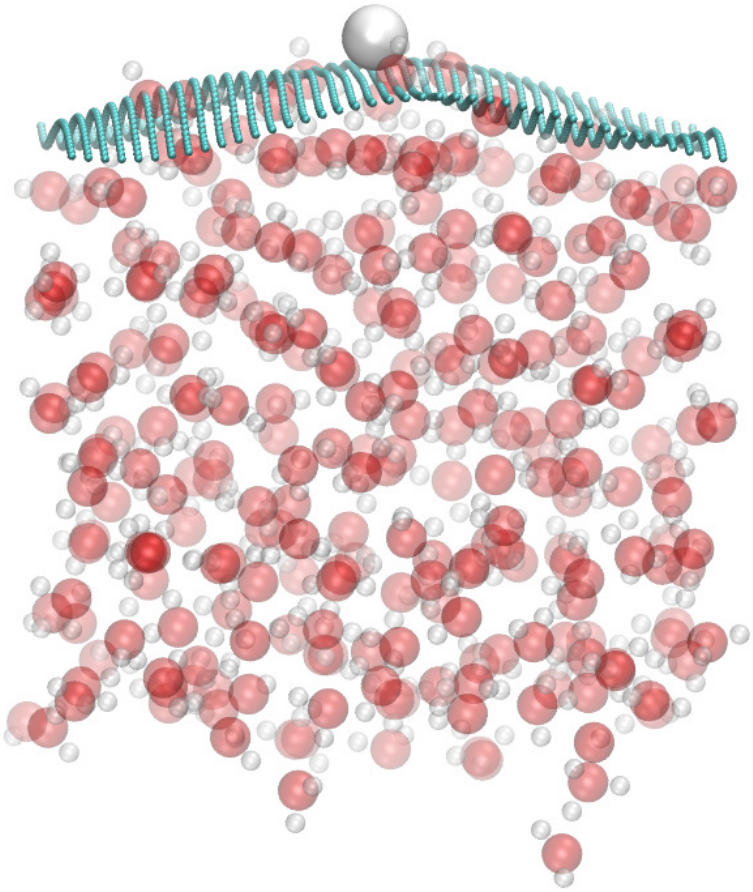

Figure 2.15: The intrinsic interface defined in the text for a single configuration that contains an ion at the surface.

The partition function for this model is then given by

$$Z = \int \Pi_i d\delta h(x_i) \exp[-\frac{1}{2} \sum_{x_i,x_j} \delta h(x_i) \chi^{-1}(x_i, x_j) \delta h(x_j)] \tag{2.37}$$

This can be evaluated as a straight forward gaussian integral by diagonalizing χ^{-1}, and the result is

$$Z \simeq det(\chi^{-1})^{-\frac{1}{2}}. \tag{2.38}$$

You can also show that the inverse of χ^{-1} is the correlation matrix:

$$\chi(x_i, x_j) = \langle \delta h(x_i) \delta h(x_j) \rangle. \tag{2.39}$$

The determinant of a matrix and its inverse are related by

$$det(\chi^{-1}) = det(\chi)^{-1}. \tag{2.40}$$

Computing the free energy is then a simple matter of combining equations 2.40 and 2.38:

$$F = -\frac{k_B T}{2} \ln[det(\chi)] \tag{2.41}$$

Applying the identity $S = -\frac{\partial F}{\partial T}$ we arrive at a simple formula for the entropy:

$$S = \frac{k_B}{2} \ln[det(\chi)]. \tag{2.42}$$

This equation provides us with a way to estimate the entropy contained in fluctuations of the interface by simply measuring correlated fluctuations. We will henceforth refer to this procedure as the harmonic analysis. As we will see, the reliability of this analysis is a somewhat delicate issue. The assumption that fluctuations of the interface are gaussian is likely to break down when you approach molecular length scales, and furthermore, its not clear how well the Willard interface procedure is even capturing these fluctuations when there is a solute at the surface.

It is nonetheless the case that this procedure can capture certain features of the entropy profile as the ion moves across the interface. Figure 2.16 shows the the true entropy profile along with the entropy calculated from 2.42. Computing this equation requires us to choose a coarse graining length for the solvent density field, which in this case is $\sigma = 3.1\mathring{A}$, and a grid resolution, which determines how closely spaced points on the 2-d lateral grid are. Later on we will discuss changing the grid resolution, but for now we choose it to be $\Delta = 2.5\mathring{A}$. The harmonic analysis does in fact predict an entropy minimum for the ion at the interface, and it does predict that the entropy starts to rise again as the ion crosses into the vapor phase. The exact location of the minimum is off by about 2 $\mathring{A}$, and its magnitude is only about half of the true entropy minimum. Furthermore, there is a larger spurious entropy

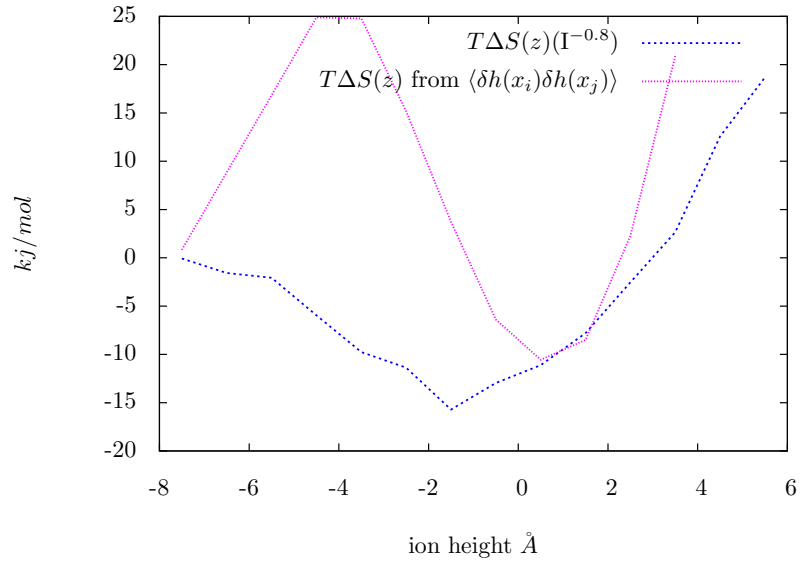

Figure 2.16: The true entropy profile for $\mathrm{I}^{-0.8}$, along with the entropy computed from fluctuations of the liquid vapor interface.

maximum a few Angstroms below the interface. As we will see this ion is a particularly challenging case for this harmonic analysis and we can find cases where it does better.

The fact that the entropy has a minimum at the surface is a sign that either fluctuations are attenuated or that they are more highly correlated. We can get a sense for how much these fluctuations are attenuated in the vicinity of the ion by looking at $\langle \delta h(x)^2 \rangle$ where x is the perpendicular distance between a point on the surface and the location of the ion. Figure 2.17 shows these quantities for a water-vapor surface with an $\mathrm{I}^{-.8}$ ion 7 Angstroms, and one for a surface with an $\mathrm{I}^{-.8}$ ion right at the Gibbs dividing surface.

Figure 2.18 compares the true entropy and the entropy computed from the harmonic analysis for the surface repelled Cl^- ion. In this case the true entropy has no minimum at the interface, and the harmonic analysis appears to predict a very shallow minimum. There is, however no spurious maximum below the interface and it very accurately predicts the entropy rise after the ion crosses the interface.

2.6 A detailed discussion of the harmonic analysis

In the last section we demonstrated that we can plausibly draw a connection between solvation entropies for an ion at the surface and its impact on capillary wave fluctuations. The analysis we used to draw this conclusion is plagued by a few problems in the sense that it predicts a large entropy maximum before the ion crosses the surface, and it also requires us to choose a grid spacing Δ which is somewhat arbitrary. In this section we will attempt to

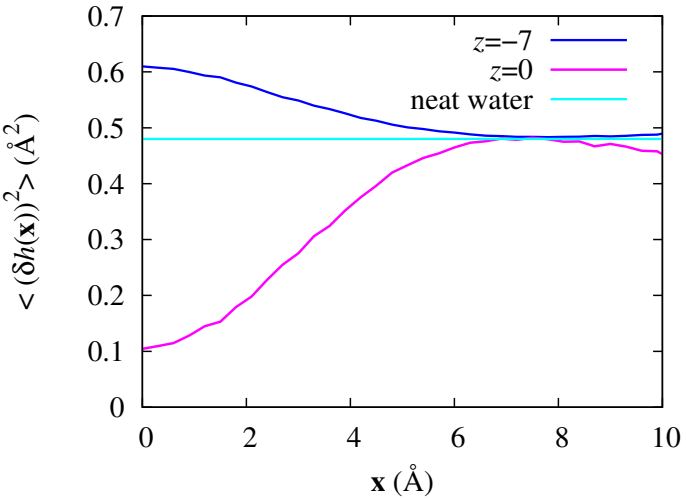

Figure 2.17: Fluctuations of a water-vapor interface with an ion either 7 below the Gibbs dividing surface or right at it, as a function of perpendicular distance from the ion, as well as the fluctuations of the neat water-vapor interface.

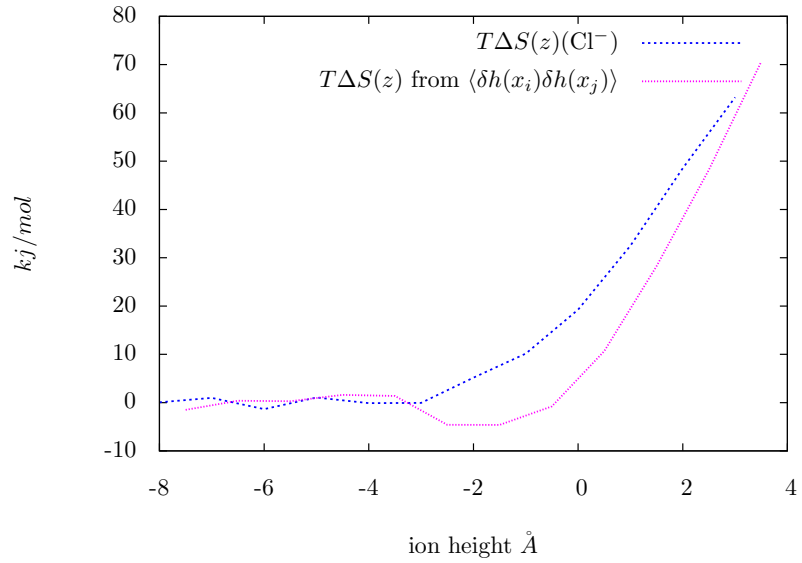

Figure 2.18: The true entropy profile for Cl^-, along with the entropy computed from fluctuations of the liquid vapor interface.

make the connection between surface fluctuations and entropies more concrete by assessing the strengths and flaws of this algorithm in more detail.

Figure 2.20 compares the estimated entropy changes for several different choices of the grid spacing for the $I^{-.8}$ ion. While the qualitative features of these curves stay the same, the quantitative features clearly depend strongly on the grid spacing. In particular, both the entropy maximum and the entropy minimum become more severe as the grid spacing is lowered. Some dependence on this grid spacing is to be expected. It is clear that a widely space grid will not resolve the most important fluctuations, which, as we see from figure 2.17 will occur on length scales less than about 7 $\mathring{A}$. Also a very finely spaced grid will pick up features that are necessarily artifacts. If the grid spacing is 0.5 $\mathring{A}$, features at the shortest length scale are surely not something that we would describe as a collective fluctuation of the liquid-vapor interface. The natural intermediate choice seems like something about the size of a water molecule or on the order of 3 $\mathring{A}$. Figure **??** shows that even if we restrict our attention to length scales of this order we find serious quantitative differences.

One possible source of error is that the fluctuations of the surface deviate from Gaussian behavior at the length scales of interest and that we need to account for this in some way. When the underlying model is not strictly harmonic there is no simple analogue to equation 2.42 that will allow us to estimate the entropy. We will use an approach here that is inspired by the harmonic approach and should give us some sense of the importance of non gaussian fluctuations. In a harmonic system the eigenvectors of $\chi(x_i, x_j)$, are the normal modes of $\chi(x_i, x_j)$. The normal modes are sets of fluctuations that are completely uncoupled from one another. In a system that is not harmonic, we can still of course compute the eigenvectors of $\chi(x_i, x_j)$, but there is no general sense in which these are independent modes. The approach we use here is to assume that the eigenvectors of χ are still roughly independent and then to compute the statistics of the fluctuations of these modes. If we denote the α eigenvector of χ by $\xi^\alpha(x_i)$, then for a given configuration of $\delta h(x_i)$, the projection on to the normal mode is

$$\eta^\alpha = \sum_i \delta h(x_i)\xi^\alpha(x_i). \tag{2.43}$$

We then compute the probability distribution of this component, $P^\alpha(\eta^\alpha)$ by sampling over many configurations. We can then determine an effective Gibbs entropy associated with each mode as

$$S^\alpha = -k_\mathrm{B} \int d\eta P^\alpha(\eta) \ln P^\alpha(\eta). \tag{2.44}$$

And finally obtain a total entropy by summing over all the modes:

$$S = \sum_\alpha S^\alpha. \tag{2.45}$$

If the probability distributions are all exactly gaussian then these two equations reduce to equation 2.42. Figure 2.19 shows the entropy profile calculated from equation 2.45, which we

call the extended harmonic analysis, along with the true entropy profile and the one computed from equation 2.42 for reference. The extended harmonic analysis hardly improves upon the standard harmonic analysis at all, suggesting that the fluctuations are approximately gaussian. Figure 2.19 also shows the probability distributions $P^o(\eta^0)$ for the eigenvector with the largest eigenvalue for several ion heights, and these are approximately gaussian.

These results do not rule out the possibility that there are important non gaussian fluctuations, it just suggests that they are probably hard to account for and capture with the simple intrinsic interface picture. There is, however another source of error which is slightly easier to systematically study and that is the finite size of the ion. Constructing the Willard interface in the simplest way involves placing a gaussian mass density on each oxygen atom. Ions that exceed the length scale of this Gaussian introduce significant inhomogeneities into this coarse-grained density field which means that the density may drop below the cutoff value of $0.5\rho_{bulk}$ inside of the ion. This will create problems for the algorithm that assigns the interface when the interface is neither unambiguously above or below the ion. To illustrate this point figure 2.21 shows maps of average solvent density as a function of perpendicular distance from an $I^{-.8}$ ion and vertical distance from the interface as the ion approaches and crosses the Gibbs dividing surface. Overlain on these maps are two quantities that are computed from the Willard interface. The red lines are the average height of the interface and the green lines show $\langle(\delta h(x))^2\rangle$. Notice how the ion crosses a threshold where the average position of the Willard interface starts to penetrate its interior. When this threshold is crossed the fluctuations of the interface start to rise. This rise is mostly an artifact of the fact that there is a void of solvent density right below the interface, and it is also responsible for the large entropy maximum seen in figure 2.16.

This is a problem which is difficult to correct for the $I^{-.8}$ ion. You can adopt schemes for constructing the coarse grained density field that include solvent density in some way but these schemes all introduce their own artifacts and don't fix the problems. However, we can still address the basic question of whether or not there is a connection between solvation entropies and restricted interface fluctuations by just using a smaller ion. We will use an ion with the same Lennard-Jones parameters as a water molecule, this way it will occupy nearly the same space as a water molecule and interfere with the coarse grained density field in a minimal way. Ions of this size only adsorb to the surface if they have a charge less than about 0.6 e and we will therefore study and ion with a charge of -0.5 e. Figure 2.22 shows the entropy profiles computed for this ion from the harmonic analysis with three different values of the grid spacing. This ion is generally much less sensitive to the grid spacing than the larger one, and although there still is an entropy peak a few $\mathring{A}$ below the interface it is much smaller and it is not the dominant feature.

2.7 Fluctuations near other surfaces

The connection that we attempted to establish in the last section between solvation thermodynamics and fluctuations in the geometry of the air-water interface is somewhat

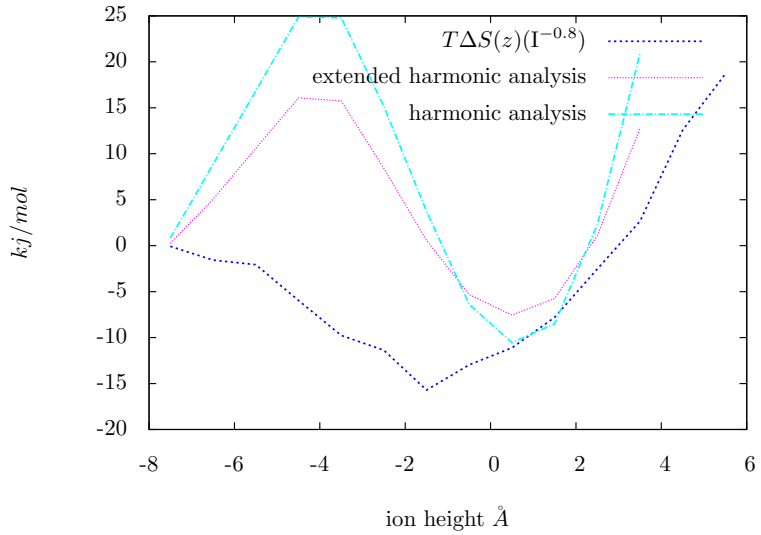

(a)

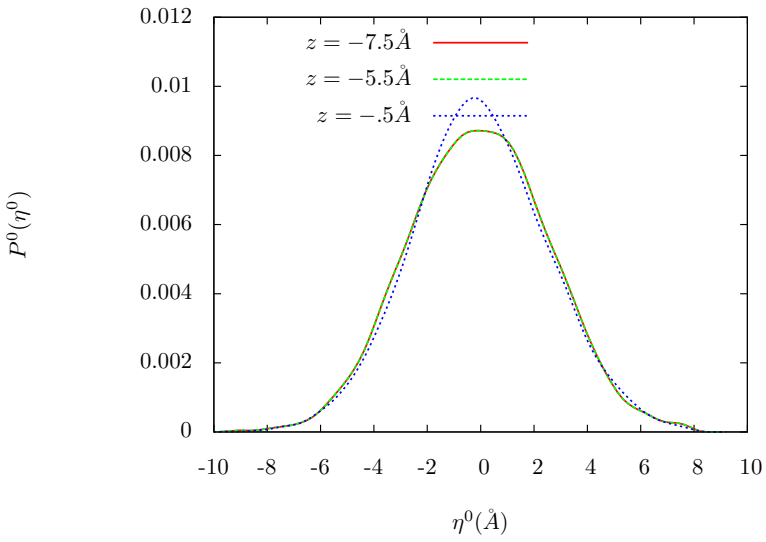

(b)

Figure 2.19: In figure a, entropy profiles for moving the $\mathrm{I}^{-.8}$ ion across the water-vapor interface along with the harmonic analysis and extended harmonic analysis approximations to this. Each variant of the harmonic analysis is very similar, indicating that fluctuations are approximately gaussian. Figure b shows the probability distribution of the projection on to the eigenvector with the largest eigenvalue, for three different ion heights. By eye these probability distributions are approximately gaussian.

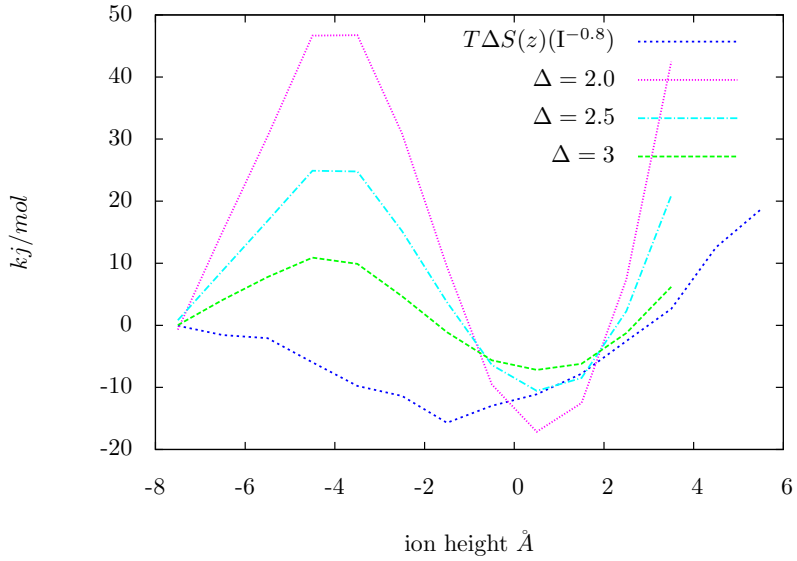

Figure 2.20: The entropy profiles calculated from the harmonic analysis for three different values of the grid spacing.

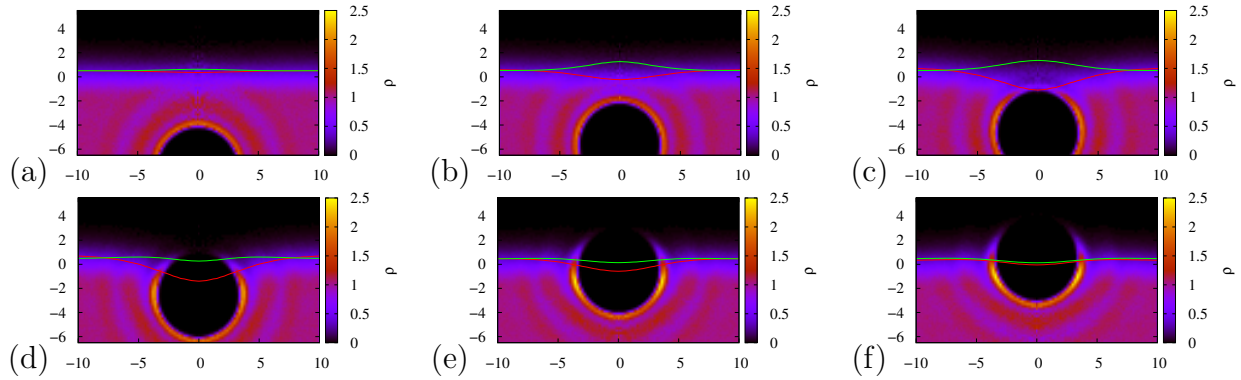

Figure 2.21: These figures show average solvent density as a function of perpendicular distance from an $\mathrm{I}^{-.8}$ ion and vertical distance from the GDS for various positions of the ion. The solvent density map here is just the density of oxygen atoms, it is not the coarse-grained solvent density field used to find the Willard interface. The red lines are the average height of the interface and the green lines show the mean squared fluctuations of the surface $\langle(\delta h(x))^2\rangle$. Note how, when the ion is at $z = -5$ (figure c) the average interface starts to penetrate the interior of the ion, and this corresponds to an increase in fluctuations.

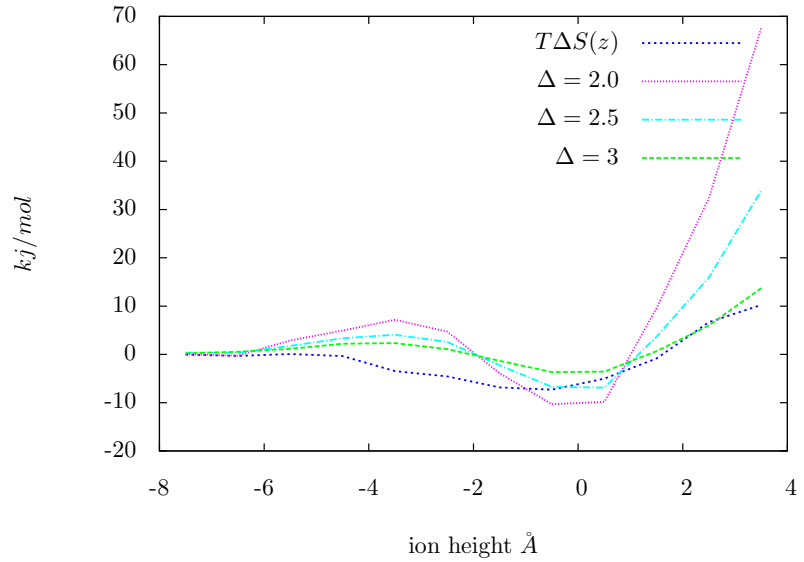

Figure 2.22: The entropy profiles calculated from the harmonic analysis for three different values of the grid spacing for a water molecule sized ion with a charge of -0.5 e, along with the true entropy profile for this ion. The harmonic analysis is still not be perfect, but for this ion it is generally much less sensitive to the grid spacing. The lines are labeled according to the grid spacing used (in $\AA$).

imperfect. In this section we present a different and perhaps slightly more compelling set of evidence for this connection. The question we ask in this section is, if the entropy minimum associated with placing the ion at the interface is associated with quenching capillary waves, can we remove this effect by quenching capillary waves altogether. There is no completely straightforward way to quench capillary waves but we've attempted to do this with two different approaches. The first of these is replacing the air-water interface with a wall that has some attraction for water molecules, and the second of these is confining the slab of water between two hard walls such that the overall density matches the bulk density.

One naturally expects that the interface between water and a slightly attractive wall should be fluctuating less than the interface between water and vapor. Problems like this are fairly well studied in the context of hydrophobic solvation and one of the surprising things is that certain measures of fluctuations, like $P_v(N)$ do not change too much when we add a weak attraction. If, however, the slightly attractive wall has even a weak effect on the fluctuations of the interface we might expect this to show up in the entropy profile for an ion like the $I^{-.8}$ studied above. We have studied the adsorption thermodynamics of the $I^{-.8}$ near a flat wall, which interacts with water molecules in the following way:

$$U(z_O) = 4\epsilon_w \left[\left(\frac{\sigma_w}{z_O - z_w} \right)^{12} - \left(\frac{\sigma_w}{z_0 - z_w} \right)^{6} \right], \tag{2.46}$$

where z_w is the position of the wall, ϵ_w is the strength of the attraction, σ_w dictates the length scale of the attraction and z_O is the position of the oxygen atom. We've chosen values of $3.5\mathring{A}$ for the parameter σ and 1.95 kj/mol for the parameter ϵ_w which means that the length scale of the interaction is on the order of one water molecule and the strength of the interaction is just shy of a $k_{\mathrm{B}}T$. This interaction is strong enough that the interfacial profile is narrower (indicating that fluctuations are suppressed) but not so strong as to induce significant layering in the density profile of water. Figure 2.23 shows how the solvent density depends on the perpendicular distance from the ion and the vertical distance from the attractive wall for a variety of ion heights. Figure 2.24 shows the same thing except for an air-water interface. The interface is noticeably narrower close to the attractive wall, and its average geometry does not change as much in response to the ion, but there is not significant layering of the solvent density.

Figure 2.25 shows the entropy and free energy profiles for transferring an $\mathrm{I}^{-.8}$ ion to the attractive wall described above, as well as the same profiles for transferring the ion to the free air-water interface for reference. The entropy minimum is indeed shallower near the sticky wall, even with this very weak attraction. The free energy minima are nearly equal, but they have very different temperature derivatives as indicated by the entropy and will therefore be different at higher temperatures.

Figure 2.26 shows the equivalent free energy and entropy profiles for a slab confined between two hard walls. In this case we see quite a dramatic reduction in the entropy minimum and a corresponding increase in the free energy minimum.

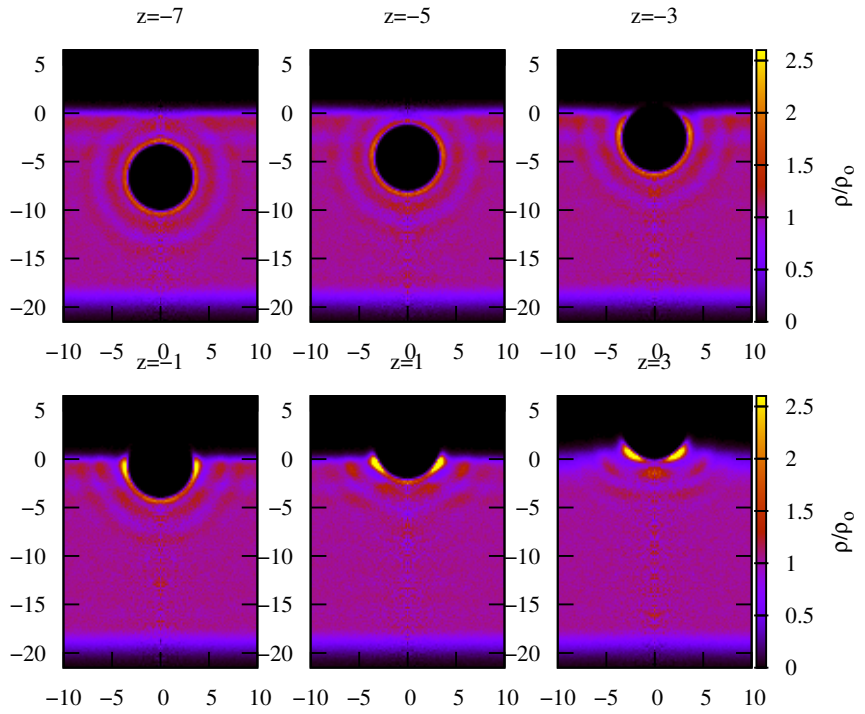

Figure 2.23: Solvent density as measured by oxygen atom density, as a function of perpendicular distance from the ion and vertical distance from the interface, for various different heights of the $I^{-.8}$ ion. In this case the interface is the slightly attractive wall described in the text.

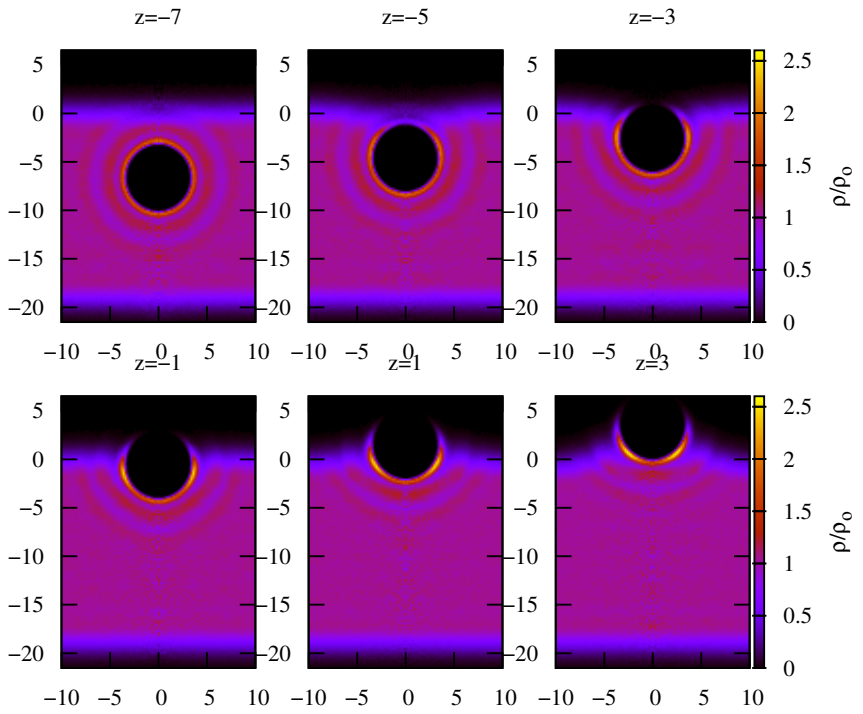

Figure 2.24: Solvent density as measured by oxygen atom density, as a function of perpendicular distance from the ion and vertical distance from the interface, for various different heights of the I^{-}.[8] ion. In this case the interface simply the air-water interface.

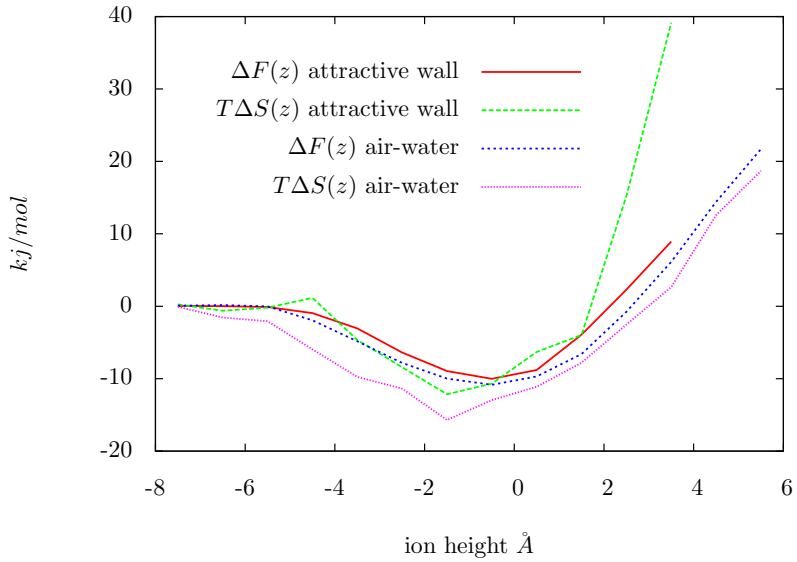

Figure 2.25: Free energy and entropy profiles for adsorption of the $I^{-.8}$ ion to the attractive wall described in the text, along with the same quantities for an air-water interface for comparison. The entropy minimum is significantly reduced, even for this very weak attraction.

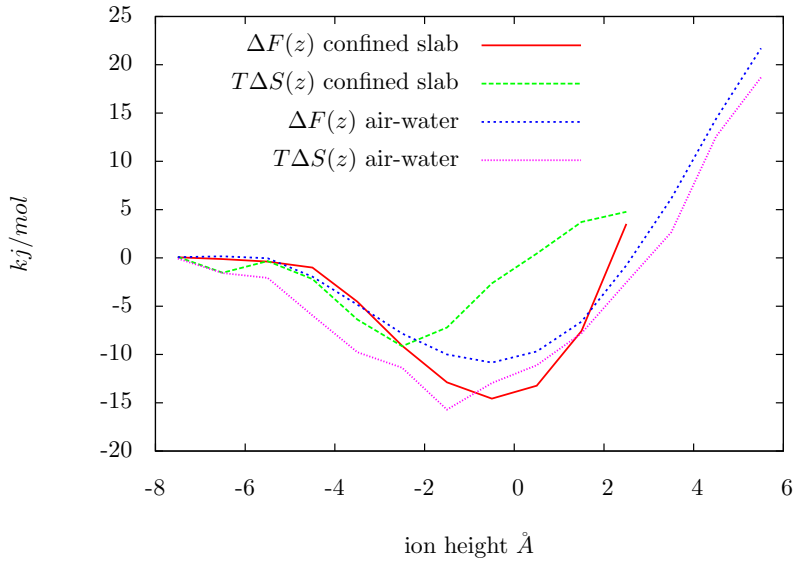

Figure 2.26: Free energy and entropy profiles for adsorption of the $I^{-.8}$ ion to a hard wall, along with the same quantities for an air-water interface for comparison. The entropy minimum is significantly reduced and the free energy minimum is noticeably deeper.

Chapter 3

Charge Asymmetry

3.1 Preliminaries

In the last chapter we described some of the general features of charged solute adsorption to liquid vapor interfaces. The fact that surface adsorption has both negative energies and entropies for a variety of ions in both water and the stockmayer fluid is surprising, but we argued that the physical origins of these trends are both relatively simple and fairly ubiquitous in liquids. They are in fact so general that even a simple lattice gas model for solute adsorption can capture them [60]. However, the remarkable feature of the way that ions interact with air-water interfaces is not really its generality but its specificity. Small changes to the physical parameters of an ion can modulate significant increases or decreases of ion density near the surface. Perhaps the most dramatic example of this sensitivity is the cation-anion asymmetry. It is generally accepted that anions have a stronger surface preference than cations, and changing the charge of an ion from positive to negative can indeed increase surface density by a factor of up to 1000. Figure 3.1 illustrates this effect for an ion with a hard core radius of 3.3 $\mathring{A}$ and $q \pm 0.6$e. However this effect is highly dependent on both the magnitude of the charge and the size of the ion. For certain parameters this effect even goes in the other direction in that the anion has a weaker surface affinity than the cation. There is no naive or simple way to predict the effect of inverting the sign of the charge as suggested in many papers [4, 3].

3.2 Some technical details

In this chapter we will be studying ion solvation thermodynamics across a much broader range of parameters than in the previous chapter. Rather than studying a few parameters in detail we will be studying ions with hard core radii ranging from 2.4 $\mathring{A}$ to 3.85 $\mathring{A}$, and charges ranging from -1.6 to 1.6 e. We study ions with a hard core repulsion rather than a Lennard-Jones potential in order to isolate cavity formation and charging free energies in the simplest way possible. For ions with a Lennard-Jones potential it is often the case that

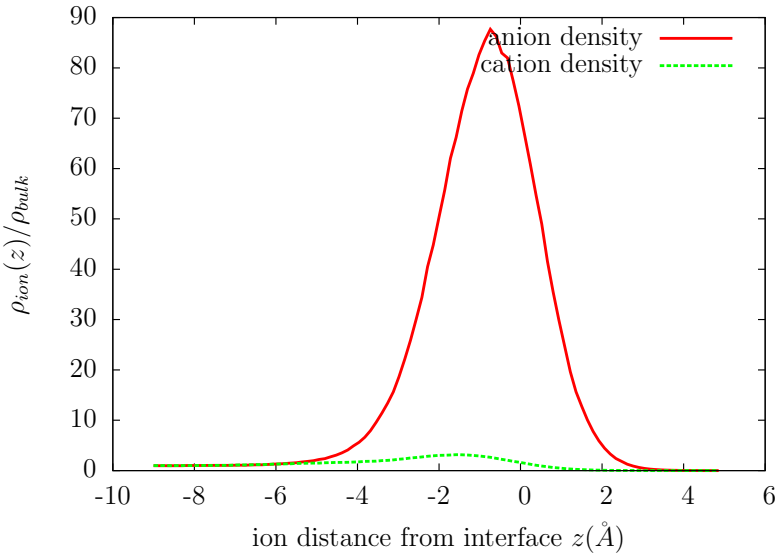

Figure 3.1: Density profiles for two ions which are identical apart from the sign of the charge. The anion has a very strong affinity for the surface while the cation has almost no affinity for the surface. The ions studied here have hard core radii of 3.3 $\AA$ and charges of $\pm$ 0.6 e

.

an anion and a cation with the same LJ parameters have a different effective radius, and it is therefore harder to compare a cation and an anion in an unambiguous way. In this chapter we will focus almost exclusively on the charging free energy because we are mainly interested in the cation-anion asymmetry. As we saw in the last chapter, we can compute the charging free energy for any charge given the probability distribution of the electrostatic potential in an uncharged cavity using the identity

$$F_{es}(q) = -k_B T \ln \int d\phi' P_o(\phi'; z) \exp[-\beta q \phi']. \tag{3.1}$$

This equation is exact but if we want to use it over a very broad charge range then we need to know the probability distribution $P_o(\phi'; z)$ very accurately. This requires us to accurately sample values of the electrostatic potential that have a probability of nearly 10^{-200} in the unbiased ensemble. See figure 2.4 for an illustration. We use the MBAR method described in the previous chapter to sample these probability distributions (see equations 2.5 and 2.6). The form of the bias potentials is simply a linear coupling to the electrostatic potential where

$$V_l(\phi(z)) = q_l \phi(z), \tag{3.2}$$

and $\phi(z)$ is the value of the electrostatic potential at the center of the cavity. This means that simulations conducted in the biased ensembles are simply simulations where the cavity carries a charge. We conduct many such simulations and use MBAR to reconstruct the

unbiased probability distribution. For the different biased ensembles we used values of q between 1.6 and -1.6 e, separated by 0.2 e except for the smallest ion studied, where it was necessary to use a q spacing of 0.1 e to obtain thorough sampling. In all of the work described in this chapter we only studied a small collection of ion heights z, typically just one position in bulk and a few positions near the Gibbs dividing surface.

3.3 Surface potentials and linear response

Discussions about the nature of the force that stabilizes anions at air-water interfaces usually focus on a quantity called the surface potential. This quantity is defined by the equation

$$\phi_{sp} = 4\pi \int_v^l z\rho(z)dz, \tag{3.3}$$

where $\rho(z)$ is simply the average charge density, v is a point in the vapor and l is a point in the liquid. This equation computes the difference between the average electrostatic potential in the bulk liquid and the average electrostatic potential in the vapor phase. This quantity is difficult to measure experimentally but it has been studied thoroughly in simulations [31, 4, 13]. For most atomistic models of water ϕ_{sp} has a value of about -0.5 V. This amounts to an energy drop of roughly 50 kj/mol for bringing a negative charge from the bulk liquid to the vapor. Likewise, it is an energy penalty of the same magnitude to bring a positive charge into the vapor phase. Figure 3.2 shows the charge density of neat liquid SPC/E water along with the mean electrostatic potential associated with this charge density.

The large value of the surface potential seems like a compelling argument that there is a large charge asymmetric force acting on ions as they cross the liquid-vapor interface. It is perhaps natural to associate this surface potential with an orientational bias on water molecules at the surface under the assumption that water molecules with no orientational bias would interact with positive charges and negative charges in the same way. This sort of reasoning has a key flaw that was exposed by Wilson, Pohorille and Pratt [64]. They pointed out, following Jackson [29], that there are contributions to the surface potential even when there is no orientational bias. Their reasoning starts from the observation that you can write a multipole like expansion of the charge density

$$\rho(z) = -\frac{d}{dz}\left[P_z(z) - \frac{d}{dz}Q_{zz}(z) + ...\right]. \tag{3.4}$$

In this expression $P_z(z)$ is the average molecular dipole density, it is computed from the equation

$$P_z(r) = \langle \sum_{n=1}^{N} \delta(r - r_n)\left[\int dr' \rho_n(r')z'\right]\rangle, \tag{3.5}$$

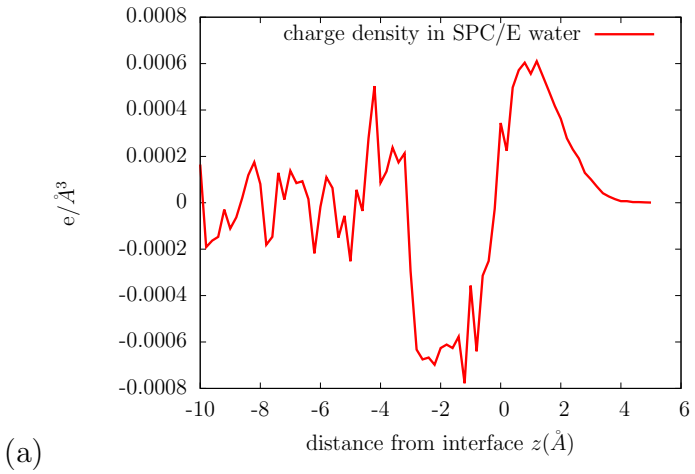

(a)

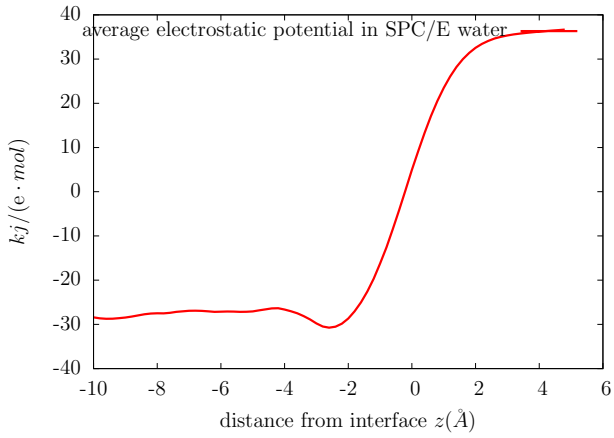

(b)

Figure 3.2: In (a), the charge density near a neat liquid vapor surface. This charge density arises purely from the internal charge distributions of solvent molecules because there are no solutes present. The potential at a point z is obtained by integrating over this charge density according to equation 3.3, this is shown in b.

where N is the number of solvent molecules, r_n is the center of solvent molecule n and $\rho_n(r')$ is the charge distribution of molecule n (which in general depends on the orientation of the molecule). The term in brackets is the dipole of the molecule, and it averages to zero if the system is isotropic. $Q_{zz}(z)$ is called the density of molecular quadrupoles but its definition is actually slightly different from the standard quadrupole. It is

$$Q_{zz}(r) = \langle \sum_{n=1}^{N} \delta(r - r_n) \left[\int dr' \rho_n(r') z'^2 \right] \rangle. \tag{3.6}$$

To compute the zz component of the standard quadrupole tensor you would integrate over the charge density times $z^2 - \frac{1}{3}r^2$ and not just z^2. The standard quadrupole would be zero for a spherically symmetric charge distribution, but this is not necessarily true of the quantity defined in equation 3.6. Consider a charge distribution which consists of a delta function positive charge q at the origin surrounded by a sphere of radius a of uniformly distributed negative charge with charge density $-\frac{3q}{4\pi a^3}$. The term in brackets in equation 3.6 would be

$$\left[\int dr' \rho_n(r') z'^2 \right] = \int_{sphere} dr' q\delta(r') z'^2 - \int_{sphere} dr' \frac{3q}{4\pi a^3} z'^2 = \frac{-qa^2}{25}, \tag{3.7}$$

which implies that Q_{zz} in the liquid has the nonzero value of $\rho_l \frac{-qa^2}{25}$, where ρ_l is the bulk liquid phase density. If we substitute equation 3.4 into equation 3.3, and integrate by parts, we can rewrite ϕ_{sp} as

$$\phi_{sp} = 4\pi \int_v^l P_z(z) dz - 4\pi \left[Q_{zz}(l) - Q_{zz}(v) \right]. \tag{3.8}$$

The first term in this equation depends on the orientations of molecules at the surface, the second term in this equation does not. It depends only on the quadrupole density in the isotropic liquid and the vapor phases. This result is very counterintuitive. It implies that even molecules with spherical symmetry can have a nontrivial charge distribution at the surface, and it also implies that charges will feel a potential drop or increase in crossing this surface. Figure 3.3 illustrates how even a very simple charge distribution can lead to charge layering at the surface. Models like these were studied extensively by Harder and Roux and they do indeed have large surface potentials [18]. This leads immediately to an apparent contradiction. Finite size ions, which are excluded from the interior of the molecules, will not interact electrostatically with any of the molecules in any way, and they cannot experience an electrostatic potential change in crossing the surface. The finite size of the ion breaks translational symmetry in the direction perpendicular direction to the interface, which means that equations 3.3, 3.4 and 3.8 are no longer strictly valid, but it still seems like the charge at the center of the cavity should have a long range interaction with the charge distribution at the interface. The resolution of this contradiction is that the molecules neighboring the cavity will give rise to charge layering around the cavity itself,

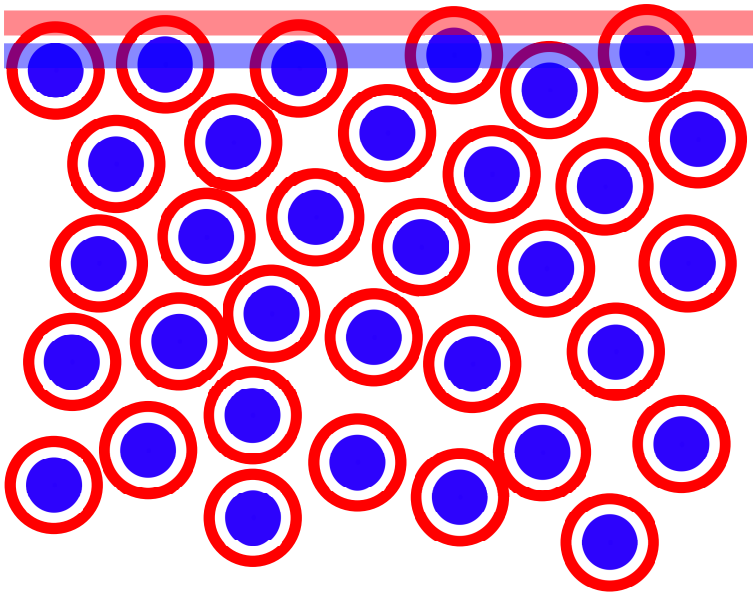

Figure 3.3: An illustration of the counterintuitive way in which spherically symmetric charge distributions can give rise to charge layering at the surface. The red circles represent the positive part of a molecular charge distribution and the blue circles represent the negative parts of that charge distribution. The transparent red layer at the top is a region in which there is excess positive charge and the transparent blue layer is a region in which there is excess negative charge.

and the interaction of the charge at the center of the cavity with these two separate charge distributions will effectively cancel. Point charges, however, penetrate the molecular interiors and therefore will have electrostatic interactions with the spherically symmetric molecules. Because they don't break translational symmetry, equation 3.3 is exact and it describes the electrostatics entirely in terms of the charge distribution at the surface, even though the interaction between the point charge and individual molecules is entirely local.

This discussion highlights the fact that the surface potential contains significant contributions from the interior charge distribution of the solvent molecule, and this contribution is irrelevant when considering finite size solutes. It is perhaps not so surprising then, that quantum models (which have a much more detailed internal charge distribution), have very different surface potentials. Recently reported values are on the order of 3V, which has the opposite sign of the -0.5V seen in classical simulations [31]. The ambiguities in interpreting the surface potential can be sidestepped by looking at the mean electrostatic potential inside a cavity. This quantity has direct relevance to ion solvation thermodynamics. To see this, recall that we can determine the charging free energy from equation 3.1 if we know the distribution of the potential inside a cavity $P_o(\phi; z)$. And if we assume a gaussian form for this distribution with mean $\langle\phi\rangle(z)$ and variance $\langle(\delta\phi)^2\rangle(z)$ then the charging free energy is

$$F_{es}(z,q) \simeq q\langle\phi\rangle(z) - \frac{1}{2}\beta q^2\langle(\delta\phi)^2\rangle(z) = F_{gauss}(z,q). \tag{3.9}$$

If we compare a positive and a negative charge of the same magnitude then the second order terms cancel and we are left with

$$F_{es}(z,q) - F_{es}(z,-q) \simeq 2q\langle\phi\rangle(z). \tag{3.10}$$

The assumption that $P_o(\phi)$ is gaussian is one of the assumptions underlying dielectric continuum theory (for a thorough discussion of the connection between gaussian fluctuations and DCT see chapter 5), so in a dielectric continuum the above equation would be exact. The quantity $F_{es}(z,q) - F_{es}(z,-q)$ is something we'll be using a lot so we'll give it a nice compact definition:

$$F_{\Delta q}(z,q) \coloneqq F_{es}(z,q) - F_{es}(z,-q). \tag{3.11}$$

In light of the discussion of surface potentials above, a natural question is what structural features of the solvent are responsible for the value of $\langle\phi\rangle(z)$. If it's mainly determined by something long range, like an orientational bias of water molecules at the interface, then you might expect charge asymmetric behavior to be relatively uniform for a broad class of ion parameters because this orientational bias will be fairly independent of things like ion size, charge and polarizability. On the other hand, if the value of $\langle\phi\rangle(z)$ has more to do with the local arrangement of water molecules around the cavity, then it may be very sensitive to the physical parameters of the ion. To address this issue we can spatially resolve contributions to $\langle\phi\rangle(z)$ by measuring the average interaction between a water molecule and a positive test charge at the center of an uncharged cavity. The coordinate system used is almost identical to the coordinate system shown in figure 2.8, except in this case the variable h is the vertical distance between the water molecule and the ion, not the interface. We will refer to the average interaction between a water molecule and the positive test charge at height z as $\bar{v}_{is}(x,h,z)$. The average electrostatic potential at the center of the cavity can be obtained as an integral over this quantity from the equation

$$\langle\phi(z)\rangle = \int_0^L \pi x dx \int_{-L}^{L} dh \rho_s(x,h,z)\bar{v}_{is}(x,h,z). \tag{3.12}$$

In figure 3.4 we look at $\rho_s(x,h,z)\bar{v}_{is}(x,h,z)\pi x$ for a cavity in bulk and a cavity at the interface. For the cavity in bulk, we see large negative contributions to the potential from the solvation shell of the cavity, and positive contributions from the interfacial regions. This implies that the orientations of molecules at the interface are such that they interact favorably with an anion, which is the opposite of what you would naively expect based on the charge distribution in figure 3.2. The total potential in the center of the cavity in bulk is about 8 $kj/(\mathrm{e}\cdot mol)$, implying that the long range contributions are dominant. The fact that there is a mix of long range and short range features makes it difficult to predict how

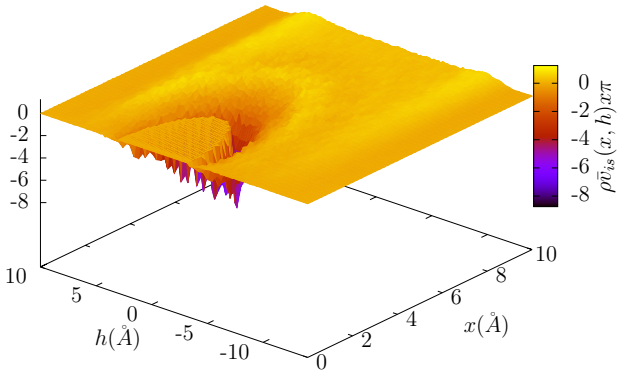

(a)

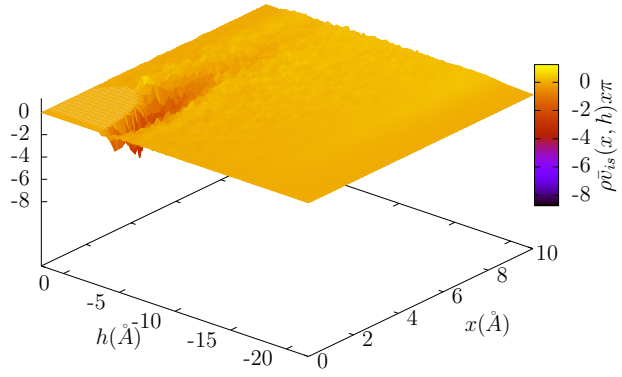

(b)

Figure 3.4: $\rho_s(x,h,z)\bar{v}_{is}(x,h,z)\pi x$ showing spatial contributions to $\langle\phi\rangle(z)$ for a cavity in bulk (a) and a cavity at the interface (b). Although there are competing long range and short range features, the dominant change when the cavity moves to the interface comes from the short range features.

$\langle\phi\rangle$ will change when the cavity is at the surface. As the ion crosses into the vapor phase the negative contributions from the coordination region should be much smaller, and figure b confirms this, implying that $\langle\phi\rangle$ should go up. The value of $\langle\phi\rangle$ at the surface integrates to about 18 $kj/(\mathrm{e}\cdot mol)$, and this indicates that the dominant change is from the short range features.

Figure 3.5 shows how the mean potential at the center of a cavity depends on height for a large height range and two different cavity sizes. There is some dependence on cavity size but in either case it is clear that the value of this potential is higher at the surface. To the extent that the linear response approximation is correct this implies a driving force that attracts anions to the interface and repels cations. As discussed above, one of the problems

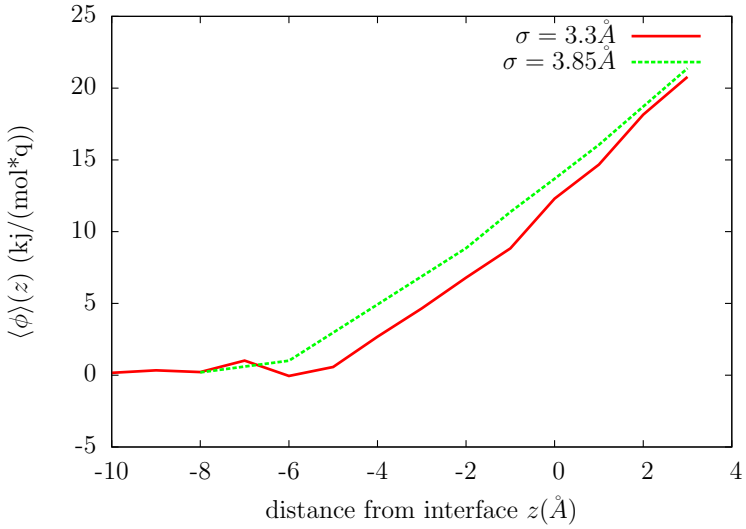

Figure 3.5: Average electrostatic potential inside a cavity as the cavity approaches the air-water interface. Results are shown for two cavity sizes, each of which has similar behavior. The average potential is normalized to zero in bulk.

with interpreting the surface potential is that it is very model dependent due to the internal charge distribution. Recent work has suggested that the mean potential in a center of a cavity is much less model dependent and even behaves similarly for quantum and classical models [4].

Whether or not you trust the gaussian approximation in equation 3.9 depends on what your criteria are because this equation makes several testable predictions. The simplest of these predictions is simply the charging free energy itself. Figure **??**a shows the charging free energy along with the gaussian approximation for an ion in bulk and an ion at the interface. In neither case can we expect quantitative accuracy from this approximation outside of a small range. Our previous results suggest differences of a few kj/mol are important and the errors clearly exceed this both in bulk and at the interface. However, it's possible that some of these errors cancel when we compare the bulk to the interface. The difference between the charging free energy at the surface and the charging free energy in bulk is shown in figure 3.6b. We will refer to this quantity as $\Delta F(q)$:

$$\Delta F(q) = F_{es}(z_i, q) - F_{es}(z_b, q) \simeq q\left(\langle\phi\rangle(z_i) - \langle\phi\rangle(z_b)\right) - \frac{1}{2}\beta q^2\left(\langle(\delta\phi)^2\rangle(z_i) - \langle(\delta\phi)^2\rangle(z_b)\right), \tag{3.13}$$

where z_i is a position at or near the interface and z_b is a position in bulk. This quantity does depend on precisely which value of z_i you choose but we will suppress this dependence for simplicity.

Quantitatively the gaussian approximation does slightly better for ΔF for charges be-

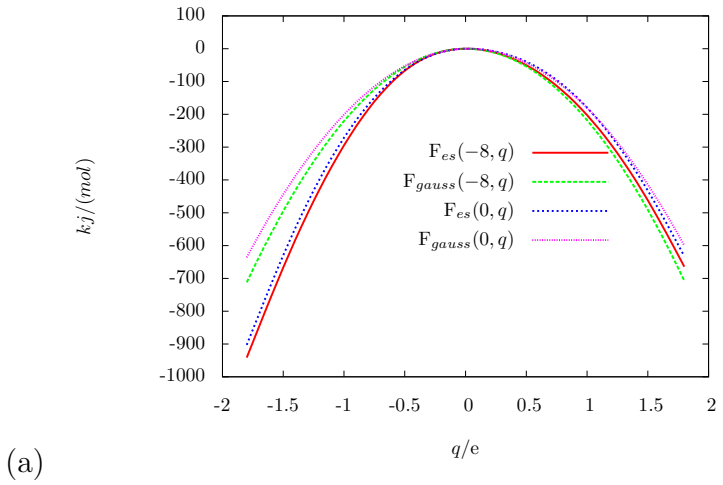

(a)

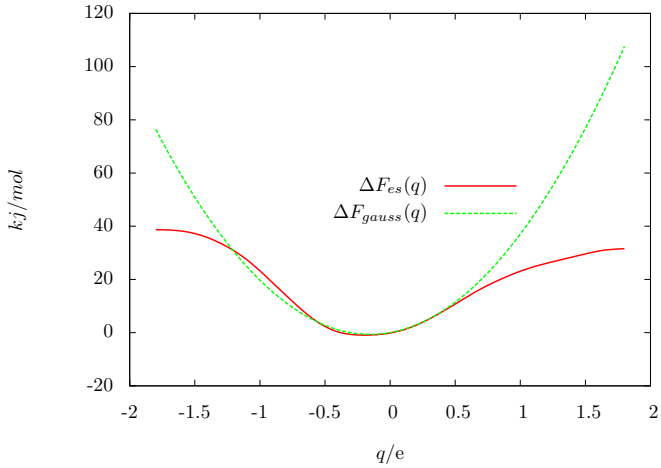

(b)

Figure 3.6: In figure a, the charging free energy for an ion with a hard core radius of 3.3 $\mathring{A}$ at the surface (z=0) and in bulk (z=-8), along with the gaussian approximations to these quantities. In figure b, the difference between the surface charging free energy and bulk charging free energy shown in figure a.

tween ±0.5e, but outside of this region there are serious qualitative errors. The curvature of ΔF actually changes sign for higher charges and it becomes much easier to solvate ions at the interface than predicted by the simple harmonic model. This is an example of a nonlinearity, we will discuss this more later and argue that it's related to the ability of the interface to deform around the ion.

As a final test of the gaussian approximation we can ask how well it predicts charge asymmetry according to equation 3.10. In figure **??** we test how well equation 3.10 predicts $F_{\Delta q}$ at the surface and in bulk for the same 3.3 $\mathring{A}$ ion. In neither case is equation 3.10 quantitatively accurate outside of a very small charge range. If we subtract the bulk value

from the surface value, however, we find that the Gaussian approximation is not too far off over a reasonable charge range. We we will refer to this quantity as $\Delta F_{\Delta q}(q)$. To be explicit it is given by:

$$\Delta F_{\Delta q}(q) = F_{\Delta q}(z_i, q) - F_{\Delta q}(z_b, q) \simeq 2q\left(\langle\phi\rangle(z_i) - \langle\phi\rangle(z_b)\right). \tag{3.14}$$

This quantity is extremely important because it dictates the relative densities of anions and cations at the surface according to the equation

$$\frac{\rho_{anion}(z_i)}{\rho_{cation}(z_i)} = \exp[\beta\Delta F_{\Delta q}(q)]. \tag{3.15}$$

Figure 3.8, shows explicitly the density ratios expected from both the true $\Delta F_{\Delta q}$ and the gaussian approximation. There is a sweet spot around 0.6 e where the anion density at the surface is about 30 times the cation density. For higher charges this value starts to decay and finally crosses 1 indicating that the cation density actually exceeds the anion density at the surface. There are some naive reasons to expect a decay like this. For real electrolyte solutions there are strong interactions between the ions and locally breaking charge neutrality has a very high energetic cost. However, the calculations described here completely neglect such interactions and these features are entirely due to nonlinearities in the individual ion solvation thermodynamics.

It is important to point out that for the ion size described in this section only charges between about -0.85 and +0.7 e are actually surface enhanced. One could argue that if we restrict our attention to this region then the behavior in 3.7b is not too poorly described by the linear response approximation, and that the behavior of ions at an interface that they would ordinarily avoid is irrelevant. Looking at the expanded parameter space exposes the fact that there are several effects competing with one another and we therefore cannot make quantitatively accurate predictions by only accounting for one effect. There are clearly forces that in some regimes prefer anions at interfaces, while there are other forces that prefer cations at interfaces, the fact that neither of these is dominant for physical ion parameters exposes a serious gap in our understanding.

3.4 An expanded set of ion parameters

The results of the last section raise obvious questions about how the charge asymmetric behavior depends on various parameters like ion size and temperature. If we had found that the gaussian approximation was fairly good at describing charge asymmetry then we might reasonably conclude that not much would change when we study different ion sizes or different ion heights. We would just need to know the average and variance of the electrostatic potential inside of the cavity. The fact that there are dramatic nonlinearities implies that some of the features in figures 3.6 and 3.7 may be sensitive to perturbations. In this section

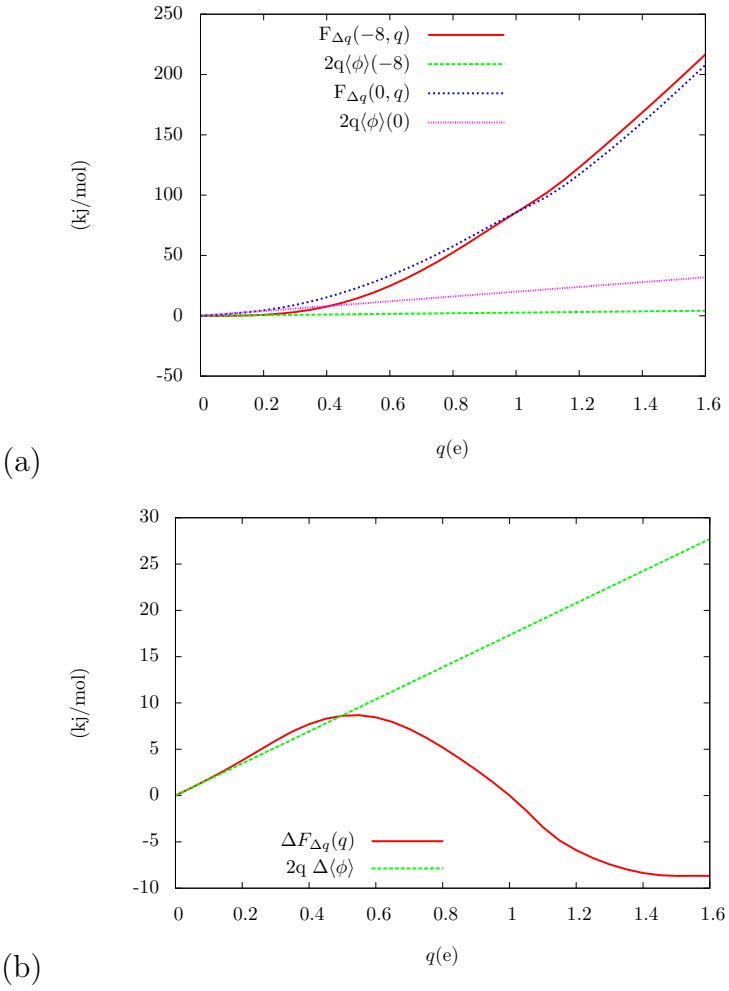

Figure 3.7: In figure a is shown $F_{\Delta q}(q)$ for an ion in bulk and an ion at the interface along with the gaussian approximation. Figure b shows $\Delta F_{\Delta q}(q)$ for the two ion heights shown in figure a. This quantity has a non monotonic dependence on q and changes sign around q=1, indicating a crossover from the anion being favored to the cation being favored at the interface.

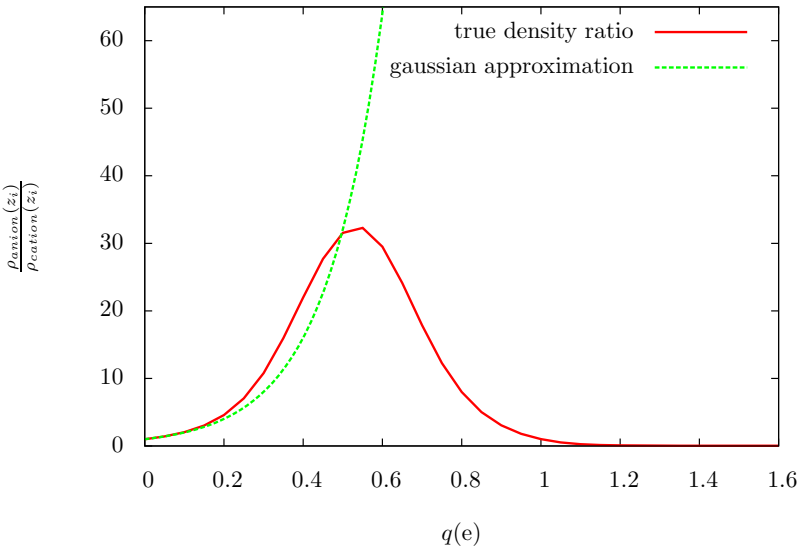

Figure 3.8: Ratio of anion density at the surface to cation density at the surface along with the gaussian approximation for this quantity. This is calculated from solvation free energies of individual ions, and therefore does not include interactions between ions at finite ionic strength.

we explore this behavior over a broader range of parameters to see what sort of patterns emerge.

In this section we look at a slightly different quantity than those presented above. Equation 3.14 both defines $\Delta F_{\Delta q}$ and provides the gaussian approximation. This approximation suggests the definition

$$\Delta F_{\Delta q}(q) = 2q\psi(q,\sigma), \tag{3.16}$$

where σ is the size of the ion. $\psi(q,\sigma)$ serves as an analogue for the quantity $(\langle\phi\rangle(z_i) - \langle\phi\rangle(z_b))$, and it obeys the important limit

$$\psi(0,\sigma) = (\langle\phi\rangle(z_i) - \langle\phi\rangle(z_b)) \tag{3.17}$$

It therefore gives us a convenient and compact measure of the nonlinearity.

Figure 3.9 shows this quantity as a function of q for three different cavity sizes and two different temperatures. The three cavity sizes are 2.4 $\mathring{A}$, 3.3 $\mathring{A}$ and 3.85 $\mathring{A}$. These were mainly chosen to cover the entire range of interesting parameters rather than to match any specific physical ions but the smallest is about the size of a sodium ion, the middle one is about the size of a bromide anion and the largest one is slightly larger than an iodide anion [14]. The ion heights were the same for all three ions and were chosen to be $z_i = 0.5\mathring{A}$ and $z_b = -9.5\mathring{A}$. The low temperature simulations were conducted at 250K which is below the freezing point of real water but is substantially higher than the freezing point of SPC/E

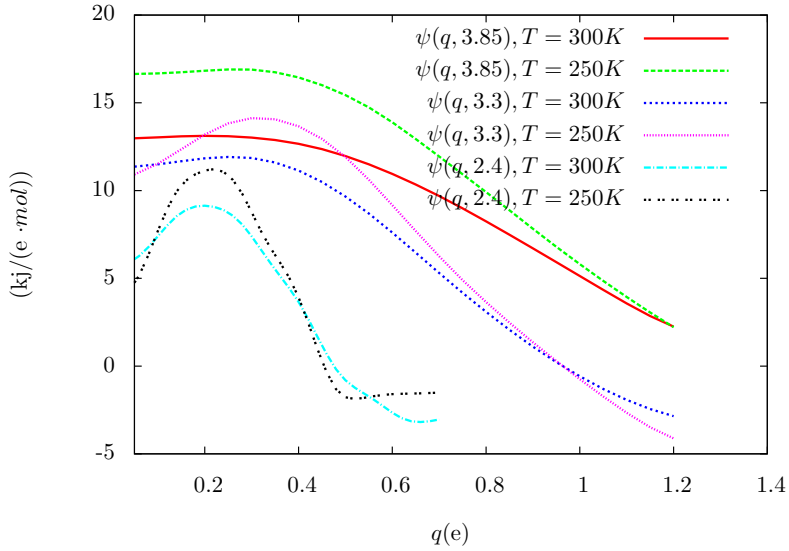

Figure 3.9: The quantity $\psi(q, \sigma)$ described in the text for ions with hard core radii of 2.4, 3.3 and 3.85 $\mathring{A}$, and at two different temperatures of 300K and 250K.

water. We deliberately chose this very low temperature to make the temperature dependence very clear across the whole charge range and size range.

There are several interesting features of figure 3.9. Perhaps the simplest evident trend is that the value of ψ tends to increase with ion size. ψ also tends to increase as you lower the temperature. This is a rule for the largest cavity but has clear exceptions for the smaller two cavities at very low and high charges. Perhaps the most surprising feature in these results is the way that ψ is at first an increasing function of charge for the smaller two ions. This is an indication that the linear response approximation actually underpredicts the degree to which the anion is favored at the surface. This was slightly evident in figures 3.8 and 3.7 but we see it much more dramatically here.

3.5 Energetic and entropic features

We can use the temperature dependence in the curves above to estimate the energetic and entropic components of $\Delta F_{\Delta q}$ from the equation

$$\Delta S_{\Delta q} = -\frac{\Delta F_{\Delta q}(T_2) - \Delta F_{\Delta q}(T_1)}{T_2 - T_1}, \tag{3.18}$$

and

$$\Delta E_{\Delta q} = \Delta F_{\Delta q} + T\Delta S_{\Delta q}. \tag{3.19}$$

These equations assume that $\Delta E_{\Delta q}$ and $\Delta S_{\Delta q}$ are roughly independent of temperature over the relevant temperature range. It is not reasonable to expect this assumption to hold over the range 250K to 300K, so we've also directly computed $\Delta E_{\Delta q}$ at a few different values of q as a check for the 3.3 $\mathring{A}$ ion. The results of this analysis are shown in figure 3.10 for all three cavity sizes discussed above. The energies computed from the direct averaging (shown as the purple dots in figure 3.10b) and the temperature derivative to do not agree exactly as expected but they show the same basic trends.

All three cavity sizes exhibit similar trends. The peak in $\Delta F_{\Delta q}$ is associated with a much larger maximum in $\Delta E_{\Delta q}$ and a minimum in $-\Delta S_{\Delta q}$ indicating that the force which prefers anions at the interface has a very favorable energetic component and an unfavorable entropic component. This entropic component may be related to capillary waves, however, a capillary wave analysis like the one described in the last chapter yields similar results for both the anion and the cation. Later in this chapter we will present evidence that the anion and the cation have a similar effect on capillary waves. Perhaps more relevant is the fact that the anion and the cation have very different bulk solvation entropies. This effect is not very well understood but it is related to the constraints imposed on the hydrogen bonding network by the ion. These constraints are largest in the first and second solvation shells of the ion and this effect is therefore likely to be highly localized in space. As the ion crosses the interface the number of water molecules in its solvation shell starts to decrease, and the charge asymmetric effect on the hydrogen bonding network starts to decrease as well. If the magnitude of this decrease is c, we might schematically estimate the entropy change for bringing the ion to the surface as

$$\Delta S(q) = S(q, z_i) - S(q, z_b) = -cS_{bulk}(q) + S_{symm}(q). \tag{3.20}$$

The symmetric part is associated with capillary waves and cavity formation and other effects which might be relatively charge symmetric and it therefore cancels when we compute $\Delta S_{\Delta q}$:

$$\Delta S_{\Delta q}(q) \simeq -c\left(S_{bulk}(q) - S_{bulk}(-q)\right). \tag{3.21}$$

Figure 3.11 compares the right and left hand sides of equation 3.21 for the 3.3 $\mathring{A}$ and the 3.85 $\mathring{A}$ ion where we have arbitrarily set $c = 1$. For each cavity size, these two quantities have similar features. The correspondence is slightly better for the larger cavity but in either case it seems reasonable to conclude that the asymmetries in solvation entropies at the surface are connected to the asymmetries of the solvation entropies in bulk. The asymmetry in the bulk solvation entropies is itself an interesting question and one that I don't believe has been fully addressed. The peak in the red and the blue curves in figure 3.11 indicates that the bulk solvation entropy of the anion exceeds that of the cation by as much as 20 kj/mol. This is a substantial difference and it accounts for a large fraction of the difference between the total solvation free energies of the two ions.

We will now attempt to describe some of the energetic features in figure 3.10. In the last chapter we described a method for spatially decomposing contributions to the solvation

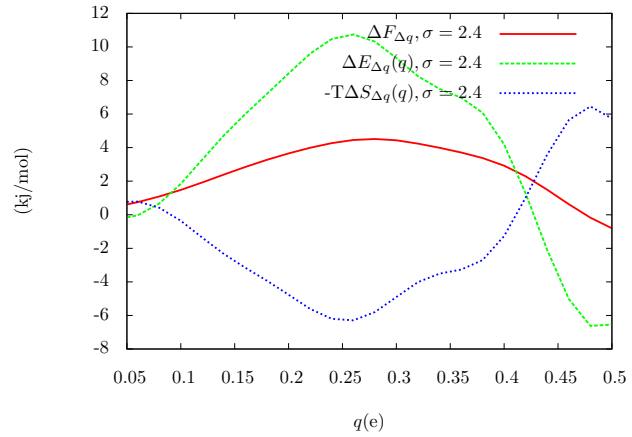

(a)

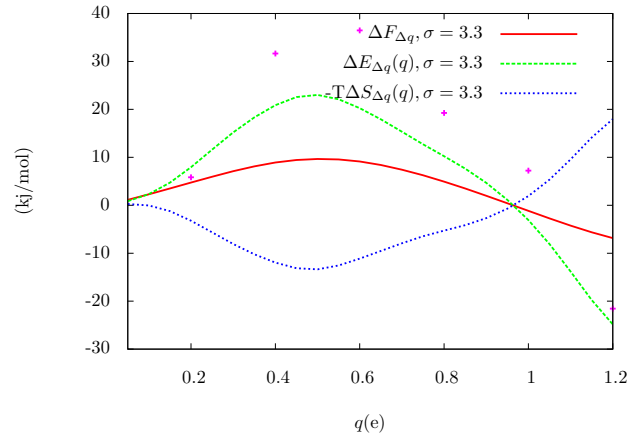

(b)

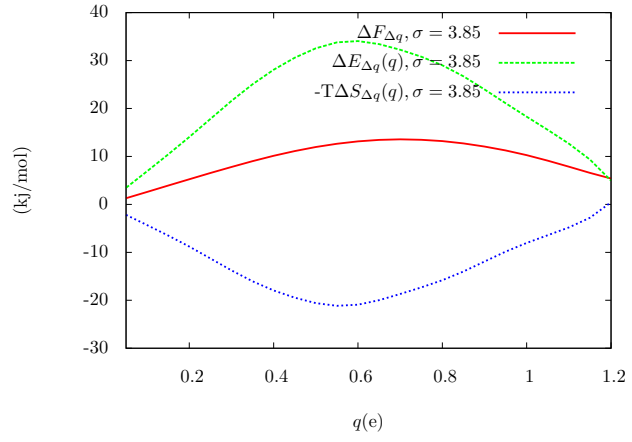

(c)

Figure 3.10: $\Delta F_{\Delta q}$ decomposed into its energetic and entropic components using its temperature dependence. Results are shown for all three cavity sizes studied in figure 3.9. Plot a shows the $\sigma = 2.4\mathring{A}$ cavity, figure b shows the $\sigma = 2.3\mathring{A}$ cavity and figure c shows the $\sigma = 3.85\mathring{A}$ cavity. The purple crosses in figure b show the $\Delta E_{\Delta q}$ computed directly from averaging at 300K.

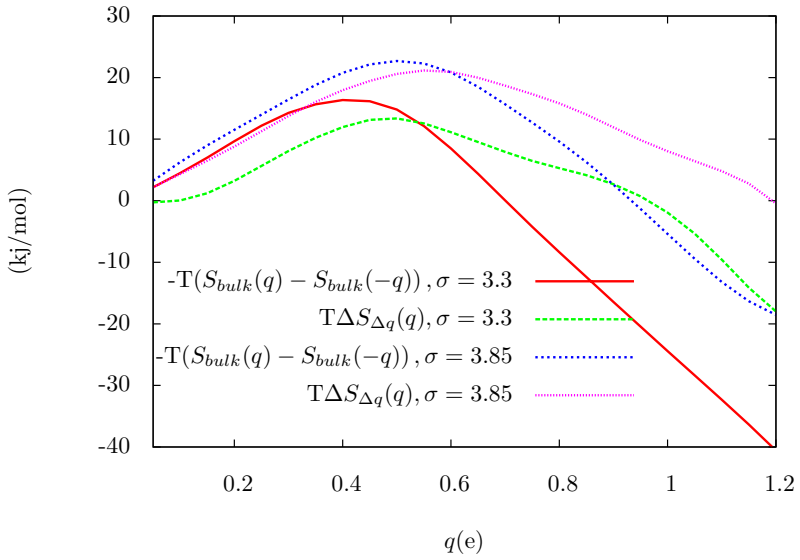

Figure 3.11: A comparison between $\Delta S_{\Delta q}(q)$ and $(S_{bulk}(q) - S_{bulk}(-q))$ for two different cavity sizes.

energy by measuring averages of pairwise interactions. We also described the local approximation, in which we computed the average interaction strengths of water molecules in three different regions: coordinating the ion, in bulk, and at the interface. We then showed that you can accurately reproduce the solvation energy curves simply by keeping track of how the number of water molecules in these three regions change. It seems logical to try to extend this analysis to the broader charge range and see if it provides any insight. The problem is that the local approximation is actually only successful in special cases. Figure 3.12 shows the local approximation applied to the hard core ion of 3.3 $\mathring{A}$ and charges of ± 0.6. This approximation describes the anion fairly well but does very poorly with the cation.

It is clear that a straightforward application of the local approximation will not be very useful for this problem. The approach we will adopt here is related to the local approximation in the sense that we consider contributions to the energy from molecules in the first or second solvation shell of the ion. Recall that in chapter 2 we derived the following exact decomposition of the average energy, E:

$$E(z,q) = n_{coord}(z,q)\bar{\mathcal{E}}_{coord}(z,q) + n_{surf}(z,q)\bar{\mathcal{E}}_{surf}(z,q) + n_{bulk}(z,q)\bar{\mathcal{E}}_{bulk}(z,q). \tag{3.22}$$

The local approximation then just assumes that the $\bar{\mathcal{E}}_i$ are independent of z. In this chapter we will allow for the fact that $\bar{\mathcal{E}}_{coord}$ has some dependence on ion height, but we will assume that the final two terms in the above sum do not depend on the sign of the charge of the ion. Therefore, if we want to compute the difference between the anion and the cation these two terms will cancel and we can focus exclusively on the coordination region. We have

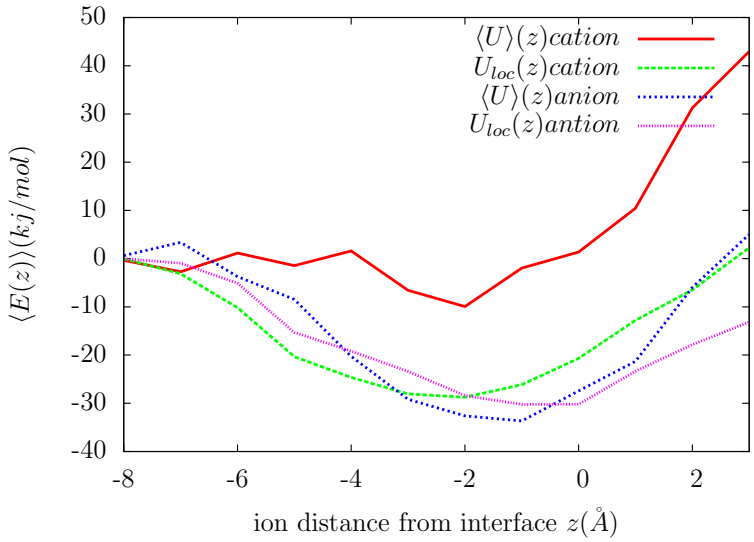

Figure 3.12: The local approximation applied to the hard core ions with $\sigma = 3.3\mathring{A}$ and charges of ± 0.6e, along with the true average energy change. The local approximation is much more successful for the anion then it is for the cation.

$$E_{\Delta q}(q,z) = E(z,q) - E(z,-q) \simeq n_{coord}(z,q)\bar{\mathcal{E}}_{coord}(z,q) - n_{coord}(z,-q)\bar{\mathcal{E}}_{coord}(z,-q). \quad (3.23)$$

For convenience we will define this approximation as $E^{coord}_{\Delta q}$:

$$E^{coord}_{\Delta q}(q,z) = n_{coord}(z,q)\bar{\mathcal{E}}_{coord}(z,q) - n_{coord}(z,-q)\bar{\mathcal{E}}_{coord}(z,-q). \quad (3.24)$$

Ultimately we are interested in the quantity $\Delta E_{\Delta q}$ which we will approximate as

$$\Delta E^{coord}_{\Delta q}(q) = E^{coord}_{\Delta q}(q,z_i) - E^{coord}_{\Delta q}(q,z_b). \quad (3.25)$$

Neglecting the surface and the bulk regions will clearly produce serious errors if we consider either ion individually, but these errors largely cancel when we consider the charge asymmetry. Figure 3.13 shows a set of energy density maps for an anion and a cation in bulk and at the interface. The cutoff defining the coordination region is indicated by the circle. By visual inspection, the changes that occur outside of the coordination region are nearly identical for the anion and the cation. We can also test equation 3.23 directly. Figure 3.14 shows $\Delta E^{coord}_{\Delta q}(q)$ and the true $\Delta E_{\Delta q}(q)$ as estimated from the temperature derivatives for the three different cavity sizes considered above. These figures show that there is excellent qualitative and even reasonable quantitative agreement. Each cavity size has a different cutoff used to define the coordination region. For the 2.4 $\mathring{A}$ cavity this cutoff is 4.1 $\mathring{A}$, for the 3.3 $\mathring{A}$ cavity it is 5.3 $\mathring{A}$ and for the 3.85 $\mathring{A}$ cavity it is 5.85 $\mathring{A}$.

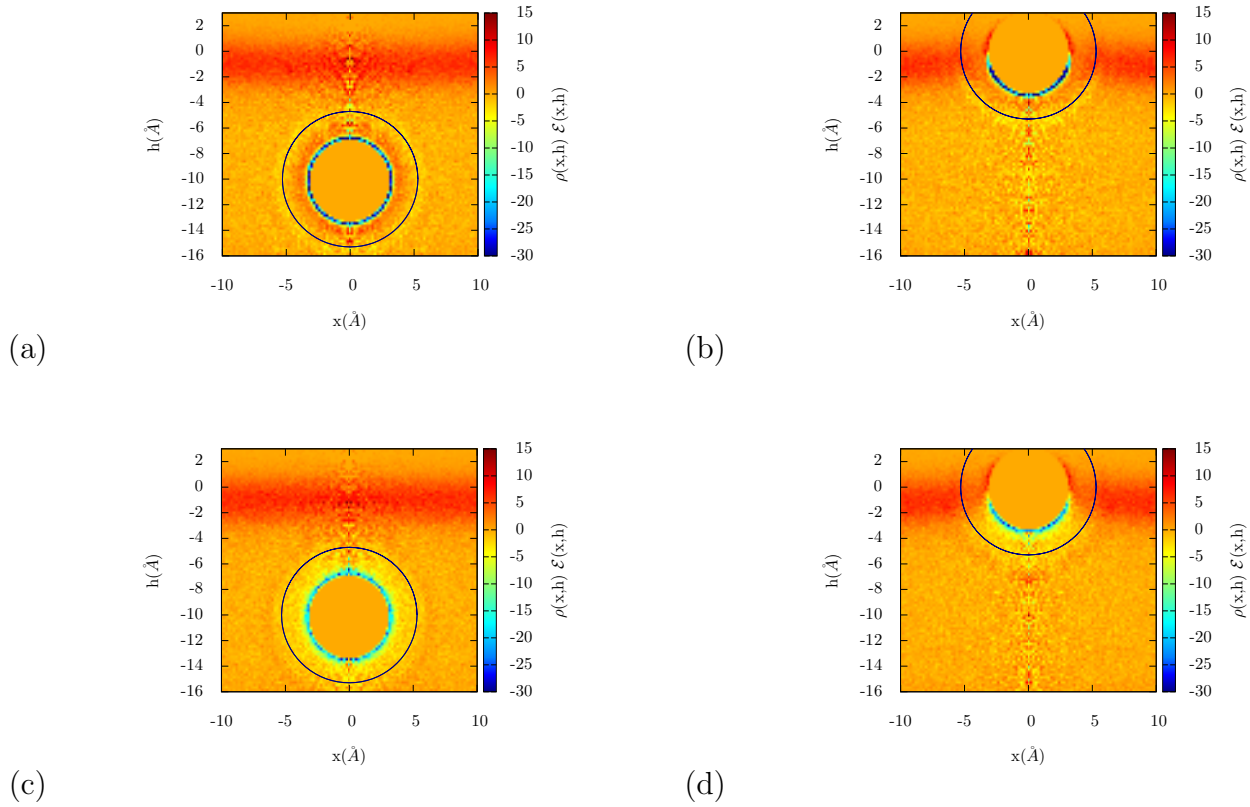

Figure 3.13: Energy density maps for a representative anion (plots a and b) and cation (plots c and d) both in bulk and at the interface. The ions shown here have a hard core radius of 3.3 $\mathring{A}$ and charges of ± 0.6. The blue circles represent the cutoff of the coordination region. The changes that occur outside of this region when you bring the ion to the surface are very similar for the anion and the cation.

The fact that we find similar qualitative features in figure 3.14 is perhaps not so surprising. In the last section we argued that the best measure of the charge asymmetry is not simply $\Delta F_{\Delta q}$, but instead this quantity scaled by $2q$, which we called ψ. And indeed, we see more dramatic qualitative differences between the different cavity sizes when we look at this quantity (see figure 3.9). We will therefore look at the energetic analogue of this quantity, which we call Θ and define by

$$\Theta(q) = \frac{\Delta E_{\Delta q}(q)}{2q}, \tag{3.26}$$

and

$$\Theta^{coord}(q) = \frac{\Delta E^{coord}_{\Delta q}(q)}{2q}. \tag{3.27}$$

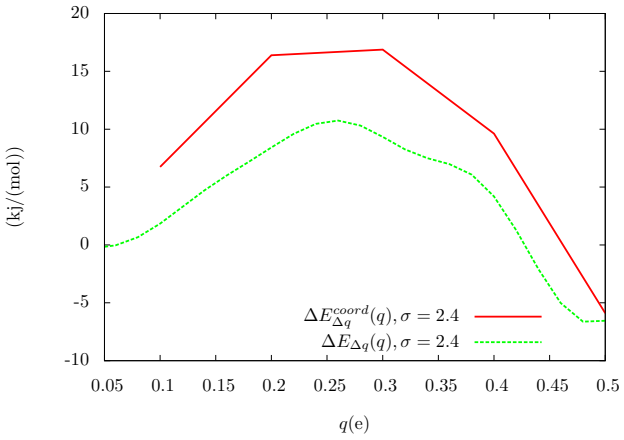

(a)

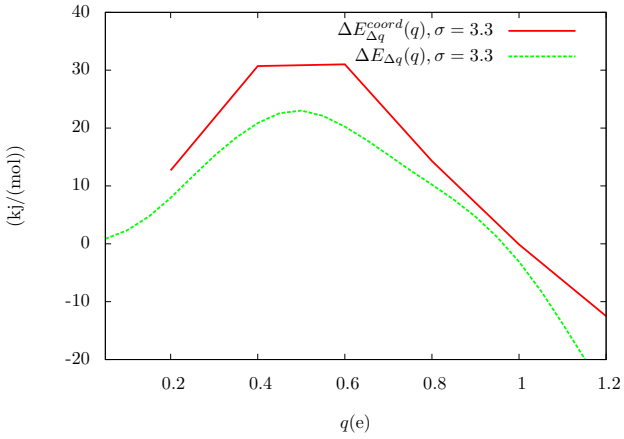

(b)

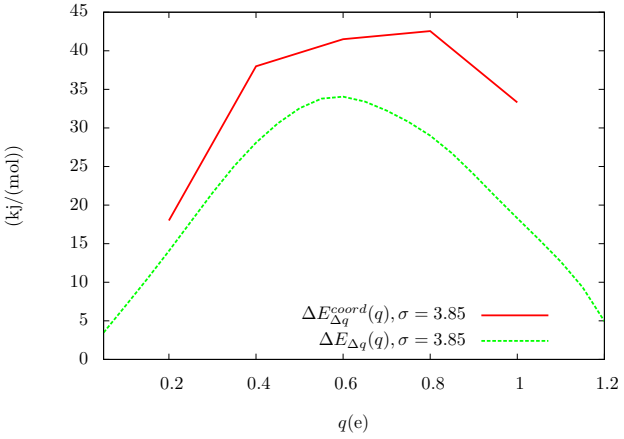

(c)

Figure 3.14: $\Delta E^{coord}_{\Delta q}(q)$ and $\Delta E_{\Delta q}(q)$ for the three different cavity sizes studied above (2.4, 3.3, 3.85 $\mathring{A}$ in plots a, b and c respectively). In each case the trends in $\Delta E_{\Delta q}(q)$ are well captured by just considering the coordination region. The quantitative errors are largely due to the fact that the average energies are computed from an imprecise temperature derivative (see figure 3.10.

Figure 3.15 shows these two quantities for all three cavity sizes studied throughout this section. Θ shows the same qualitative behavior as Ψ, where the smaller two cavity sizes have a steep increase for low values of q, indicating a large energetic preference for solvating the anion at the surface which exceeds the naive linear response prediction followed by a decline towards zero, when the cation starts to be favored at the surface. The local approximation to this quantity is imperfect, particularly at low charges, but it succeeds in capturing the qualitative differences between the different cavity sizes.

We can learn something about these trends by breaking down $\Delta E^{coord}_{\Delta q}(q)$ into components which have relatively simple interpretations. Consider the quantity $\Delta E^{coord}(q)$, which is defined by the equation

$$\Delta E^{coord}(q) = n_{coord}(z_i, q)\bar{\mathcal{E}}_{coord}(z_i, q) - n_{coord}(z_b, q)\bar{\mathcal{E}}_{coord}(z_b, q), \tag{3.28}$$

and measures the energy change in the coordination region when an ion moves from a position z_b in bulk to a position z_i at the interface. If we make the substitution

$$n_{coord}(z_i, q) = n_{coord}(z_b, q) + \Delta n_{coord}(q) \tag{3.29}$$

and

$$\bar{\mathcal{E}}_{coord}(z_i, q) = \bar{\mathcal{E}}_{coord}(z_b, q) + \Delta\bar{\mathcal{E}}_{coord}(q), \tag{3.30}$$

then equation 3.28 becomes

$$\Delta E^{coord}(q) = \Delta n_{coord}(q)\bar{\mathcal{E}}_{coord}(z_b, q) + n_{coord}(z_i, q)\Delta\bar{\mathcal{E}}_{coord}(q). \tag{3.31}$$

The first term here is the one that appears in the original local approximation and it says that the energetic penalty associated with losing molecules from the solvation shell of the ion is proportional to the average interaction strength of a molecule coordinating the ion in bulk. From the perspective of this term alone, the more strongly solvated an ion is in bulk, the more difficult it is to place it at an interface. The second term is slightly more complicated but its a rough measure of how much more strongly or weakly a water molecule in the coordination region is interacting with the other molecules when that ion is at the interface as opposed to bulk. If we recall the definition of $\bar{\mathcal{E}}_{coord}$ from equation 2.31 we see why this term is not so straightforward to interpret. It's an average of an interaction strength weighted by the density, which is very inhomogeneous when the ion is at the surface. This difficulty is likely to be the same or very similar for both the cation and the anion, and so by taking the difference between the two we may have a quantity with a straightforward interpretation. We will rewrite $\Delta E^{coord}_{\Delta q}(q)$ in terms of these two components as

$$\Delta E^{coord}_{\Delta q}(q) = \Delta E^{coord_1}_{\Delta q}(q) + \Delta E^{coord_2}_{\Delta q}(q) \tag{3.32}$$

where

$$\Delta E^{coord_1}_{\Delta q}(q) = \left(\Delta n_{coord}(q)\bar{\mathcal{E}}_{coord}(z_b, q) - \Delta n_{coord}(-q)\bar{\mathcal{E}}_{coord}(z_b, -q)\right) \tag{3.33}$$

and

$$\Delta E^{coord_2}_{\Delta q}(q) = \left(n_{coord}(z_i, q)\Delta\bar{\mathcal{E}}_{coord}(q) - n_{coord}(z_i, -q)\Delta\bar{\mathcal{E}}_{coord}(-q)\right). \tag{3.34}$$

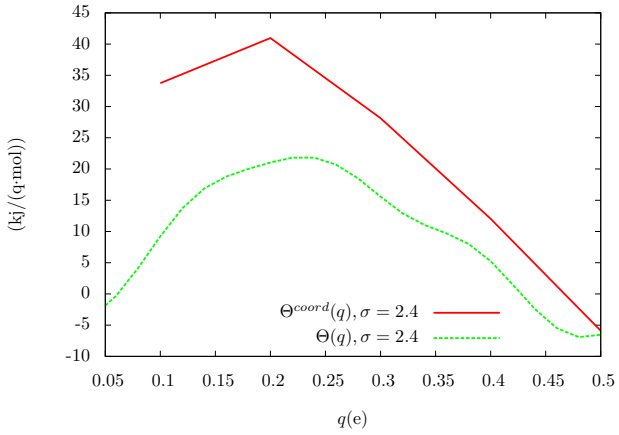

(a)

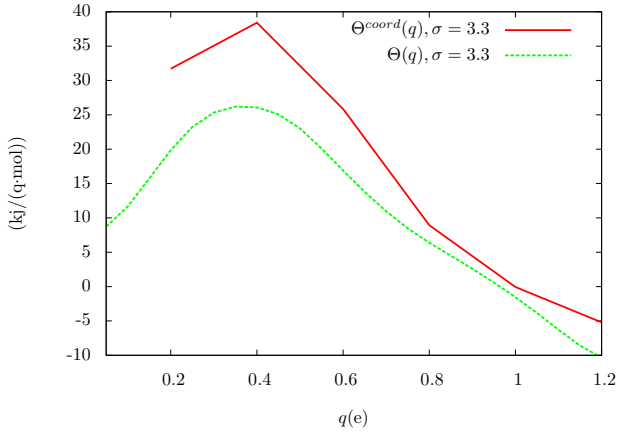

(b)

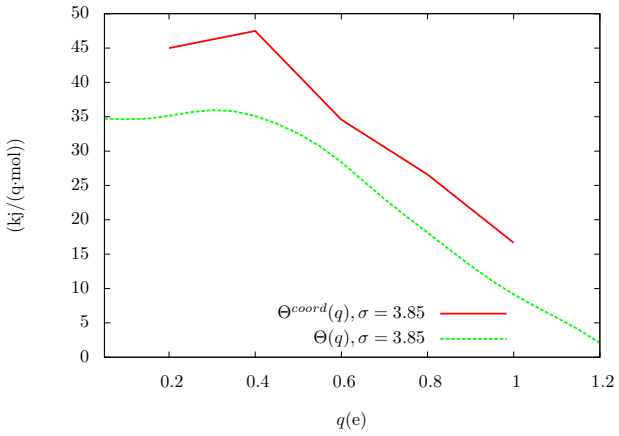

(c)

Figure 3.15: The quantities Θ and Θ^{coord} defined in the text for all three cavity sizes studied above. These quantities provide an estimate of the energetic preference per unit charge to solvate the anion at the surface over the cation.

If we assume that n_{coord} is charge symmetric then we have the approximation

$$\Delta E_{\Delta q}^{coord_1}(q) \simeq \Delta n_{coord}(q) \left[\bar{\mathcal{E}}_{coord}(z_b, q) - \bar{\mathcal{E}}_{coord}(z_b, -q)\right] \tag{3.35}$$

and

$$\Delta E_{\Delta q}^{coord_2}(q) \simeq n_{coord}(z_i, q) \left[\Delta\bar{\mathcal{E}}_{coord}(q) - \Delta\bar{\mathcal{E}}_{coord}(-q)\right]. \tag{3.36}$$

Recall that when these quantities are positive that means the anion is favored at the surface. Since $\Delta n_{coord}(q)$ is negative, the sign of equation 3.35 is determined by the quantity in brackets. If $\bar{\mathcal{E}}_{coord}(z_b, q)$ exceeds $\bar{\mathcal{E}}_{coord}(z_b, -q)$, then the cation is favored at the surface, which agrees with our intuition that if the water molecules are in an energetically more favorable state around an ion then it is more difficult to partially remove that ion from solution. Since n_{coord} is strictly positive, the sign of equation 3.36 is also determined by the quantity in brackets. When this quantity is positive it implies that the anion is favored at the surface because of the way that the interactions of water molecules in the solvation shell change when they are at the surface as opposed to in bulk. This quantity makes explicit reference to properties of the surface, but it still only measures relatively local properties. If there is some relatively long range effect associated with orientations of molecules at the surface, it may show up weakly here but this term will not capture all of that effect. To facilitate easy comparison with figure 3.15, we will look at the quantities $\Theta^{coord_1}(q)$ and $\Theta^{coord_2}(q)$ defined by

$$\Theta^{coord_1}(q) = \frac{\Delta E_{\Delta q}^{coord_1}(q)}{2q} \tag{3.37}$$

and

$$\Theta^{coord_2}(q) = \frac{\Delta E_{\Delta q}^{coord_2}(q)}{2q} \tag{3.38}$$

Figure 3.16 shows these two components of $\Theta^{coord}(q)$, which behaves in qualitatively the same way for all three cavity sizes. It starts large and positive and then is monotonically decreasing over the entire charge range, eventually becoming negative. The fact that this is large and positive for low values of q is just an indicator that the water molecules around an uncharged cavity in bulk water prefer a cation to an anion, it has nothing to do with the charge distribution of the interface. As the cavity becomes more charged the water molecules rearrange in such a way that water molecules around an anion are in a more favorable state.

The second set of curves show more dramatic differences between the three cavity sizes. For the smallest cavity size $\Theta^{coord_2}(q)$ starts out small and negative and grows to be very large and positive before decaying again. This maximum is a sign that the way water molecules rearrange in the solvation shell of the anion when you bring it to the surface is more favorable than the way that water molecules rearrange in the solvation shell of the cation when you

bring it to the surface. The 3.3 $\mathring{A}$ cavity shows similar but less pronounced behavior and for the largest ion this effect is very weak.

A large value of $\Theta^{coord_2}(q)$ can be loosely interpreted as meaning that the ion forms stronger bonds with water molecules when it's at the interface than when it's in bulk, and that this effect is stronger for the anion than it is for the cation. To illustrate this effect we have measured $\bar{u}_{is}(x, h, z)$ for a variety of ion parameters. This quantity was defined in chapter 2 and it measures the average interaction between an ion and a water molecule as a function of the spatial coordinates x (the perpendicular distance from the ion), and h the vertical distance from the surface. In figure 2.9 we showed plots of this for an anion in bulk and an anion at the surface. If we shift both of these maps into the reference frame of the ion then we can compare the two and get a sense for how much stronger (or weaker) ion-water interactions are when the ion is at the surface. We define this quantity as

$$\Delta\bar{u}_{is}(x, h) = \bar{u}_{is}(x, h, z_i) - \bar{u}_{is}(x, h, z_b). \tag{3.39}$$

Figure 3.17 shows these sets of maps for the 2.4 $\mathring{A}$ ion with charges of ± 0.3. The anion is shown in figure a and the cation is shown in figure b. There are deep minima around the anion meaning that the ion-solvent bonds are much stronger when the anion is at the interface. The cation has similar minima around it but they are much shallower. This discrepancy between the anion and the cation agrees with the fact that $\Delta E_{\Delta q}^{coord_2}$ has a maximum at this value of q. Figure 3.18 shows the same thing for the 3.3 $\mathring{A}$ ion with charges of ± 1.2. This is a case where $\Delta E_{\Delta q}^{coord_2}$ is smaller, and we find that the asymmetry between the anion and the cation is less pronounced here.

The behavior depicted in figure 3.17 implies that the solvation shell of the anion is slightly more susceptible than the solvation shell of the cation when Θ^{coord_2} is large. Somehow the water molecules around the ion can rearrange in slightly more dramatic ways to form much stronger bonds with the ion when it is at the surface. This greater susceptibility of the anion solvation shell is correlated with certain signatures of fluctuations of the solvation shell when the ion is in bulk. The simplest measure of fluctuations is simply the variance of the electrostatic potential, $\langle(\delta\phi)^2\rangle(q)$, in the center of a cavity in bulk. The linear response analysis in equation 3.9 assumes that these fluctuations don't depend on charge but there is in fact strong dependence on q. In figure 3.19 we show this quantity for all three cavity sizes and over the entire charge range studied above. A common feature to all three cavity sizes is the increase in fluctuations when the cavity acquires a negative charge (similar features have been seen in many studies of ion solvation thermodynamics in bulk, see [26, 25, 16, 51]). This feature is most dramatic for the smallest cavity, for the which the value of $\langle(\delta\phi)^2\rangle(q)$ at its maximum is nearly double its value in bulk. We have superimposed $\Theta^{coord_2}(-q)$ on these figures to show that the maxima in $\Theta^{coord_2}(-q)$ roughy correspond to the maxima in $\langle(\delta\phi)^2\rangle(q)$. We don't mean to imply a direct connection between these two quantities, but it seems reasonable to suppose that the effective response of the solvation shell which is measured by $\Theta^{coord_2}(q)$ is connected to fluctuations in the solvation shell.

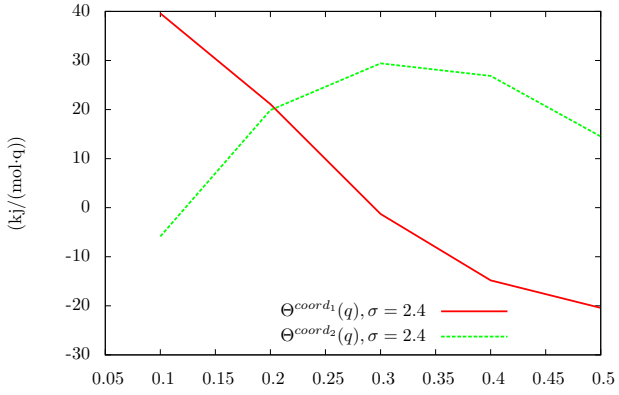

(a)

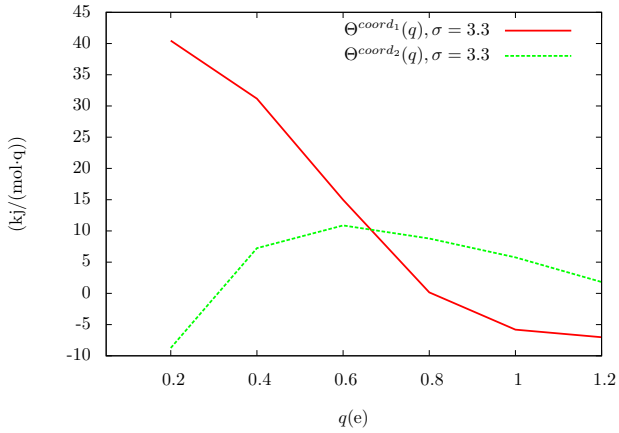

(b)

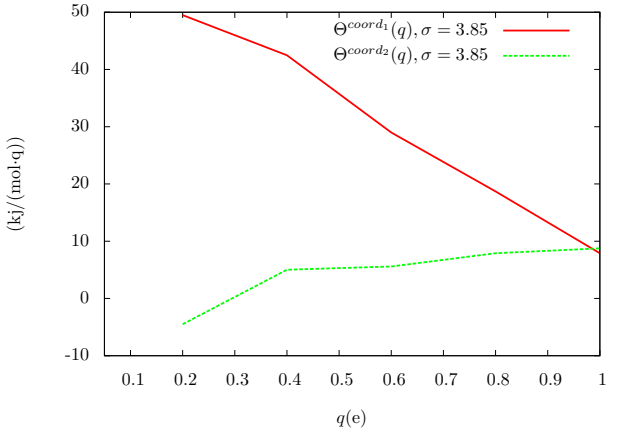

(c)

Figure 3.16: The quantities Θ^{coord_1}, and Θ^{coord_2} discussed in the text.

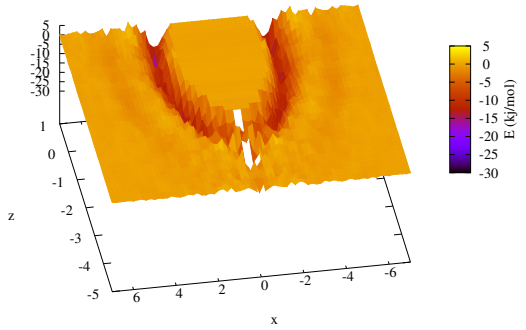

(a)

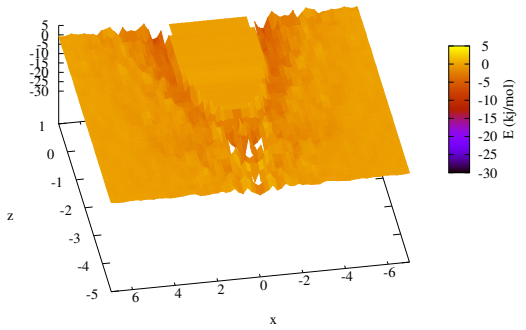

(b)

Figure 3.17: $\Delta\bar{u}_{is}(x,h)$ for an anion (a) and a cation (b) with hard core radii of 2.4$\mathring{A}$ and charges of $\pm$ 0.3. This quantity is a measure of how much stronger ion-solvent bonds are when the ion is at the surface. In this case this effect is much stronger for the anion, and this corresponds to a large value of $\Delta E^{coord_2}_{\Delta q}$.

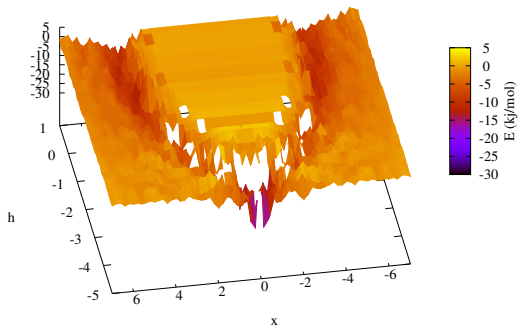

(a)

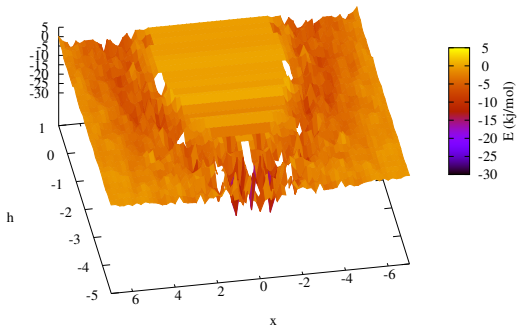

(b)

Figure 3.18: $\Delta\bar{u}_{is}(x,h)$ for an anion (a) and a cation (b) with hard core radii of 3.3$\mathring{A}$ and charges of $\pm$ 1.0. The asymmetry between the anion and the cation is less pronounced here than it is for the smaller ion above.

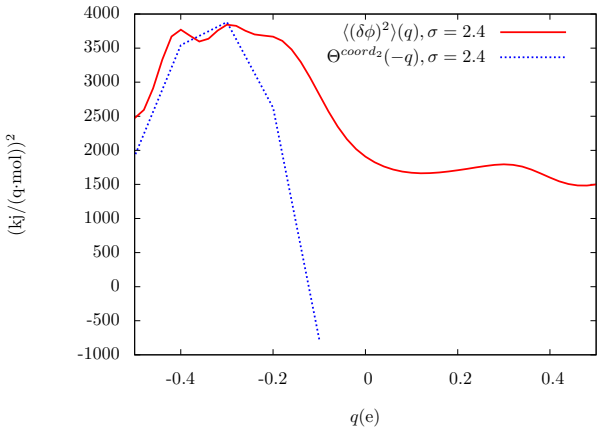

(a)

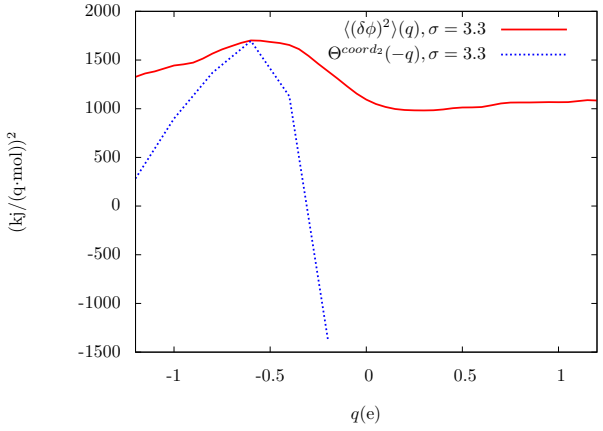

(b)

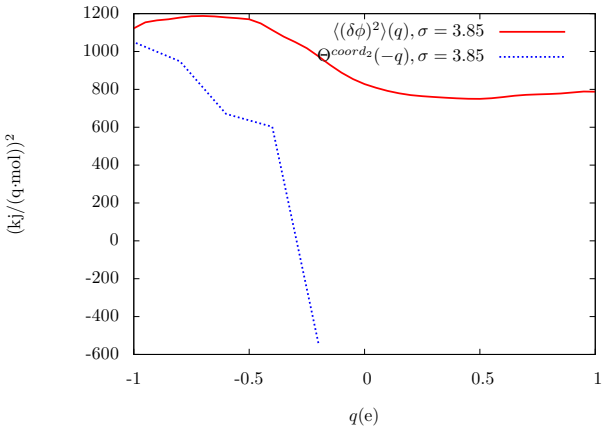

(c)

Figure 3.19: The variance of the electrostatic potential for three different cavity sizes in bulk. We have superimposed $\Theta^{coord_2}(-q)$ to make the qualitative point that the maxima in this quantity loosely correspond to maxima in the fluctuations of the electrostatic potential.

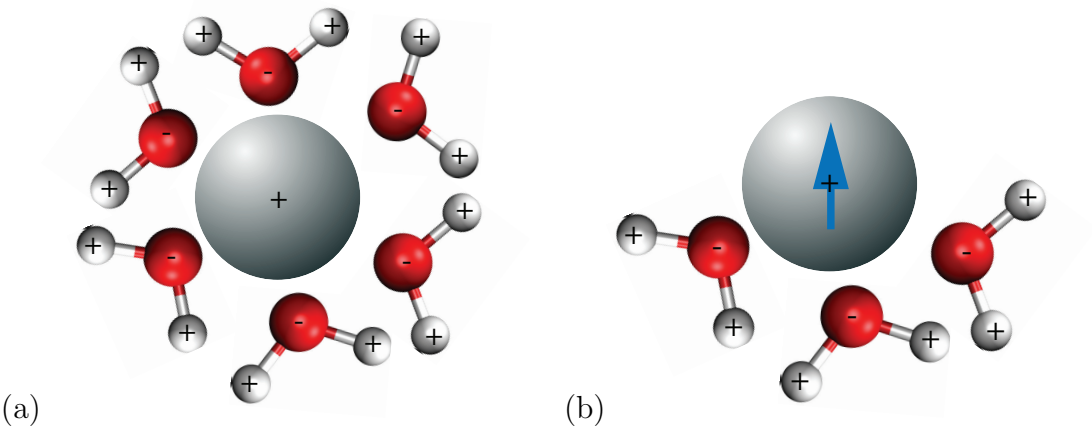

(a) (b)

Figure 3.20: An illustration of a polarizable cation in bulk (a) and at the surface(b). In bulk there is on average no electric field at the center of the ion. At the surface, the partially coordinated ion has a net electric field at the center due to the orientational bias in the surrounding water molecules. The corresponding induced dipole at the center of the ion interacts favorably with the electric field.

3.6 Charge asymmetry in polarizability

In this section we ask whether there are any charge asymmetric effects associated with the polarizability of the ion. Polarizability, both of the ion and of the water model itself, is well studied as a force that can stabilize ions at interfaces [62, 2]. The general reasons why a polarizable ion might be more stable at an interface are illustrated in figure 3.20. At the center of an ion in bulk, the average electric field is necessarily 0 because of the symmetry. An ion at the surface is only partially coordinated, and the neighboring water molecules have orientational bias, so there can be a non zero electric field in the z-direction and the induced dipole on the ion interacts favorably with this field. In the context of dielectric continuum theory, the induced dipole interacts favorable with the image charge of the ion. A full DCT treatment would include the fact that the induced dipole interacts unfavorably with its own image and this is a counterbalancing effect, but the net effect of polarizability is favorable for an ion at the surface. For a full discussion see [41].

Based on the work in this chapter there are many reasons to suspect that there might be a charge asymmetric effect associated with polarizability of the ion. The picture described in 3.20 considers only the orientational bias on water molecules coordinating the ion. However, the intrinsic orientational bias on water molecules at the surface may also produce an electric field in the center of the cavity. Furthermore, the interaction of an induced dipole with the solvent depends on the fluctuations of the electric field at the center of a cavity (not just the mean), and there may be large charge asymmetries in these electric field fluctuations as there were in electrostatic potential fluctuations.

We will address some of these question by measuring the probability distribution of the electric field in the center of a charged cavity with charge q, $P_q(\vec{E};z)$. Knowledge of this probability distribution allows us to determine the free energy change associated with giving a non polarizable ion a finite polarizability. We will demonstrate this for the specific case of a harmonic model for polarizability, but the arguments can be generalized to other models. The polarizability α determines the cost associated with forming a transient dipole, $\vec{d}$ at the center of the ion, which then interacts with the electric field of the solvent at the center of the ion, $\vec{E}(r^N)$. The potential energy associated with such a model is

$$U_{pol}(\vec{d},r^N) = \frac{\mid \vec{d} \mid^2}{2\alpha} - \vec{d}\cdot\vec{E}(r^N) \tag{3.40}$$

The remaining component of the potential energy is associated with Van der Waals and fixed charge interactions, and we denote this by U_{VdW+fc}. Given these potential energies we can write the partition function as

$$Z(z,q,\alpha) \propto \int \mathrm{d}r^N \int \mathrm{d}\vec{d} \exp[-\beta U_{VdW+fc}(r^N) - \beta U_{pol}(\vec{d},r^N)]. \tag{3.41}$$

Because $U_{pol}(\vec{d},r^N)$ is quadratic we can perform the integral over $\vec{d}$ analytically, which is equivalent to minimizing $U_{pol}(\vec{d},r^N)$ with respect to $\vec{d}$. This gives us

$$Z(z,q,\alpha) \propto \int \mathrm{d}r^N \exp[-\beta U_{VdW+fc}(r^N) + \frac{\beta\alpha}{2} \mid \vec{E}(r^N) \mid^2]. \tag{3.42}$$

In a familiar operation we can multiply by $\delta(\vec{E}' - \vec{E}(r^N))$ and integrate over $\vec{E}'$ to obtain

$$Z(z,q,\alpha) \propto \int \mathrm{d}\vec{E}' \exp[\frac{\beta\alpha}{2} \mid \vec{E}' \mid^2] \int \mathrm{d}r^N \delta(\vec{E}' - \vec{E}(r^N)) \exp[-\beta U_{VdW+fc}(r^N)], \tag{3.43}$$

Which is equivalent to

$$\int \mathrm{d}\vec{E}' P_q(\vec{E}';z) \exp[\frac{\beta\alpha}{2} \mid \vec{E}' \mid^2] Z_{VdW+fc}(z,q). \tag{3.44}$$

This allows us to define a polarization free energy as

$$F^{pol}(z,q,\alpha) = -k_{\mathrm{B}}T \ln \int \mathrm{d}\vec{E}' P_q(\vec{E}';z) \exp[-\frac{\beta\alpha}{2} \mid \vec{E}' \mid^2]. \tag{3.45}$$

Because we are interested in the forces that stabilize ions at surface, a naturally relevant quantity is

$$\Delta F^{pol}(q,\alpha) = F^{pol}(0,q,\alpha) - F^{pol}(-10,q,\alpha), \tag{3.46}$$

which dictates how much nonzero α stabilizes an ion at the surface. If the z component of the electric field acquires a nonzero mean for an ion at the surface, $\Delta F^{pol}(q)$ will likely be negative. For small values of the polarizability this decrease is given by

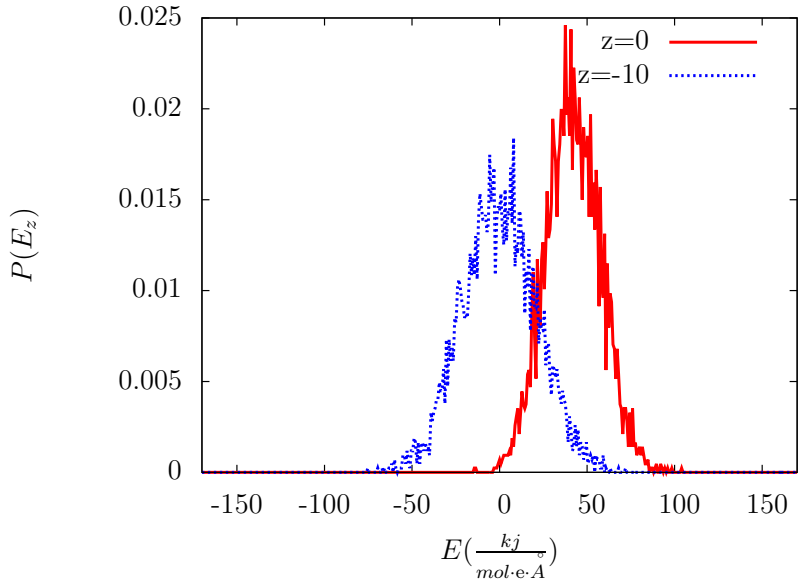

Figure 3.21: Probability distributions of the z component of the electric field at the center of an ion in bulk and at the interface. The ion considered here has a hard core radius of 3.3 $\mathring{A}$ and a charge of -0.4 e. The ion at the surface clearly has a nonzero mean, and it also has a slightly less broad probability distribution than the ion in bulk.

$$\Delta F^{pol}(q,\alpha) \simeq -\alpha \langle E_z \rangle_{q,0}^2, \tag{3.47}$$

where $\langle E_z \rangle_{q,0}$ is the mean electric field in the z direction for an ion of charge q and height 0. It has been shown that this linear relationship breaks down for modest values of α and that the simple linear scaling actually underestimates the decrease in F^{pol} [41].

The probability distributions $P_q(\vec{E}';z)$ computed in this work were computed from straight forward sampling and thus we do not have very accurate estimates of the decay in the wings. We can however accurately estimate shifts in the mean and variance when the ion moves from bulk to the surface. Figure 3.21 shows the probability distributions of the z component of the electric field for an ion with a charge of -0.4 e both in bulk and at the interface. The mean is substantially nonzero at the surface and the distribution is also noticeably narrower. Given that we have imperfect approximations to the full probability distributions we will focus attention on small values of α. In figure 3.22 we show the measured values $\Delta F^{pol}(q,\alpha)$ for a range of cavity sizes. We have used a value of $\alpha = 0.1\mathring{A}^3$, which is very small compared to typical polarizabilities used to model real ions, but the general trends in figure 3.22 are independent of the exact value of α. When $\Delta F^{pol}(q,\alpha)$ is negative this implies that a finite polarizability stabilizes an ion at the interface. In figure 3.22 ΔF^{pol} is negative for nearly all values of q and all three ion sizes, but there is dramatic charge asymmetry. In general the anions are far more stabilized at the interface by polarizability than the equivalent cation is.

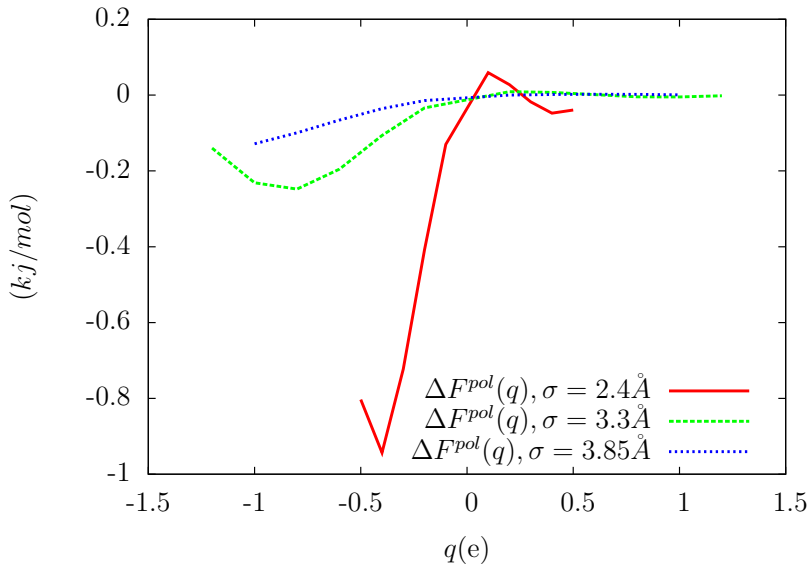

Figure 3.22: $\Delta F^{pol}(q)$ showing how polarizability stabilizes ions at the interface, for three different cavity sizes. There is very dramatic charge asymmetry for all three cavity sizes.

The smaller two ions also have clear minima in q for which polarizability has an optimum stabilizing effect.

This is a low polarizability regime, in which the approximation in equation 3.47 is fairly good and the behavior is dominated by the nonzero values of $\alpha\langle E_z\rangle_{q,0}$. In figure 3.23 we show $\alpha\langle E_z\rangle_{q,0}$ for the three different ion sizes studied above. The anions and the cations induce electric fields which have the opposite sign (which is not surprising), but very different magnitudes indicating that it is much easier to induce a nonzero electric field at the center of an anion than a cation. Furthermore the smaller two cations show the same sweet spot seen in $\Delta F^{pol}(q)$, where there is a particular value of q for which it is easiest to induce a nonzero $\langle E_z\rangle_{q,0}$. This behavior is mirrored by the variance $\langle(\delta E_z)^2\rangle_{q,0}$ which shows maxima for moderate negative charges before decaying again (see figure 3.24). This behavior bears some qualitative similarities to the behavior seen figure 3.19, where we saw maxima in the fluctuations of the electrostatic potential for intermediate negative charges.

3.7 Charge asymmetry near other surfaces

To end this chapter we briefly address the question of what happens when the ion is adsorbing not to an air-water interface but to a surface that has some weak attraction for water molecules. The surface we study here is the same as the attractive surface described in chapter 2 (see equation 2.46), except we are using a slightly stronger attraction. The surface interacts with the water molecules only. In chapter 2 we saw that there were substantial

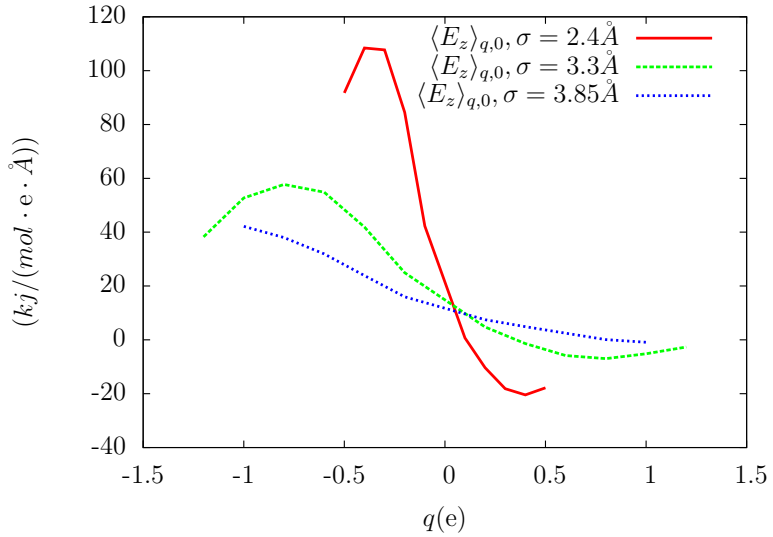

Figure 3.23: $\langle E_z \rangle_{q,0}$ for all three cavity sizes, showing that the magnitude of induced electric field for an ion at the surface is in general much larger for the anions then it is for the cations.

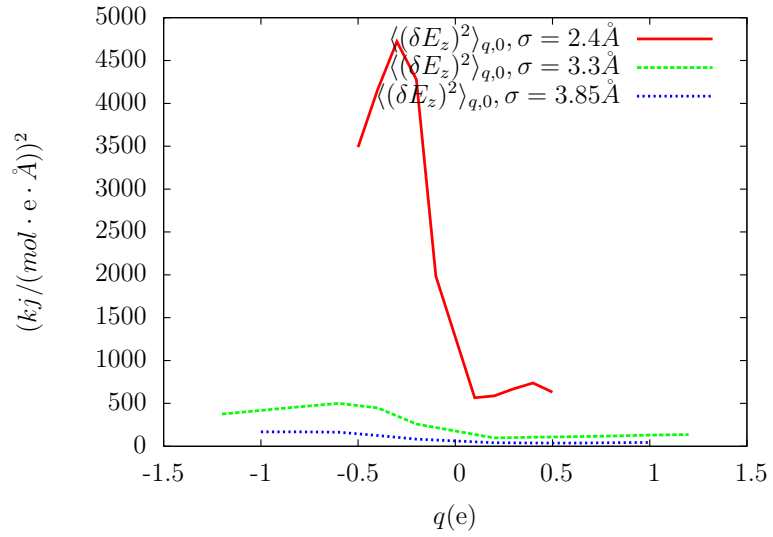

Figure 3.24: $\langle (\delta E_z)^2 \rangle_{q,0}$ for all three cavity sizes in bulk, showing that fluctuations of the electric field are in general larger in the interior of an anion than a cation, and have a maximum at intermediate charge.

changes in the entropy of adsorption for a fractionally charged iodide to such a surface. In this chapter we will investigate a broader charge range and look for any dramatic charge asymmetry or ion specificity in general. Based on the discussion in chapter 2 we expect there to be some effect associated with the absence of capillary waves near the attractive surface but it is not at all clear how such an effect might depend on charge.

To address these questions we compute $\Delta F^{att}(q)$, which is exactly the same quantity defined in equation 3.13 except the surface is the attractive wall. The ion studied here has a hard core radius of 3.3 $\mathring{A}$ In figure 3.25a we show this quantity along with the same thing for a liquid vapor interface for reference. Taking the difference between these two quantities, as we do in figure b, exposes the fact that there are pronounced peaks at intermediate values of the charge. These peaks mean that at those values of the charge the ion much prefers adsorbing to the attractive wall than the liquid-vapor interface. These peaks could have more than one interpretation, but it's likely they are charges at which the ion has the maximum effect on capillary waves as described in the previous chapter. For very small charges, the interface prefers to bend around the ion, effectively expelling the ion from solution. The interface in this case very much resembles a liquid vapor interface, and has the associated large fluctuations. For very high charges, the interface prefers to bend in the other direction, effectively keeping the ion totally solvated. In this case the interface again has large fluctuations. It's only for intermediate values of the charge for which the fluctuations are maximally suppressed and there is a large entropic penalty for putting the ion at the surface. It is this suppression of fluctuations which is effectively removed by replacing the air water interface with an attractive wall, and therefore the intermediate charges have the largest free energy differences when the attractive wall is present. These maxima at intermediate charges are reminiscent of behavior seen in a schematic lattice gas model for solute adsorption. In the lattice gas model the solute interacts with occupied solvent cells with an attractive energy ϵ which is analogous to charge. In these models it was seen that surface adsorbing solutes have entropic minima when the solute at the surface, but the depth of this minimum is greatest for a intermediate values of ϵ [60].

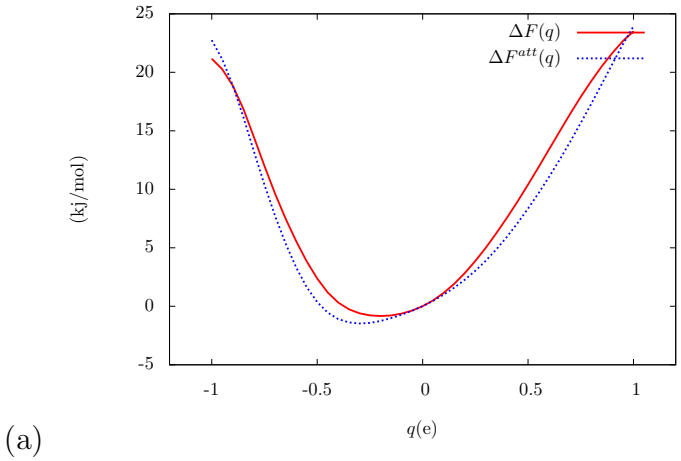

(a)

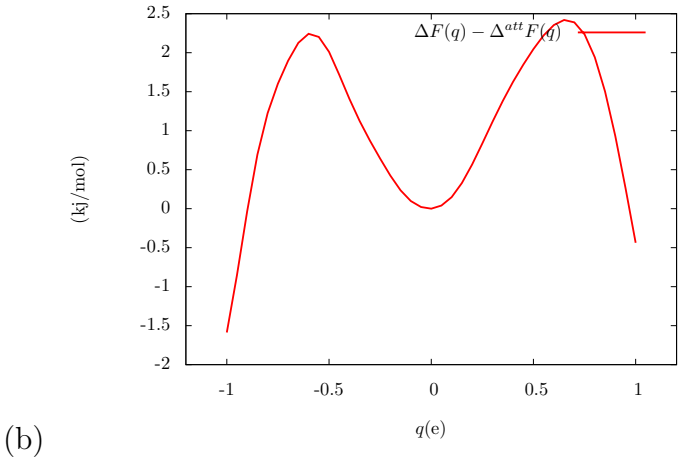

(b)

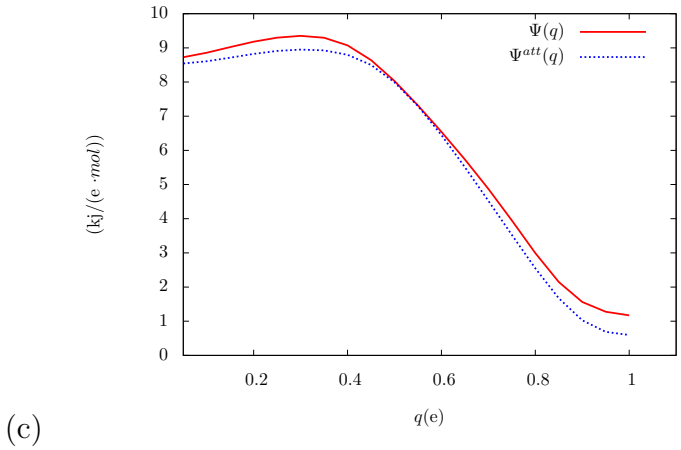

(c)

Figure 3.25: Details of ion adsorption to wall with a weak attraction for water molecules. In figure a, we show the quantities $\Delta F^{att}(q)$ and $\Delta F(q)$ measuring the difference between charging free energies at the surface and in bulk. In figure b we take the difference between these two quantities to emphasize that there are pronounced peaks at intermediate charges. Positive values of this quantity mean that an ion would prefer to adsorb to the attractive wall than a plain liquid vapor interface. In figure c, we show $\psi(q)$ and $\psi^{att}(q)$ which shows that the attractive wall does not change the charge asymmetry in any dramatic way.

Chapter 4

The impact of solvent polarizability on inter-ion interactions

4.1 Preliminaries

Molecular dynamics and Monte Carlo simulations of water and other liquid solvents are typically conducted using nonpolarizable force fields. In these models the interactions between two molecules consist of interactions between a small number of fixed charge sites and fixed Van der Waals sites. The SPC/E water model and the Stockmayer solvent studied in previous chapters are examples of such models. These models must capture the effects of electronic polarizability of molecules implicitly. Polarizable force fields, by contrast, endeavor to capture the fluctuating molecular charge distribution explicitly [52]. This comes at a significant computational cost, and for this reason, it is worth investigating in detail how well non polarizable models can capture the effects of polarizability implicitly. Leontyev and Struchebrukhov have argued that one can implicitly capture the effects of polarizability by scaling the charge of ions by a factor of $1/\sqrt{\epsilon_{el}}$ where ϵ_{el} is the high frequency dielectric constant of the solution [34]. The argument put forth is based on an assumption of spatial homogeneity of the electronic degrees of freedom, and it is not clear how these arguments break down in the presence of significant inhomogeneities, for example, an interface or a protein. In this chapter we quantitatively evaluate this approximation using a model of polarizable water.

4.2 Molecular Dynamics Electronic Continuum Model

In several recent papers Leontyev and Stuchebrukhov have introduced the molecular dynamics electronic continuum model (MDEC), where dielectric continuum theory is used to treat electronic polarizability, and standard nonpolarizable force fields are used to capture nuclear motion [34]. The nuclear motion is the slower time scale motion, and it is usually

associated with the low frequency dielectric constant ϵ. This models bears a connection to the way the most sophisticated polarizable models currently treat polarizability, and we briefly review this connection here. For a system of point charges with harmonically bound inducible dipoles the energy is given by

$$U = \frac{1}{2}\sum_{i\neq j}^{N}\frac{q_i q_j}{r_{ij}} + \frac{1}{2}\sum_{i,j=1}^{N}\vec{d}_i K(r_i, r_j)\vec{d}_j - \sum_{i}^{N}\vec{E}_o(r_i)\vec{d}_i. \tag{4.1}$$

$\vec{E}_o(r_i)$ is the value of the electric field at r_i due to all the fixed charges. To keep the discussion and the notation simple, we are ignoring distinctions between separate molecules, but to be precise we should include only contributions to the electric field from the fixed charges on other molecules. $K(r_i, r_j)$ is the coupling matrix for dipole interactions. its diagonal elements are given by $1/\alpha$, where α is a molecular or atomic polarizability and its off diagonal elements are given by:

$$K(r_i, r_j) = \nabla_i \nabla_j \frac{1}{|r_i - r_j|}. \tag{4.2}$$

In principle a molecular dynamics simulation in which the electrostatics were represented by equation 1 could proceed by updating both the $\vec{d}_i$ and the r_i simultaneously. However the motion of the induced dipoles is intended to capture electronic motion, which has a much faster time scale than the nuclear motion represented by the r_i. This means that for a given value of the nuclear positions you expect the dipoles to sample all of their positions with a Boltzmann weight, which for a harmonic restoring force is exactly captured by finding the minimum of equation 1 with respect to $\vec{d}_i$. This means we must find the values of $\vec{d}_i$ that satisfy the following equations:

$$\frac{\vec{d}_i}{\alpha} + \sum_{i\neq j}^{N} K(r_i, r_j)\vec{d}_j - \vec{E}_o(r_i) = 0. \tag{4.3}$$

Minimizing this set of N-coupled equations after each MD time step to determine the polarization is what makes simulations of polarizable models costly. In the context of dielectric continuum theory, there is a simple relationship between the polarization density and the external field. The MDEC model consists of assuming that the fixed charges constitute an external field and the inducible dipoles form a uniform dielectric continuum with dielectric constant ϵ_{el}. In this case the polarization density is:

$$\vec{P}(r) = \frac{1}{4\pi}\frac{\epsilon_{el} - 1}{\epsilon_{el}}\vec{E}_o(r) \tag{4.4}$$

Given a typically molecular volume v, we can relate the polarization density to the induced dipole:

$$\vec{d}(r) = \vec{P}(r)v. \tag{4.5}$$

Using this equation implies that the electrostatic energy can be rewritten as, see [34] for details:

$$U = \frac{1}{2}\sum_{i\neq j}^{N}\frac{q_i q_j}{\epsilon_{el} r_{ij}} - \sum_{i=1}^{N}(1-\frac{1}{\epsilon_{el}})\frac{q_i^2}{2R_i} \tag{4.6}$$

The second term in this equation is the familiar born solvation energy, and the first term is standard screened electrostatics. This equation says that the effect of the polarizability is two fold. First, each fixed charge has an effective born solvation self energy with the inducible dipoles. Second, the interactions between fixed charges are screened by a factor ϵ_{el}. As Leontyev and Struchebrukhov point out, this type of reasoning already underlies parameter choices in existing empirical potentials of water such as TIP3P and SPC/E, which have an effective molecular dipole of 2.3D. Gas phase estimates of the water molecule dipole are about 3.0D, and if we scale this by $\frac{1}{\sqrt{\epsilon_{el}}}$, we get a value very close to 2.3D. The original paper on SPC/E water even explicitly acknowledges that the parameter modifications are intended to correct for polarization [5]. Simulations of these models with ions, however, always use the full value of the charge, and may therefore overestimate the interactions involving these ions. The simplest approach is to simply scale the magnitudes of these charges according to equation 4.6. It is by no means clear how good an approximation this is in the presence of large inhomogeneities. The MDEC assumes that all the fixed charges are embedded in a uniform dielectric continuum composed of the electronic degrees of freedom. But the interior of an ion is likely to have a significantly different ϵ_{el} then the solvent. Furthermore, there is significant interest in how ions behave at interfaces between air and water, and in these cases, the assumption of a uniform dielectric is obviously false.

4.3 Scrutinizing the MDEC model in bulk

We will first examine the MDEC model for the interaction between two ions in bulk. From the perspective of equation 4.6 the interaction between two ions is

$$\bar{U}(r) = \frac{q_i q_j}{\epsilon_{el} r}. \tag{4.7}$$

This is the sum of the bare coulomb interaction ($\frac{q_i q_j}{r}$) and the interaction of the ions with the polarization field $\bar{U}^{pol}$ which is given by

$$\bar{U}^{pol}(r) = -\frac{\epsilon_{el}-1}{\epsilon_{el}}\frac{q_i q_j}{r}. \tag{4.8}$$

In the sort of polarizable atomistic system that the MDEC is intended to mimic, the actual interaction between the ions and the polarization field (U^{pol}) depends on all the values of $\vec{d_k}$, which in turn depend on the fixed charge configuration according to equation 4.3. U^{pol} takes the form

$$U^{pol} = \sum_k \frac{q_i \vec{d_k} \cdot \hat{r}_{ik}}{r_{ik}^2} + \sum_k \frac{q_j \vec{d_k} \cdot \hat{r}_{jk}}{r_{jk}^2} \tag{4.9}$$

where $\hat{r}_{ik}$ is the unit normal vector connecting i and k. This quantity is nonzero even when the ions are widely separated because it includes the interaction between the individual ions and the polarization field (which $\bar{U}^{pol}(r)$ does not). We are only interested in how this quantity scales with r, the distance between the two ions, so we will look at

$$\Delta U^{pol} = U^{pol}(r) - U^{pol}(\infty). \tag{4.10}$$

To the extent that the uniform dielectric approximation is accurate, an average of $\Delta U^{pol}(r)$ should agree reasonably well with $\bar{U}^{pol}(r)$. We will compute this average by sampling many configurations from a non polarizable model of water with the ions constrained to be a certain distance r from one another. For each nuclear configuration we will solve for the $\vec{d_k}$ using equation 4.3. This equation can be solved using conjugate gradient minimization [53, 54]. We will adopt a simple model for water polarizability in which there is just one induced dipole per water molecule, located on the oxygen atom, for which the polarizability α is 1.5 $\mathring{A}^3$. This is nearly identical to the polarizability used in the Dang-Chang polarizable water model [12], but we have looked at a wider range of polarizabilities and found that it does not change the qualitative picture described here. In figure 4.1 we show $\langle \Delta U^{pol} \rangle(r)$ for two pairs of oppositely charged ions in bulk water. Each pair of ions carries charges of ± 0.75e but one pair has a Lennard-Jones diameter of 2.5 $\mathring{A}$ and the other has a Lennard-Jones diameter of 4.7 $\mathring{A}$. We have measured this polarization energy all the way down to an inter-ion separation of zero (in which case the ions are obviously overlapping). We've also plotted the dielectric continuum approximation from equation 4.8. The value of ϵ_{el} of 2.5 was determined by fitting to the $\langle \Delta U^{pol} \rangle(r)$ curves for large values of r. For both cavity sizes the dielectric continuum approximation is qualitatively very good all the way up to the point where the cavities start to overlap. However, for the larger of two ions there is clear quantitative disagreement when the two separation between the two ions slightly exceed the overlap separation.

4.4 Scrutinizing the MDEC model at the surface

The results of the last section indicate that the simple dielectric continuum theory is a fairly good way of capturing the interactions between ions in bulk as long as those ions are not overlapping. In this section we ask how this breaks down when those ions are at the interface. We have performed a set of calculations which are exactly analogous to those described in the last section, except the ions are constrained to be a particular distance above the Gibbs dividing surface. This constraint applies to each ion individually, so they move in a plane parallel to the Gibbs Dividing surface. The results of this analysis are shown in figure 4.2 for the larger pair of ions at 0, 4 and 8 $\mathring{A}$ above the Gibbs dividing surface. The

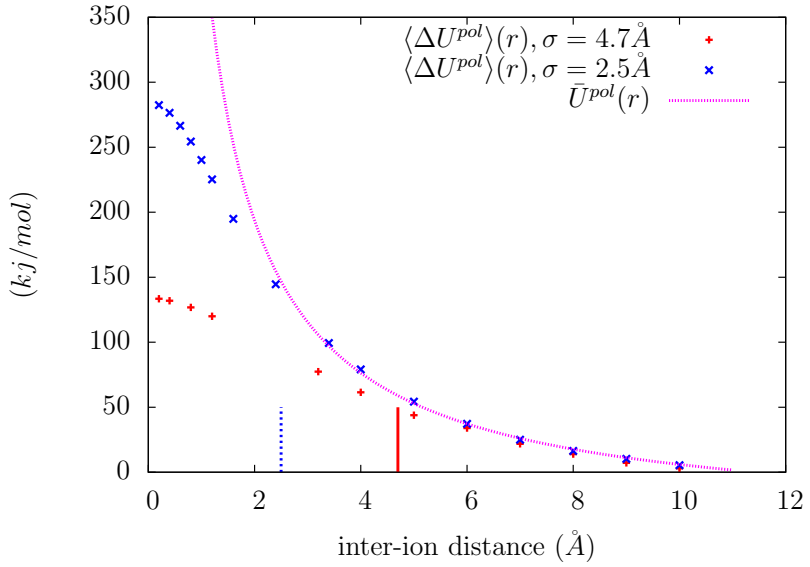

Figure 4.1: Average polarization energies which measure the interaction between the two fixed charges on the ions and the induced dipoles of the solvent molecules for two different pairs of ions. The different pairs of ions are distinguished by their different Lennard-Jones diameters σ, indicated in the legend. The vertical lines show the separation at which the two ions are in contact. The ions have charges of ± 0.75e. Also shown is the dielectric continuum approximation to this quantity ($\bar{U}^{pol}(r)$).

dielectric continuum approximation and the value of $\langle \Delta U^{pol} \rangle(r)$ for a pair of ions in bulk are shown again for reference. The DCT approximation has the same quantitative flaws seen in the previous plot, but it is qualitatively a surprisingly good description, even for the pair of ions 8 $\mathring{A}$ above the surface. The success of this approximation is connected to the fact that the interface deforms itself substantially in order to keep the ions partially solvated. Only when the ions are 8 $\mathring{A}$ above the Gibbs dividing surface, and separated by less than about 3 $\mathring{A}$ does the $\langle \Delta U^{pol} \rangle(r)$ become qualitatively very flat, indicating that the ions are no longer partially solvated by a distorted interface.

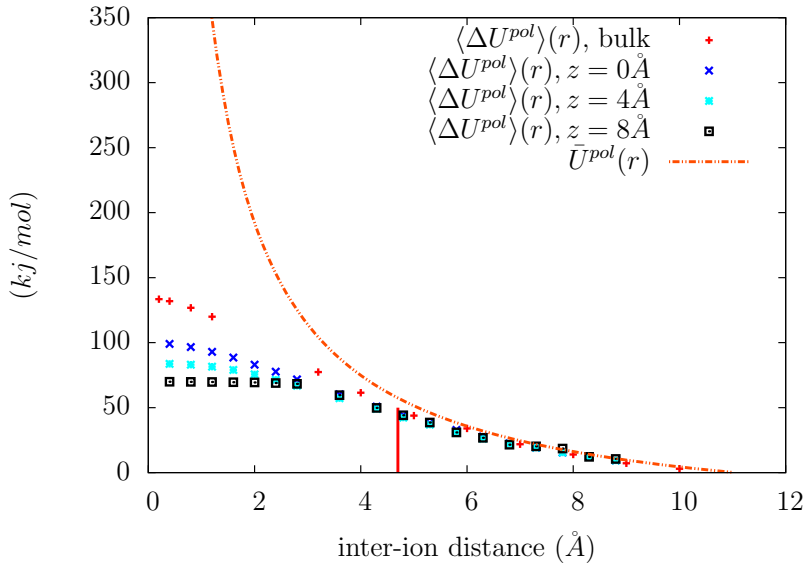

Figure 4.2: Average polarization energies for two ions separated by the distance on the x-axis. This measures the same quantity as the figure above, except in this case the ions were constrained to be a certain distance above the Gibbs dividing surface. We show the result for the two ions in bulk, as well as the dielectric continuum approximation for reference ($\bar{U}^{pol}(r)$).

Chapter 5

Dielectric continuum theory for interfaces

5.1 Preliminaries

In chapter 2 we discussed how it is natural to think of solvation thermodynamics in terms of two distinct components. The cavity formation free energy is, regardless of length scale a force that draws ions to air-water interfaces and the charging free energy tends to repel ions from those interfaces. Because of the approximately gaussian nature of the fluctuations of the electrostatic potential, dielectric continuum theory is considered a good reference theory for computing the charging free energy. The most naive implementation of dielectric continuum theory treats the ion as a point charge, and predicts divergent forces acting on the ion as it approaches the surface. This divergence is clearly not physical and it is a sign that we need to treat the finite size of the ion explicitly in order to get sensible predictions from dielectric continuum theory. Another element missing from the point charge description presented in chapter 1 is the flexibility of the interface. As illustrated in chapters 2 and 3, this flexibility has important consequences and should not be left out of a predictive theory.

In this chapter we will describe ways to include some of these missing ingredients in dielectric continuum theory. The theory presented here is based on the reformulation of macroscopic dielectric continuum theory in terms of microscopic gaussian fluctuations due to Song and Chandler [58, 57]. The advantage of formulating DCT this way is that inhomogeneities like the solute can be treated as constraints on a gaussian field, which is both physically intuitive and allows us to use mathematical tools from constrained gaussian field theory [8]. In this chapter we first describe flawed attempts to handle the finite size of the ion in DCT, then we review the gaussian field theory formulation of DCT, and then we extend this formulation of DCT to a system with an extended interface.

5.2 Flawed attempts to treat the finite size of the ion in DCT

The simplest improvement to the point charge DCT described above and in chapter 1 is to account for the finite size of the ion by setting the dielectric constant in the interior of the ion to 1. Figure 5.1 is an illustration of the resulting geometry. The charge is now embedded in a cavity of radius L with a dielectric constant $\epsilon_2 = 1$, at a distance z from the boundary where the dielectric constant changes from $\epsilon_1 = 80$ to ϵ_2. The solution to Poisson's equation must now satisfy boundary conditions on the plane interface and the surface of the sphere. As we will see, these boundary conditions cannot be satisfied in any simple way. Even for this simplest realistic geometry we will require numerical techniques. There are published analytical solutions to this problem from Kharkats and Ulstrup which purport to solve this problem but in fact violate the boundary conditions of DCT [32]. This solution is frequently cited despite its flaws [40, 27]. The Kharkats and Ulstrup treatment starts from the following expression for the electrostatic energy in terms of the displacement vector:

$$W = \frac{1}{2}\int D(r)E(r)dV, \tag{5.1}$$

where the integration is over the volume not occupied by the ion and $D(r) = \epsilon E(r) = -\epsilon\nabla\phi(r)$. This expression is exact and the volume integrals can be transformed in to surface integrals by integration by parts, but it requires that you know $\phi(r)$ which is the solution to Poisson's equation. Kharkats and Ulstrup assert that $\phi(r)$ takes the form in equation 1.5, which is the solution for two uniform dielectrics separated by a boundary, with no spherical cavity:

$$\phi(r) = \frac{q}{\epsilon_1|r-z|} + \frac{\epsilon_1 - 1}{\epsilon_1 + 1}\frac{q}{\epsilon_1|r-z'|} \tag{5.2}$$

For this solution to be correct it must not only satisfy the boundary conditions on the planar surface, it must also satisfy those boundary conditions on the surface of the spherical cavity. These boundary conditions are:

$$\epsilon_1\frac{\partial\phi(r)}{\partial n}|_{sphere} = \frac{\partial\phi_i(r)}{\partial n}|_{sphere} \tag{5.3}$$

and

$$\frac{\partial\phi(r)}{\partial\rho}|_{sphere} = \frac{\partial\phi_i(r)}{\partial\rho}|_{sphere}. \tag{5.4}$$

Where $\phi_i(r)$ is the potential in the interior of the cavity and $\frac{\partial}{\partial n}$ is a surface normal derivative and $\frac{\partial}{\partial\rho}$ is a surface tangential derivative. Demonstrating that 5.2 cannot satisfy these equations requires us to choose a form for the potential inside a cavity. The natural choice is

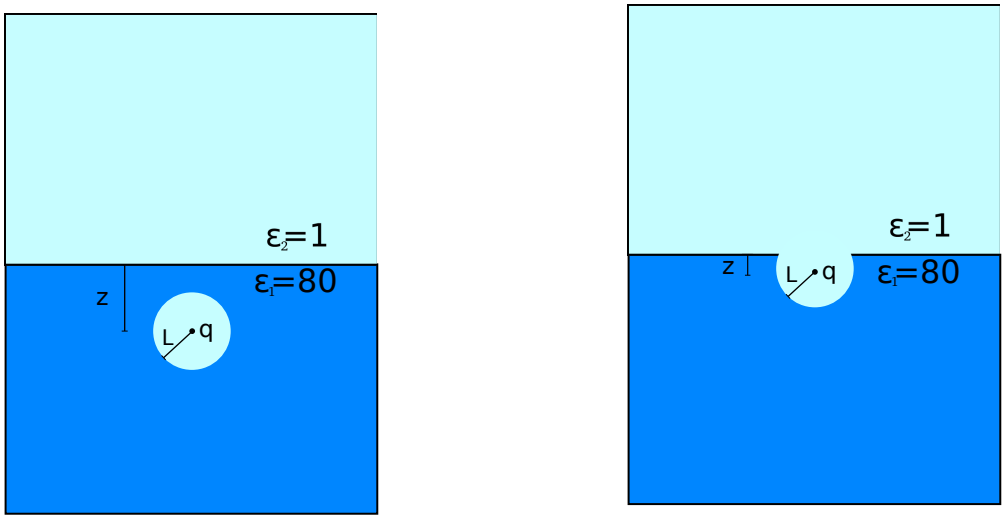

Figure 5.1: A schematic illustration of the boundary between two dielectric media when there is a volume excluding ion present. Figure a illustrates the case when the spherical cavity does not penetrate the boundary, and Figure b illustrates the spherical cavity overlapping with the boundary. In neither case is the potential described by a simple image charge.

$$\phi_i(r) = \frac{q}{|r-z|} + \frac{Aq}{|r-z'|}. \tag{5.5}$$

Plugging this into equation 5.3 would give you $A = \frac{\epsilon_1 - 1}{\epsilon_1 + 1}$ and equation 5.4 would give you $A = \frac{\epsilon_1 - 1}{\epsilon_1(\epsilon_1+1)}$, which are obviously not consistent with one another. All otther choices for ϕ_i also fail to satisfy these boundary conditions.

5.3 Microscopic model of a dielectric

In this section we describe a microscopic formulation of dielectric continuum theory in terms of a fluctuating polarization field that will allow us to recast problems like the one above. This theory was developed by Song, Chandler and Marcus as both a lattice field theory [58] and a continuum field theory [57] and the discussion in this section is based on those two papers. We present a thorough review here because it will aid the subsequent development.

For a very broad class of materials called linear dielectrics, we describe the electrostatic response of the system in the same very simple way:

$$P(r) = \chi_e \mathcal{E}(r). \tag{5.6}$$

where $P(r)$ is the polarization and $\mathcal{E}(r)$ is the electric field, which, in any real material includes contributions from both applied external fields and internal fields. χ_e is a material property called the susceptibility that for our purposes is a scalar but could be a tensor if the material does not respond isotropically. The fact that such a simple equation can be used to describe solids, liquids and gases seems surprising because the microscopic physics underlying charge redistribution seems at first glance to vary widely between different materials. The theory we describe provides some perspective on the origins of this simplicity. In the gaussian field theory we describe the microscopic charge distribution by a spatially varying, fluctuating polarization field $\vec{m}(r)$. The polarization field that we are imagining is a coarse grained polarization, it is not the instantaneous dipole of an individual molecule in a liquid for example. It is the average polarization of a region of space that constitutes a few molecular diameters. The fluctuations that determine this polarization could be very different for different materials. In liquid water, for example, the dominant effect comes from the fluctuating molecular orientations whereas in a solid metal the dominant effect may involve fluctuating electron clouds. Furthermore, the charge distribution in this region is likely to have higher order multipoles. In this theory we ignore these details and assume that there is strictly a quadratic penalty for establishing a polarization and that the polarization at separate points in space interact with one another as point dipoles. The Hamiltonian is then:

$$H = n\int dr \frac{|\vec{m}(r)|^2}{2\alpha} + \frac{n^2}{2}\int\int drdr' \vec{m}(r)\cdot\nabla\nabla' \frac{1}{|r-r'|}\cdot\vec{m}(r') - SI. \tag{5.7}$$

where n is a density and α is the local polarizability that describes the cost of forming a dipole. The second term captures the interactions between spatially separated dipoles. This double integral includes a self interaction SI, which is the interaction of a dipole with itself. The parameter α is intended to completely describe the self interaction however, so we must subtract this term off as described below.

Let's consider a small volume v in which $\vec{m}(r)$ does not vary. In that case, the self interaction is given by:

$$SI = \frac{n^2}{2}\int_v\int_v drdr' \vec{m}\cdot\nabla\nabla' \frac{1}{|r-r'|}\cdot\vec{m} \tag{5.8}$$

We will evaluate this in Fourier space using the identity:

$$\frac{1}{|r-r'|} = \int \frac{d\vec{k}}{2\pi^3} e^{-i\vec{k}\cdot(r-r')}\frac{4\pi}{k^2}. \tag{5.9}$$

This gives us:

$$\nabla\nabla' \frac{1}{|r-r'|} = 4\pi\int \frac{d\vec{k}}{2\pi^3} e^{-i\vec{k}\cdot(r-r')}\hat{k}\hat{k}. \tag{5.10}$$

So that:

$$SI = 4\pi\frac{n^2}{2}\vec{m}\cdot\int_v\int_v drdr' \int \frac{d\vec{k}}{2\pi^3} e^{-i\vec{k}\cdot(r-r')}\hat{k}\hat{k}\cdot\vec{m}. \tag{5.11}$$

Now we'll take $\vec{m}$ to be along the z axis, which implies:

$$SI = 4\pi\frac{n^2}{2}m^2\int\frac{d\vec{k}}{2\pi^3}\frac{k_z^2}{k^2}\int_v dr e^{(-i\vec{k}\cdot r)}\int_v dr' e^{(-i\vec{k}\cdot r')} \tag{5.12}$$

The two real space integrals depend only on $|\vec{k}|$ and not on the orientation, so we can replace $\frac{k_z^2}{k^2}$ by $\frac{1}{3}$.

$$SI = 4\pi\frac{n^2}{2}\frac{m^2}{3}\int_v dr\int_v dr'\delta(r-r') = 4\pi\frac{n^2}{2}\frac{m^2}{3}v \tag{5.13}$$

integrating this over the entire volume gives:

$$SI = \frac{n^2}{2}\int dr\frac{4\pi}{3}|\vec{m(r)}|^2. \tag{5.14}$$

This means that the full Hamiltonian is given by

$$H = \frac{n}{2}\int dr|\vec{m}(r)|^2(\alpha^{-1}-\frac{4\pi n}{3}) + \frac{n^2}{2}\int\int dr dr'\vec{m}(r)\cdot\nabla\nabla'\frac{1}{|r-r'|}\cdot\vec{m}(r'), \tag{5.15}$$

which can be written explicitly as a set of coupled harmonic oscillators:

$$\beta H = \frac{1}{2}\int dr\int dr'\vec{m}(r)\cdot\chi^{-1}(r,r')\cdot\vec{m}(r'), \tag{5.16}$$

where

$$\chi^{-1}(r,r') = \beta n(\alpha^{-1}-\frac{4\pi n}{3})I\delta(r-r') + \beta n^2\nabla\nabla'\frac{1}{|r-r'|}. \tag{5.17}$$

We will refer to this object as a matrix with indices r and r'. In truth this connection is imperfect because these indices are continuous and not discrete. Certain properties of this matrix, like its determinant, are not defined unless you choose a finite basis (like a grid in real space or a set of Fourier modes with a high frequency cutoff). As we will see below we can define a functional inverse of this object which is analogous to the matrix inverse. Furthermore, each element of this matrix is itself a 3x3 matrix. That is, for any given value of r and r' the $\chi^{-1}(r,r')$ in a cartesian basis is:

$$\begin{pmatrix} \beta n(\alpha^{-1}-\frac{4\pi n}{3}) + \beta n^2\frac{\partial^2}{\partial x^2}\frac{1}{|r-r'|} & \beta n^2\frac{\partial^2}{\partial x\partial y}\frac{1}{|r-r'|} & \beta n^2\frac{\partial^2}{\partial x\partial z}\frac{1}{|r-r'|} \\ \beta n^2\frac{\partial^2}{\partial y\partial x}\frac{1}{|r-r'|} & \beta n(\alpha^{-1}-\frac{4\pi n}{3}) + \beta n^2\frac{\partial^2}{\partial y^2}\frac{1}{|r-r'|} & \beta n^2\frac{\partial^2}{\partial y\partial z}\frac{1}{|r-r'|} \\ \beta n^2\frac{\partial^2}{\partial z\partial x}\frac{1}{|r-r'|} & \beta n^2\frac{\partial^2}{\partial z\partial y}\frac{1}{|r-r'|} & \beta n(\alpha^{-1}-\frac{4\pi n}{3}) + \beta n^2\frac{\partial^2}{\partial z^2}\frac{1}{|r-r'|} \end{pmatrix}$$

5.4 Connecting microscopic and macroscopic pictures

Computing the statistical properties of such a system, like the polarization induced by an applied electric field $\mathcal{E}_o(r)$ is now a matter of computing multidimensional gaussian integrals. The partition function for this system coupled to such an external field is

$$Z = \int \mathcal{D}[\vec{m}(x)] \exp[-\frac{1}{2}\int dr \int dr' \vec{m}(r)\cdot \chi^{-1}(r,r')\cdot \vec{m}(r') - \beta n \int dr \vec{m}(r)\mathcal{E}_o(r)]. \quad (5.18)$$

There are a number of formally exact results for computing integrals like this and its derivatives. One such result relates the correlation function for $\vec{m}(r)$ to the matrix inverse of χ^{-1}:

$$\langle \vec{m}(r)\vec{m}(r')\rangle = \chi(r,r'), \quad (5.19)$$

where the matrix χ must satisfy $\int dr'\chi(r,r')\chi^{-1}(r',r'') = \delta(r-r'')$. We also describe the response to an external field in terms of this matrix as

$$\langle \vec{m}(r)n\rangle = n^2 \int dr' \beta \mathcal{E}_o(r)\cdot \chi(r,r'), \quad (5.20)$$

and for this reason $\chi(r,r')$ is called the response function. These results are only formally exact because we may not necessarily know what matrix will invert $\chi^{-1}(r,r')$, we can however use these results to make a connection to the more familiar macroscopic DCT without knowing $\chi(r,r')$.

If we identify $P(r)$ with $\langle \vec{m}(r)\rangle n$ then equation 5.6 and equation 5.20 are two different ways of computing the same thing, one from the macroscopic perspective and one from the microscopic perspective. To make the connection concrete however, we need to distinguish between the applied external field $\mathcal{E}_o$ and the field due to internal sources ($\mathcal{E}_i$) in equation 5.6:

$$\langle \vec{m}(r)\rangle n = \chi_e \mathcal{E}(r) = \chi_e(\mathcal{E}_o(r) + \mathcal{E}_i(r)). \quad (5.21)$$

We interpret $\mathcal{E}_i(r)$ as the field generated by the average polarization. The electric field at r due to a dipole $\vec{d}$ at r' is $\nabla\nabla'\frac{1}{|r-r'|}\cdot \vec{d}(r')$ which means that the total internal electric field is

$$\mathcal{E}_i(r) = -n \int dr' (\nabla\nabla' \frac{1}{|r-r'|})\cdot \langle \vec{m}(r')\rangle. \quad (5.22)$$

This integral is easier to evaluate than it looks. We can rearrange 5.17 so that we have $\nabla\nabla'\frac{1}{|r-r'|}$ in terms of $\chi^{-1}(r,r')$ and we can insert equation 5.20 to obtain

$$\mathcal{E}_i(r) = -n \int dr' \frac{1}{\beta n^2}[\chi^{-1}(r,r') - \beta n(\alpha^{-1} - \frac{4\pi n}{3})I\delta(r-r')]\cdot n \int dr'' \beta \mathcal{E}_o('')\cdot \chi(r',r''). \quad (5.23)$$

This equation reduces to

$$\mathcal{E}_i(r) = \frac{-1}{\beta n}[\int dr'' \beta n \mathcal{E}_o(r'')\delta(r-r'') - \beta n \int dr'(\alpha^{-1} - \frac{4\pi n}{3})I\delta(r-r')\langle\vec{m}(r')\rangle]. \quad (5.24)$$

By integrating over the delta functions we find that $\mathcal{E}_i$ is a simple function of $\mathcal{E}_o$ and the polarization.

$$\mathcal{E}_i(r) = -\mathcal{E}_o(r) + (\alpha^{-1} - \frac{4\pi n}{3})\langle\vec{m}(r)\rangle \quad (5.25)$$

By comparing this to the macroscopic equation we find

$$\chi_e = \frac{n}{(\alpha^{-1} - \frac{4\pi n}{3})} = \frac{\epsilon - 1}{4\pi}, \quad (5.26)$$

which leads to the Clausius-Mossotti equation relating the dielectric constant ϵ to the local susceptibility α:

$$\frac{4\pi n\alpha}{3} = \frac{\epsilon - 1}{\epsilon + 1} \quad (5.27)$$

5.5 Normal modes of a dielectric

The analysis in the last section provides us with an extremely useful result, but further applications will require us to actually have a form for the response function $\chi(r, r')$ which means we need to invert $\chi^{-1}(r, r')$. Using equation 5.27 we see that χ^{-1} can be rewritten as:

$$\chi^{-1}(r, r') = \frac{4\pi\beta n^2}{\epsilon - 1} I\delta(r - r') + \beta n^2 \nabla\nabla' \frac{1}{|r - r'|} \quad (5.28)$$

Finding the inverse of a matrix like this is easiest if you can find the basis in which it is diagonal, which is equivalent to finding its normal modes. This matrix is translationally invariant which means that its normal modes must be Fourier modes. Equation 5.10 tells us how to expand the second term in a Fourier basis. Expanding the first term in a Fourier basis requires the Fourier representation of the delta function, which is

$$\delta(r - r') = \int \frac{d\vec{k}}{(2\pi)^3} e^{-i\vec{k}\cdot(r-r')}. \quad (5.29)$$

The Fourier expansion of $\chi^{-1}(r, r')$ is therefore given by

$$\chi^{-1}(r, r') = \int \frac{d\vec{k}}{(2\pi)^3} e^{-i\vec{k}\cdot(r-r')}[\frac{4\pi\beta n^2}{\epsilon - 1} I + 4\pi\beta n^2 \hat{k}\hat{k}]. \quad (5.30)$$

The quantity in brackets is the $\hat{\chi}^{-1}(k)$, which as we can see has no off diagonal elements (there is no coupling between k and k' where $k \neq k'$). However, the 3x3 matrix that composes each

diagonal element is not itself diagonal. There is a convenient basis set for inverting matrices that involve I and the outer product of two unit vectors. This basis set is composed of the two elements

$$J_+ = \hat{k}\hat{k}, \tag{5.31}$$

and

$$J_- = I - \hat{k}\hat{k}. \tag{5.32}$$

These tensors have the following easily checked properties:

$$J_+ \cdot J_+ = J_+ \tag{5.33}$$
$$J_- \cdot J_- = J_- \tag{5.34}$$
$$J_+ \cdot J_- = 0. \tag{5.35}$$

These relationships imply the following identity for matrices that are a linear combination of these two tensors:

$$(aJ_+ + bJ_-) \cdot (a^{-1}J_+ + b^{-1}J_-) = I. \tag{5.36}$$

We can rewrite $\hat{\chi}^{-1}(k)$ in this form as

$$\hat{\chi}^{-1}(k) = 4\pi\beta n^2[\frac{1}{\epsilon - 1}(I - \hat{k}\hat{k}) + \frac{\epsilon}{\epsilon - 1}\hat{k}\hat{k}], \tag{5.37}$$

and we see right away from equation 5.36 that

$$\hat{\chi}(k) = (4\pi\beta n^2)^{-1}[(\epsilon - 1)(I - \hat{k}\hat{k}) + \frac{\epsilon - 1}{\epsilon}\hat{k}\hat{k}]. \tag{5.38}$$

Performing the inverse Fourier transform of this we find that the response function for a uniform dielectric is

$$\chi(r, r') = \frac{\epsilon - 1}{4\pi\beta n^2}[I\delta(r - r') - \frac{\epsilon - 1}{4\pi\epsilon}\nabla\nabla'\frac{1}{|r - r'|}]. \tag{5.39}$$

In what follows we will refer to this response function as χ^o.

5.6 Response function for a semi-infinite dielectric

The response function above accurately describes both the response to an external field and the correlation function for a perfectly uniform system. If we wish to consider systems that have a nonuniform dielectric constant then it describes neither. Imagine a system which has dielectric constant ϵ_1 in some region of space and dielectric constant ϵ_2 in other regions. It might seem reasonable to formulate the problem as a set of coupled harmonic oscillators

using an analogue of equation 5.16, in which α takes different values in different regions according to the Clausius-Mossotti equation (eq. 5.27). However, if $\epsilon_2 = 1$, then $\alpha = 0$ according to equation 5.27, which means there is an infinite penalty for locally forming a dipole in the ϵ_2 region. Chandler and Song ([58]) adopt the perspective that it is more natural to think of this sort of inhomogeneity as a constraint on a Gaussian field then as a region with a different local polarizability α. This perspective is less general because it only holds when the $\epsilon_2 = 1$, but this covers an important class of problems. If we denote the volume in which we impose the constraint V_2, the partition function of the constrained system is given by

$$Z = \int \mathcal{D}[\vec{m}(r)] \prod_{r \in V_2} \delta(\vec{m}(r)) \exp[-\frac{1}{2} \int dr \int dr' \vec{m}(r) \cdot \chi^{-1}(r, r') \cdot \vec{m}(r') - \beta n \int dr \vec{m}(r) \mathcal{E}_o(r)]. \tag{5.40}$$

In a formal sense this is simply a multidimensional gaussian integral, no more complicated than equation 5.18 except that the integral is over a smaller set of modes. The response function is still given by the inverse of $\chi^{-1}(r, r')$ except now r and r' have a restricted domain. The inverse condition is

$$\int_{V_1} dr' \chi(r, r') \chi^{-1}(r', r'') = \delta(r, r'') \tag{5.41}$$

In general, the function $\chi(r, r')$ that satisfies this equation depends on the geometry of V_1 (the unconstrained volume), meaning the nature of the correlations changes when you impose a constraint. In practice, solving equation 5.41 may be a very challenging numerical problem. In the previous section, we were able to invert $\chi^{-1}(r, r')$ by working in the Fourier basis, which is the normal mode basis of any translationally invariant system, however a constrained system does not have translational invariance and we don't necessarily know the normal modes. We will discuss a different method for calculating the response function when the region V_1 is the entire half of space below a plane at $z = 0$, which is the semi-infinite dielectric scenario of interest to us. We will adopt the following ansatz for the response function

$$\chi(r, r') = \frac{\epsilon - 1}{4\pi\beta n^2 \epsilon} \left(\epsilon \delta(r - r') I - \frac{\epsilon - 1}{4\pi} \nabla \nabla' \left(\frac{1}{|r - r'|} + g(r, r') \right) \right). \tag{5.42}$$

If we substitute this ansatz into equation 5.41, along with the definition of $\chi^{-1}(r, r')$ we obtain

$$-\frac{\epsilon - 1}{4\pi\epsilon} \nabla \nabla' \left(\frac{1}{|r - r'|} + g(r, r') \right) + \nabla' \left[\beta n^2 \int_{V_1} dr'' \chi(r, r'') \nabla'' \frac{1}{|r'' - r'|} \right] = 0. \tag{5.43}$$

We can evaluate the quantity in brackets using linear response theory. If we recognize that

$$\nabla'' \frac{1}{|r'' - r'|} = -\mathcal{E}^o(r'', r') \tag{5.44}$$

where $\mathcal{E}^o(r'', r')$ is the external electric field at r'' due to a unit point charge at r', then we see from equation 5.20 that the quantity in brackets is the polarization at r due to a point charge at r'. From macroscopic electrostatics (equation 5.6), we know that this polarization is equal to the susceptibility times the total electric field. If we make the substitution $P(r) = \vec{m}(r)n$ and $\chi_e = \frac{\epsilon-1}{4\pi}$ then equation 5.6 becomes

$$\vec{m}(r)n = \frac{\epsilon - 1}{4\pi}\mathcal{E}(r). \tag{5.45}$$

Which says that we can solve for the average polarization if we know the total electric field (from both internal and external sources) due to a point charge. For the case considered here, in which V_1 is the half space below a plane, this electric field has the image charge form described in chapter 1

$$\mathcal{E}(r) = -\frac{1}{\epsilon}\left(\frac{1}{|r - r'|} + \frac{\epsilon - 1}{\epsilon + 1}\frac{1}{|r - r'_z|}\right), \tag{5.46}$$

where r'_z is the vector r' with the z-coordinate reflected through the boundary between the dielectric and the vaccum. This means that the term in brackets is

$$\beta n^2 \int_{V_1} dr'' \chi(r, r'')\nabla'' \frac{1}{|r'' - r'|} = \frac{\epsilon - 1}{4\pi}\nabla\frac{1}{\epsilon}\left(\frac{1}{|r - r'|} + \frac{\epsilon - 1}{\epsilon + 1}\frac{1}{|r - r'_z|}\right), \tag{5.47}$$

and equation 5.43 can now be rewritten as

$$-\frac{\epsilon - 1}{4\pi\epsilon}\nabla\nabla'\left(\frac{1}{|r - r'|} + g(r, r')\right) + \frac{\epsilon - 1}{4\pi}\nabla'\nabla\frac{1}{\epsilon}\left(\frac{1}{|r - r'|} + \frac{\epsilon - 1}{\epsilon + 1}\frac{1}{|r - r'_z|}\right) = 0. \tag{5.48}$$

From this expression we can easily read off that $g(r, r') = \frac{\epsilon-1}{\epsilon+1}\frac{1}{|r-r'_z|}$. The full response function is then given by:

$$\chi(r, r') = \frac{\epsilon - 1}{4\pi\beta n^2\epsilon}\left(\epsilon\delta(r - r')I - \frac{\epsilon - 1}{4\pi}\nabla\nabla'\left(\frac{1}{|r - r'|} + \frac{\epsilon - 1}{\epsilon + 1}\frac{1}{|r - r'_z|}\right)\right) \tag{5.49}$$

The analysis described here is very general, and it allows you to find an exact analytical form for the response function in any geometry for which you know the total electric field $\mathcal{E}(r)$ due to a point charge.

The geometry we are most interested in is the one depicted in figure 5.1 in which the space of the plane and the interior of a sphere are constrained. In this case we can not solve for the electric field exactly and the method described here will not work. It may seem that the simplest approach is to find a numerical solution to 5.41, but this is very difficult due to the fact that the space V_1, and therefore the size of the matrix you need to invert, is infinite.

Chandler show that there is a much easier way to solve such problems when you only want to constrain a small region of space. Given a response function $\chi(r, r')$, you can compute the modified response function due to imposing a constraint in some small region as

$$\chi^m(r, r') = \chi(r, r') - \int_{in}\int_{in} dr''dr'''\chi(r, r'') \cdot \chi^{-1}_{in}(r'', r''') \cdot \chi(r''', r'), \tag{5.50}$$

where $\chi^{-1}_{in}(r, r'')$ satisfies(for r and r' in):

$$\int_{in} dr''\chi^{-1}_{in}(r, r'')\cdot \chi(r'', r') = \delta(r - r')I. \tag{5.51}$$

The *in* region here is the interior of the region occupied by the solute. This is a numerical problem that only requires us to invert a finite (and probably very small) matrix.

5.7 Solvation free energy of point charges in a cavity

Among the interesting things we can compute when we know the response function for a given geometry is the solvation free energy of point charges in a cavity. The general expression for such a free energy is

$$E = -\frac{\beta n^2}{2}\int_{V_1}\int_{V_1} drdr'\nabla\frac{1}{|r - r_o|}\chi^m(r, r')\nabla'\frac{1}{|r' - r_o|}. \tag{5.52}$$

where χ^m is the modified response function given by equation 5.50 and V_1 is the unconstrained region. If we insert the definition of χ^m we see that the energy breaks up naturally into two terms. The first is

$$E_o = -\frac{\beta n^2}{2}\int_{V_1}\int_{V_1} drdr'\nabla\frac{1}{|r - r_o|}\chi(r, r')\nabla'\frac{1}{|r' - r_o|}, \tag{5.53}$$

and the second is

$$E_c = -\frac{\beta n^2}{2}\int_{V_1}\int_{V_1} drdr'\nabla\frac{1}{|r - r_o|}\int_{in}\int_{in} dr''dr'''\chi(r, r'') \cdot \chi^{-1}_{in}(r'', r''') \cdot \chi(r''', r')\nabla'\frac{1}{|r' - r_o|}, \tag{5.54}$$

so that

$$E = E_o - E_c \tag{5.55}$$

To evaluate E_o we rearrange equation 5.43 to find

$$\beta n^2\int_{V_1} dr'\chi(r, r')\nabla'\frac{1}{|r' - r_o|} = \frac{\epsilon - 1}{4\pi\epsilon}\nabla\left[\frac{1}{|r - r_o|} + g(r, r_o)\right] = \frac{\epsilon - 1}{4\pi\epsilon}\nabla G(r, r_o), \tag{5.56}$$

where the last line defines the function $G(r, r_o)$. Plugging this into the equation for E_o we find

$$E_o = -\frac{\epsilon - 1}{8\pi\epsilon}\int_{V_1} dr\nabla\frac{1}{|r - r_o|}\nabla G(r, r_o). \tag{5.57}$$

We could try to evaluate this integral analytically using integration by parts, but this is not actually necessary. To see this, we maniuplate equation 5.56 further by inserting the definition χ from equation 5.49. This gives us

$$\frac{\epsilon-1}{4\pi}\nabla\frac{1}{|r-r_o|}-\frac{(\epsilon-1)^2}{(4\pi)^2\epsilon}\int dr'\nabla\nabla' G(r,r')\nabla'\frac{1}{|r'-r_o|}=\frac{\epsilon-1}{4\pi\epsilon}\nabla G(r,r_o). \tag{5.58}$$

If cross out the ∇ the integral in this equation resembles the integral in equation 5.57. This gives us

$$\frac{(\epsilon-1)^2}{4\pi\epsilon}\int dr'\nabla' G(r,r')\nabla'\frac{1}{|r'-r_o|}=-\frac{\epsilon-1}{\epsilon}G(r,r_o)+(\epsilon-1)\frac{1}{|r-r_o|}. \tag{5.59}$$

And by comparing to equation 5.57 we find

$$E_o=-\frac{\epsilon-1}{2\epsilon}\frac{1}{|r_o-r_o|}+\frac{1}{2\epsilon}g(r_o,r_o). \tag{5.60}$$

Now we turn to evaluating E_c, we will find that a similar set of tricks allow us to bypass doing any difficult integrals. If we use equation 5.56 we find that we can immediately perform the integrals over r and r' in equation 5.54 and we find

$$E_c=-\frac{1}{2\beta n^2}(\frac{\epsilon-1}{4\pi\epsilon})^2\int\int_{in}dr''dr'''\nabla''G(r'',r_o)\cdot\chi_{in}^{-1}(r'',r''')\cdot\nabla'''G(r''',r_o). \tag{5.61}$$

To proceed further we need to define χ_{in}^{-1}. We adopt an ansatz which has the following general form:

$$\chi_{in}^{-1}(r'',r''')=\frac{\beta n^2 4\pi}{\epsilon-1}\delta(r''-r''')I+\beta n^2\nabla''\nabla'''G(r'',r''')+\frac{\beta n^2 4\pi\epsilon}{\epsilon-1}\nabla''\nabla'''f(r'',r'''), \tag{5.62}$$

and it satisfies the equation

$$\int_{in}dr'''\chi_{in}^{-1}(r'',r''')\chi(r''',r_o)=\delta(r'',r_o)I. \tag{5.63}$$

If we insert $\chi(r''',r_o)$ (from equation 5.49) into this equation we get:

$$\frac{\epsilon-1}{4\pi\beta n^2}\chi_{in}^{-1}(r'',r_o)-\left(\frac{\epsilon-1}{4\pi}\right)^2\frac{1}{\epsilon\beta n^2}\int dr'''\chi_{in}^{-1}(r'',r''')\nabla'''\nabla G(r''',r_o)=\delta(r'',r_o)I \tag{5.64}$$

If we insert the definition of χ_{in}^{-1} we find the delta functions on either side of this equation cancel and we are left with

$$\left(\frac{\epsilon-1}{4\pi}\right)^2 \frac{1}{\epsilon\beta n^2}\int dr'''\chi_{in}^{-1}(r'',r''')\nabla'''\nabla G(r''',r_o) = \frac{\epsilon-1}{4\pi}\nabla''\nabla\left[G(r'',r_o)+\frac{4\pi\epsilon}{\epsilon-1}f(r'',r_o)\right]. \tag{5.65}$$

Rearranging slightly and crossing out the ∇ we find

$$\int dr'''\chi_{in}^{-1}(r'',r''')\nabla'''G(r''',r_o) = \frac{4\pi\epsilon\beta n^2}{\epsilon-1}\nabla''\left[G(r'',r_o)+\frac{4\pi\epsilon}{\epsilon-1}f(r'',r_o)\right]. \tag{5.66}$$

The left hand side of this equation appears in the expression for E_c, equation 5.61, so we can immediately perform the integral over r''' and we are left with

$$E_c = -\frac{1}{2}(\frac{\epsilon-1}{4\pi\epsilon})\int_{in} dr''\nabla''G(r'',r_o)\nabla''\left[G(r'',r_o)+\frac{4\pi\epsilon}{\epsilon-1}f(r'',r_o)\right]. \tag{5.67}$$

To evaluate this integral we must write out equation 5.66 in more detail by inserting the definition of χ_{in}^{-1}. This leaves us with

$$\frac{4\pi}{\epsilon-1}\nabla''G(r'',r_o)+\int dr'''\nabla''\nabla'''\left[G(r'',r''')+\frac{4\pi}{\epsilon-1}f(r'',r''')\right]\nabla'''G(r''',r_o) = \frac{4\pi\epsilon}{\epsilon-1}\nabla''\left[G(r'',r_o)+\frac{4\pi\epsilon}{\epsilon-1}f(r'',r_o)\right].$$

If we cross out ∇'' and rearrange slightly we find

$$\int dr'''\nabla'''\left[G(r'',r''')+\frac{4\pi}{\epsilon-1}f(r'',r''')\right]\nabla'''G(r''',r_o) = 4\pi G(r'',r_o)+(\frac{4\pi\epsilon}{\epsilon-1})^2 f(r'',r_o). \tag{5.68}$$

The integral on the left side very nearly resembles the integral that appears in 5.61. We need only set r'' equal to r_o, and then change the integration index from r''' to r'' and we find

$$\int dr''\nabla''G(r'',r_o)\nabla''\left[G(r'',r_o)+\frac{4\pi}{\epsilon-1}f(r'',r_o)\right] = 4\pi G(r_o,r_o)+(\frac{4\pi\epsilon}{\epsilon-1})^2 f(r_o,r_o). \tag{5.69}$$

This equation allows to evaluate E_c immediately as

$$E_c = -\frac{1}{2}\left(\frac{\epsilon-1}{\epsilon}G(r_o,r_o)+\frac{4\pi\epsilon}{\epsilon-1}f(r_o,r_o)\right). \tag{5.70}$$

Finally we compile the total solvation energy as

$$E = E_o - E_c = \frac{2\pi\epsilon}{\epsilon-1}f(r_o,r_o)+\frac{1}{2}g(r_o,r_o). \tag{5.71}$$

5.8 Integral equations for $f(r, r')$

Equation 5.71 is a compact expression for the solvation free energy of a point charge inside a cavity in terms of the function $f(r, r')$. Equation 5.68 is the integral equation that determines this function. We will rearrange this equation slightly and change variable names so that the subsequent discussion parallels the discussion in the Song and Chandler paper [57]:

$$\begin{aligned}\epsilon f(r,r') + \frac{(\epsilon-1)^2}{4\pi\epsilon}G(r,r') - \left(\frac{\epsilon-1}{4\pi}\right)^2 \frac{1}{\epsilon}\int_{in} dr''\nabla''G(r,r'')\nabla''G(r'',r') \\ - \frac{\epsilon-1}{4\pi}\int_{in} dr''\nabla''f(r,r'')\nabla''G(r'',r') = 0.\end{aligned} \tag{5.72}$$

In this section we will describe a method for solving this equation when the *in* region is a sphere, and that sphere is not penetrating the boundary (case a in figure 5.1). Solving this equation will proceed in two steps. First we will solve for $f(r, R)$, where R is on the boundary of the sphere. Once we know its value on the boundary we can then solve for its value in the interior (details will follow shortly).

To begin with we choose r to be at the center of the cavity and r' to be on the boundary and we will apply integration by parts to each of the integrals above. As an example, if we integrate the second integral by parts we obtain

$$\int_{in} dr''\nabla''f(r,r'')\nabla''G(r'',r') = \int_{surf} da_{R''}f(r,R'')\nabla_n G(R'',R') - \int_{in} dr''f(r,r'')\nabla^2 G(r'',R'), \tag{5.73}$$

where we have adopted the notation that a capital R indicates a point on the surface. Recall that the definition of $G(r'', r')$ is

$$G(r'',r') = \frac{1}{|r-r'|} + \frac{\epsilon-1}{\epsilon+1}\frac{1}{|r-r'_z|}. \tag{5.74}$$

This means that

$$\nabla^2 G(r'',R') = -4\pi\left(\delta(r'',R') + \frac{\epsilon-1}{\epsilon+1}\delta(r'',R'_z)\right) \tag{5.75}$$

which is a delta function centered on the boundary. The second integral in equation 5.73 only picks up half of this delta function. This means that the integral equation 5.72 can be rewritten as

$$\begin{aligned}\frac{\epsilon+1}{2}f(r,R') - (\frac{\epsilon-1}{4\pi})^2\frac{1}{\epsilon}\int_{surf} da_{R''}\nabla_n G(r,R'')G(R'',R') \\ - \frac{\epsilon-1}{4\pi}\int_{surf} da_{R''}f(r,R'')\nabla_n G(R'',R') = 0.\end{aligned} \tag{5.76}$$

This integral equation determines $f(r, R)$, where R is on the boundary. We will have a separate equation below to determine $f(r, r')$ where both r and r' are in the interior. We will solve this using a spherical harmonics expansion and the identity

$$\frac{1}{|r - r'|} = 4\pi \sum_{l=0}^{\infty} \sum_{m=-l}^{l} \frac{1}{2l+1} \frac{r_<^l}{r_>^{l+1}} Y_{lm}^*(\theta', \phi') Y_{lm}(\theta, \phi) \tag{5.77}$$

The spherical harmonics expansion is natural because the surface integrals in equation 5.76 are over the surface of a sphere, and the spherical harmonics form an orthonormal basis on this surface. To be explicit, the integrals in equation 5.76 are

$$\int_{surf} da_{R''} = L^2 \int_0^{2\pi} d\phi'' \int_0^{\pi} d\theta'' \tag{5.78}$$

where L is the radius of the sphere and θ and ϕ are the usual polar and azimuthal angles, respectively. The spherical harmonics obey the property:

$$\int_0^{2\pi} d\phi'' \int_0^{\pi} d\theta'' Y_{lm}^*(\theta'', \phi'') Y_{l'm'}(\theta'', \phi'') = \delta_{l,l'} \delta_{m,m'} \tag{5.79}$$

Because we have chosen r to be at the center of the sphere, $f(r, R')$ depends only on the polar angle θ' and we need only keep terms in its spherical harmonics expansion for which $m = 0$. For this reason we will drop the m subscript and just write

$$f(r, R') = f_l Y_l(\theta'). \tag{5.80}$$

Equation 5.76 requires a spherical harmonics expansion for the function $G(R'', R')$ which does not have azimuthal symmetry and therefore its expansion would necessarily have terms for which $m \neq 0$. However, $G(r, R'')$ does have the azimuthal symmetry and the consequent vanishing $m \neq 0$ spherical harmonic components. This means that when you evaluate the first (or the second) integral in equation 5.76 only the $m = 0$ terms matter because of the orthonormality condition. We will therefore only keep track of $m = 0$ terms in an expansion of $G(R'', R')$, which will look like

$$G(R'', R') = G_l Y_l(\theta) Y_l(\theta') \tag{5.81}$$

Now we will construct explicit forms for the spherical harmonics expansions of the various terms in equation 5.76. First of all, the first term and the second term in5.74 should be handled separately because the first is a standard Coulomb potential and its expansion is given by equation 5.77. The spherical harmonics components of the second terms have to evaluated analytically or numerically term by term. For later reference we will write out the functional forms of these second terms:

$$\frac{1}{|r - R'_z|} = \frac{1}{(4d^2 + L^2 - 4dL\cos(\theta'))^{1/2}} = \frac{\epsilon + 1}{\epsilon - 1} g(r, R') \tag{5.82}$$

and

$$\frac{1}{|R'' - R'_z|} = \frac{1}{(2L^2(1-\sin(\theta'')\sin(\theta')\cos(\phi'')) - 4Ld(\cos(\theta'')+\cos(\theta')) + 4d^2 + 2L^2\cos(\theta'')\cos(\theta'))^{1/2}} = \frac{\epsilon+1}{\epsilon-1} g(R'', R') \quad (5.83)$$

The spherical harmonics expansions of the first G term in equation 5.76 is

$$\nabla_n G(r, R'') = \sum_l -\delta_{l,0}\frac{\sqrt{4\pi}}{L^2} Y_l(\theta'') + \sum_l A_l Y_l(\theta''), \quad (5.84)$$

where

$$A_l = \int_0^{2\pi} d\phi' \int_0^{\pi} d\theta' \nabla' g(r, R') Y_l(\theta'). \quad (5.85)$$

And for the second G term we have

$$G(R'', R') = \sum_l \frac{4\pi}{2l+1}\frac{1}{L} Y_l(\theta'') Y_l(\theta') + \sum_l B_l Y_l(\theta'') Y_l(\theta') \quad (5.86)$$

where

$$B_l = \int_0^{2\pi} d\phi' \int_0^{\pi} d\theta' \int_0^{2\pi} d\phi'' \int_0^{\pi} d\theta'' g(R'', R') Y_l(\theta') Y_l(\theta''). \quad (5.87)$$

And finally

$$\nabla_n G(R'', R') = \sum_l \frac{-4\pi}{2(2l+1)}\frac{1}{L^2} Y_l(\theta'') Y_l(\theta') + \sum_l C_l Y_l(\theta'') Y_l(\theta') \quad (5.88)$$

where

$$C_l = \int_0^{2\pi} d\phi' \int_0^{\pi} d\theta' \int_0^{2\pi} d\phi'' \int_0^{\pi} d\theta'' \nabla_n g(R'', R') Y_l(\theta') Y_l(\theta''). \quad (5.89)$$

If we plug all of these along with equation 5.80 into equation 5.76, and then integrate over the angles we find:

$$f_l\left(\frac{\epsilon+1}{2} - \frac{\epsilon-1}{4\pi}\left(-\frac{4\pi}{2(2l+1)} + L^2 C_l\right)\right) = (\frac{\epsilon-1}{4\pi})^2 \frac{1}{\epsilon}\left(-\delta_{l,0}\sqrt{4\pi} + L^2 A_l\right)\left(\frac{4\pi}{2l+1}\frac{1}{L} + B_l\right) \quad (5.90)$$

We now turn our attention to solving for $f(r, r')$ when both r and r' are in the interior. If we take both r and r' to be at the center of the sphere, and then we integrate equation 5.72 by parts we obtain a different integral equation

$$f(r,r) - (\frac{\epsilon-1}{4\pi})^2 \frac{1}{\epsilon} \int_{surf} da_{R''} \nabla_n G(r,R'') G(R'',r) - \frac{\epsilon-1}{4\pi} \int_{surf} da_{R''} f(r,R'') \nabla_n G(R'',r) = 0, \tag{5.91}$$

which takes the surface solution $f(r, R'')$ as input. To solve this equation we will again use a spherical harmonics expansion. For the terms $\nabla_n G(r, R'')$ and $\nabla_n G(R'', r)$ we already have the spherical harmonics expansion (equation 5.84). The remaining required expansion is

$$G(R'', r') = \sum_l \delta_{l,0} \frac{\sqrt{4\pi}}{L} Y_l(\theta'') + \sum_l D_l Y_l(\theta'') \tag{5.92}$$

where

$$D_l = \int_0^{2\pi} d\phi' \int_0^{\pi} d\theta' g(R'', r) Y_l(\theta'). \tag{5.93}$$

Performing the spherical harmonics expansion on equation 5.91 we find

$$f(r,r') = \sum_l (\frac{\epsilon-1}{4\pi})^2 \frac{1}{\epsilon} \left(-\delta_{l,0}\sqrt{4\pi} + L^2 A_l \right) \left(\sqrt{4\pi} \frac{\delta_{l,0}}{L} + D_l \right) \sum_l \frac{\epsilon-1}{4\pi} f_l \left(-\delta_{l,0} \frac{\sqrt{4\pi}}{L} + A_l \right) \tag{5.94}$$

We can evaluate analytically evaluate this equation and equation 5.90 to lowest order in the expansion. If we assume that the cavity is very far from the interface so that $d >> L$ then we find that

$$B_o = \frac{1}{2d} \int_0^{2\pi} d\phi' \int_0^{\pi} d\theta' \int_0^{2\pi} d\phi'' \int_0^{\pi} d\theta'' Y_0(\theta') Y_0(\theta'') = \frac{4\pi}{2d} \tag{5.95}$$

If we neglect all higher order terms along with all the A_l and C_l (which are higher order in $\frac{d}{L}$) we find

$$f_o = \frac{(\epsilon-1)^2}{\epsilon^2} \frac{1}{\sqrt{4\pi}} \left(\frac{1}{L} + \frac{\epsilon-1}{\epsilon+1} \frac{1}{2d} \right) \tag{5.96}$$

D_o can be evaluated in a similarly straightforward way in the limit that $d >> L$:

$$D_o = \frac{1}{2d} \int_0^{2\pi} d\phi' \int_0^{\pi} d\theta' Y_0(\theta') = \frac{\sqrt{4\pi}}{2d} \tag{5.97}$$

Now we take the first term in the sum in equation 5.96 (neglecting A_o) and we find

$$f(r,r) \simeq -\frac{(\epsilon-1)^2}{4\pi\epsilon^2}\left(\frac{1}{L}+\frac{\epsilon-1}{\epsilon+1}\frac{1}{2d}\right) \tag{5.98}$$

This is the function that appears in the expression for the solvation free energy 5.71, and if we substitute this expression into that equation we finally have

$$E(L,d) \simeq \frac{\epsilon-1}{2\epsilon}\frac{1}{L}+\frac{\epsilon-1}{\epsilon(\epsilon+1)}\frac{1}{4d} \tag{5.99}$$

The first term here is the born solvation energy for a unit point charge at the center of a cavity with radius L, and the second term is the interaction between that charge and its image charge. This result is often claimed to be an exact result for the cavity below the interface [3] but we see here that it is only in fact a lowest order result. Extending this to higher order (and to the case where the cavity is penetrating the boundary) requires some numerical work which is not yet complete.

Bibliography

[1] M.P. Allen and D.J. Tildesley. *Computer Simulation of Liquids*. Oxford: Oxford University Press, 1991.

[2] Georgios Archontis and Epameinondas Leontidis. "Dissecting the stabilization of iodide at the air-water interface into components: A free energy analysis". In: *Chemical Physics Letters* 420.1-3 (Mar. 2006), pp. 199–203. ISSN: 0009-2614. DOI: 16/j.cplett.2005.12.051. URL: http://www.sciencedirect.com/science/article/pii/S0009261405019482http://www.sciencedirect.com/science?_ob=MImg\&_imagekey=B6TFN-4J2TSRG-1-13\&_cdi=5231\&_user=4420\&_pii=S0009261405019482\&_origin=browse\&_coverDate=03/10/2006\&_sk=995799998\&view=c\&wchp=dGLzVzz-zSkzV\&md5=541fd3f77330951c6212958dd7204040\&ie=/sdarticle.pdf.

[3] Marcel D. Baer et al. "Electrochemical Surface Potential Due to Classical Point Charge Models Drives Anion Adsorption to the AirWater Interface". In: *The Journal of Physical Chemistry Letters* 3.11 (June 2012), pp. 1565–1570. ISSN: 1948-7185. DOI: 10.1021/jz300302t. URL: http://pubs.acs.org/doi/abs/10.1021/jz300302t.

[4] Thomas L Beck. "The influence of water interfacial potentials on ion hydration free energies and density profiles near the surface". In: *Arxiv* (2013), pp. 1–29. arXiv:arXiv:1209.4516v1.

[5] H J C Berendsen, J R Grigera, and T P Straatsma. "The Missing Term in Effective Pair Potentials". In: *The Journal of Physical Chemistry* 91.24 (1987), pp. 6269–6271.

[6] Divesh Bhatt et al. "Molecular simulation of the surface tension of simple aqueous electrolytes and the Gibbs adsorption equation". In: *Current Opinion in Colloid & Interface Science* 9.1-2 (Aug. 2004), pp. 145–148. ISSN: 13590294. DOI: 10.1016/j.cocis.2004.05.020. URL: http://linkinghub.elsevier.com/retrieve/pii/S1359029404000470.

[7] Carl Caleman et al. "Atomistic simulation of ion solvation in water explains surface preference of halides". In: *Proceedings of the National Academy of Sciences* 108.17 (Apr. 2011), pp. 6838 –6842. DOI: 10.1073/pnas.1017903108. URL: http://www.pnas.org/content/108/17/6838.abstracthttp://www.pnas.org/content/108/17/6838.abstract?sid=40eee614-e963-484e-aeac-3ecd1812e3c5http://www.pnas.org/content/108/17/6838.full.pdf.

[8] David Chandler. "Gaussian field model of fluids with an application to polymeric fluids". In: *Physical Review E* 48.4 (1993), pp. 2898–2905.

[9] David Chandler. "Hydrophobicity: Two faces of water". In: *Nature* 417.6888 (May 2002), p. 491. ISSN: 0028-0836. DOI: 10.1038/417491a. URL: http://dx.doi.org/10.1038/417491ahttp://www.nature.com/nature/journal/v417/n6888/full/417491a.htmlhttp://www.nature.com/nature/journal/v417/n6888/pdf/417491a.pdf.

[10] David Chandler. "Interfaces and the driving force of hydrophobic assembly". In: *Nature* 437.7059 (2005), pp. 640–647. ISSN: 0028-0836. DOI: 10.1038/nature04162. URL: http://dx.doi.org/10.1038/nature04162http://www.nature.com/nature/journal/v437/n7059/full/nature04162.htmlhttp://www.nature.com/nature/journal/v437/n7059/pdf/nature04162.pdf.

[11] David Chandler. *Introduction to Modern Statistical Mechanics*. Oxford University Press, 1987.

[12] Liem X. Dang and Tsun-Mei Chang. "Molecular dynamics study of water clusters, liquid, and liquidvapor interface of water with many-body potentials". In: *The Journal of Chemical Physics* 106.19 (1997), p. 8149. ISSN: 00219606. DOI: 10.1063/1.473820. URL: http://link.aip.org/link/JCPSA6/v106/i19/p8149/s1\&Agg=doi.

[13] Liem X Dang and Tsun-Mei Chang. "Molecular Mechanism of Ion Binding to the Liquid / Vapor Interface of Water". In: *J. Phys. Chem. B* 106 (2002), pp. 235–238.

[14] LX Dang. "Computational study of ion binding to the liquid interface of water". In: *The Journal of Physical Chemistry B* (2002), pp. 10388–10394. URL: http://pubs.acs.org/doi/abs/10.1021/jp021871t.

[15] Q Du et al. "Vibrational Spectroscopy of Water at the Vapor/Water Interface". In: *Physical Review Letters* 70.15 (1993), pp. 2313–2316.

[16] Maxim V. Fedorov and Alexei a. Kornyshev. "Unravelling the solvent response to neutral and charged solutes". In: *Molecular Physics* 105.1 (Jan. 2007), pp. 1–16. ISSN: 0026-8976. DOI: 10.1080/00268970601110316. URL: http://www.tandfonline.com/doi/abs/10.1080/00268970601110316.

[17] Daan Frenkel and Berend Smit. *Understanding Molecular Simulation: From Algorithms to Applications*. London, UK: Academic Press, 2002.

[18] Edward Harder and Benoît Roux. "On the origin of the electrostatic potential difference at a liquid-vacuum interface." In: *The Journal of chemical physics* 129.23 (Dec. 2008), p. 234706. ISSN: 1089-7690. DOI: 10.1063/1.3027513. URL: http://www.pubmedcentral.nih.gov/articlerender.fcgi?artid=2671189\&tool=pmcentrez\&rendertype=abstract.

[19] Christine L Henry and Vincent S J Craig. "Ion-specific influence of electrolytes on bubble coalescence in nonaqueous solvents." In: *Langmuir : the ACS journal of surfaces and colloids* 24.15 (Aug. 2008), pp. 7979–85. ISSN: 0743-7463. DOI: 10.1021/la8008738. URL: http://www.ncbi.nlm.nih.gov/pubmed/18598065.

[20] Christine L Henry and Vincent S J Craig. "The link between ion specific bubble coalescence and Hofmeister effects is the partitioning of ions within the interface." In: *Langmuir : the ACS journal of surfaces and colloids* 26.9 (May 2010), pp. 6478–83. ISSN: 1520-5827. DOI: 10.1021/la9039495. URL: http://www.ncbi.nlm.nih.gov/pubmed/20092343.

[21] Christine L. Henry et al. "Ion-Specific Coalescence of Bubbles in Mixed Electrolyte Solutions". In: *The Journal of Physical Chemistry C* 111.2 (Jan. 2007), pp. 1015–1023. ISSN: 1932-7447. DOI: 10.1021/jp066400b. URL: http://pubs.acs.org/doi/abs/10.1021/jp066400b.

[22] J H Hu et al. "Reactive Uptake of Cl_2(g) and BR_2(g) by Aqueous Surfaces as a Function of Br- and I- Ion Concentration: The effect of Chemical Reaction at the Interface". In: *Journal of Physical Chemistry* 99.4 (1995), pp. 8768–8776.

[23] G Hummer et al. "An information theory model of hydrophobic interactions." In: *Proceedings of the National Academy of Sciences of the United States of America* 93.17 (Aug. 1996), pp. 8951–5. ISSN: 0027-8424. URL: http://www.pubmedcentral.nih.gov/articlerender.fcgi?artid=38575\&tool=pmcentrez\&rendertype=abstract.

[24] Gerhard Hummer, Lawrence R. Pratt, and Angel E. García. "Free Energy of Ionic Hydration". In: *The Journal of Physical Chemistry* 100.4 (Jan. 1996), pp. 1206–1215. ISSN: 0022-3654. DOI: 10.1021/jp951011v. URL: http://dx.doi.org/10.1021/jp951011v.

[25] Gerhard Hummer, Lawrence R. Pratt, and Angel E. Garcia. "Ion sizes and finite-size corrections for ionic-solvation free energies". In: *The Journal of Chemical Physics* 107.21 (1997), p. 9275. ISSN: 00219606. DOI: 10.1063/1.475219. URL: http://link.aip.org/link/JCPSA6/v107/i21/p9275/s1\&Agg=doi.

[26] Gerhard Hummer, Lawrence R Pratt, and Angel E Garc. "Molecular Theories and Simulation of Ions and Polar Molecules in Water". In: 5639.98 (1998), pp. 7885–7895.

[27] Diana Ionescu and R.a. Ionescu. "Analytical insights on ion behaviour at interfaces". In: *Journal of Electroanalytical Chemistry* 650.2 (Jan. 2011), pp. 205–208. ISSN: 15726657. DOI: 10.1016/j.jelechem.2010.10.006. URL: http://linkinghub.elsevier.com/retrieve/pii/S1572665710003930.

[28] Satoru Iuchi et al. "Hydrated excess proton at water-hydrophobic interfaces." In: *The journal of physical chemistry. B* 113.13 (Apr. 2009), pp. 4017–30. ISSN: 1520-6106. DOI: 10.1021/jp805304j. URL: http://www.ncbi.nlm.nih.gov/pubmed/18821788.

[29] John David Jackson. *Classical Electrodynamics*. 3rd. John Wiley & Sons, Inc., 1999.

[30] Pavel Jungwirth and Douglas J Tobias. "Specific ion effects at the air/water interface." In: *Chemical reviews* 106.4 (Apr. 2006), pp. 1259–81. ISSN: 0009-2665. DOI: 10.1021/cr0403741. URL: http://www.ncbi.nlm.nih.gov/pubmed/16608180.

[31] Shawn M Kathmann et al. "Understanding the surface potential of water." In: *The journal of physical chemistry. B* 115.15 (Apr. 2011), pp. 4369–77. ISSN: 1520-5207. DOI: 10.1021/jp1116036. URL: http://www.ncbi.nlm.nih.gov/pubmed/21449605.

[32] Yurij I. Kharkats and Jens Ulstrup. "The electrostatic Gibbs energy of finite-size ions near a planar boundary between two dielectric media". In: *Journal of Electroanalytical Chemistry* 308 (1991), pp. 17–26.

[33] W. Kunz, J. Henle, and B.W. Ninham. "Zur Lehre von der Wirkung der Salze (about the science of the effect of salts): Franz Hofmeister's historical papers". In: *Current Opinion in Colloid & Interface Science* 9.1-2 (Aug. 2004), pp. 19–37. ISSN: 13590294. DOI: 10.1016/j.cocis.2004.05.005. URL: http://linkinghub.elsevier.com/retrieve/pii/S1359029404000317.

[34] Igor Leontyev and Alexei Stuchebrukhov. "Accounting for electronic polarization in non-polarizable force fields." In: *Physical chemistry chemical physics : PCCP* 13.7 (Feb. 2011), pp. 2613–26. ISSN: 1463-9084. DOI: 10.1039/c0cp01971b. URL: http://www.ncbi.nlm.nih.gov/pubmed/21212894.

[35] Yan Levin. "Polarizable Ions at Interfaces". In: *Physical Review Letters* 102.14 (Apr. 2009), pp. 1–4. ISSN: 0031-9007. DOI: 10.1103/PhysRevLett.102.147803. URL: http://link.aps.org/doi/10.1103/PhysRevLett.102.147803.

[36] Dingfang Liu et al. "Vibrational Spectroscopy of Aqueous Sodium Halide Solutions and AirLiquid Interfaces: Observation of Increased Interfacial Depth". In: *The Journal of Physical Chemistry B* 108.7 (Feb. 2004), pp. 2252–2260. ISSN: 1520-6106. DOI: 10.1021/jp036169r. URL: http://pubs.acs.org/doi/abs/10.1021/jp036169r.

[37] Ka Lum, David Chandler, and John D. Weeks. "Hydrophobicity at Small and Large Length Scales". In: *The Journal of Physical Chemistry B* 103.22 (June 1999), pp. 4570–4577. DOI: 10.1021/jp984327m. URL: http://dx.doi.org/10.1021/jp984327mhttp://pubs.acs.org/doi/abs/10.1021/jp984327mhttp://pubs.acs.org/doi/full/10.1021/jp984327mhttp://pubs.acs.org/doi/pdf/10.1021/jp984327m.

[38] R. M. Lynden-Bell and J. C. Rasaiah. "From hydrophobic to hydrophilic behaviour: A simulation study of solvation entropy and free energy of simple solutes". In: *The Journal of Chemical Physics* 107.6 (1997), p. 1981. ISSN: 00219606. DOI: 10.1063/1.474550. URL: http://link.aip.org/link/JCPSA6/v107/i6/p1981/s1\&Agg=doi.

[39] Sergio Murgia, Maura Monduzzi, and Barry W. Ninham. "Hofmeister effects in cationic microemulsions". In: *Current Opinion in Colloid & Interface Science* 9.1-2 (Aug. 2004), pp. 102–106. ISSN: 13590294. DOI: 10.1016/j.cocis.2004.05.012. URL: http://linkinghub.elsevier.com/retrieve/pii/S1359029404000391.

[40] Roland R. Netz and Dominik Horinek. "Progress in Modeling of Ion Effects at the Vapor/Water Interface". en. In: (Apr. 2012). URL: http://www.annualreviews.org/doi/full/10.1146/annurev-physchem-032511-143813?url_ver=Z39.88-2003\&rfr_id=ori:rid:crossref.org\&rfr_dat=cr_pub=pubmed.

[41] Joyce Noah-Vanhoucke and Phillip L. Geissler. "On the fluctuations that drive small ions toward, and away from, interfaces between polar liquids and their vapors". In: *Proceedings of the National Academy of Sciences* 106.36 (2009), pp. 15125 –15130. DOI: 10.1073/pnas.0905168106. URL: http://www.pnas.org/content/106/36/15125.abstracthttp://www.pnas.org/content/106/36/15125.abstract?sid=296c6dc6-fd08-4d47-b92f-d7c6fea15d08http://www.pnas.org/content/106/36/15125.full.pdf.

[42] Joyce Noah-Vanhoucke, Jared D. Smith, and Phillip L. Geissler. "Statistical mechanics of sum frequency generation spectroscopy for the liquidvapor interface of dilute aqueous salt solutions". In: *Chemical Physics Letters* 470.1-3 (Feb. 2009), pp. 21–27. ISSN: 00092614. DOI: 10.1016/j.cplett.2009.01.028. URL: http://linkinghub.elsevier.com/retrieve/pii/S0009261409000311.

[43] Anne Willem Omta et al. "Negligible effect of ions on the hydrogen-bond structure in liquid water." In: *Science (New York, N.Y.)* 301.5631 (July 2003), pp. 347–9. ISSN: 1095-9203. DOI: 10.1126/science.1084801. URL: http://www.ncbi.nlm.nih.gov/pubmed/12869755.

[44] Lars Onsager and Nicholas Samaras. "The Surface Tension of Debye-Huckel Electrolytes". In: *Journal of Chemical Physics* 2.8 (1934), pp. 528–536.

[45] Dale E. Otten, Poul B. Petersen, and Richard J. Saykally. "Observation of nitrate ions at the air/water interface by UV-second harmonic generation". In: *Chemical Physics Letters* 449.4-6 (Dec. 2007), pp. 261–265. ISSN: 00092614. DOI: 10.1016/j.cplett.2007.10.081. URL: http://linkinghub.elsevier.com/retrieve/pii/S0009261407014017.

[46] Dale E Otten et al. "Elucidating the mechanism of selective ion adsorption to the liquid water surface". In: *Proceedings of the National Academy of Sciences* 109.8 (Feb. 2012), pp. 3190–3190. ISSN: 0027-8424. DOI: 10.1073/pnas.1201349109. URL: http://www.pnas.org/cgi/doi/10.1073/pnas.1201349109.

[47] Amish J Patel et al. "Extended surfaces modulate hydrophobic interactions of neighboring solutes". In: *PNAS* 108.43 (2011), pp. 17678–17683. DOI: 10.1073/pnas.1110703108/-/DCSupplemental.www.pnas.org/cgi/doi/10.1073/pnas.1110703108.

[48] Poul B Petersen and Richard J Saykally. "Adsorption of ions to the surface of dilute electrolyte solutions: the Jones-Ray effect revisited." In: *Journal of the American Chemical Society* 127.44 (Nov. 2005), pp. 15446–52. ISSN: 0002-7863. DOI: 10.1021/ja053224w. URL: http://www.ncbi.nlm.nih.gov/pubmed/16262408.

[49] Poul B Petersen and Richard J Saykally. "Probing the Interfacial Structure of Aqueous Electrolytes with Femtosecond Second Harmonic Generation Spectroscopy". In: *J. Phys. Chem. B* 110 (2006), pp. 14060–14073.

[50] Poul B Petersen et al. "Spectroscopy and MD Simulations of Sodium Thiocyanide". In: *Langmuir* (2005), pp. 10915–10921.

[51] J. C. Rasaiah and R. M. Lynden-Bell. "Computer simulation studies of the structure and dynamics of ions and non-polar solutes in water". In: *Philosophical Transactions of the Royal Society A: Mathematical, Physical and Engineering Sciences* 359.1785 (Aug. 2001), pp. 1545–1574. ISSN: 1364-503X. DOI: 10.1098/rsta.2001.0865. URL: http://rsta.royalsocietypublishing.org/cgi/doi/10.1098/rsta.2001.0865.

[52] Pengyu Ren and Jay W. Ponder. "Polarizable Atomic Multipole Water Model for Molecular Mechanics Simulation". In: *The Journal of Physical Chemistry B* 107.24 (June 2003), pp. 5933–5947. ISSN: 1520-6106. DOI: 10.1021/jp027815+. URL: http://pubs.acs.org/doi/abs/10.1021/jp027815+.

[53] M.H.B.M. Shariff. "A constrained conjugate gradient method and the solution of linear equations". In: *Computers & Mathematics with Applications* 30.11 (Dec. 1995), pp. 25–37. ISSN: 08981221. DOI: 10.1016/0898-1221(95)00161-Q. URL: http://linkinghub.elsevier.com/retrieve/pii/089812219500161Q.

[54] Jonathan Richard Shewchuk. "An Introduction to the Conjugate Gradient Method Without the Agonizing Pain". In: *Published privately on web* (1994).

[55] Michael R Shirts and John D Chodera. "Statistically optimal analysis of samples from multiple equilibrium states." In: *The Journal of chemical physics* 129.12 (Oct. 2008), p. 124105. ISSN: 1089-7690. DOI: 10.1063/1.2978177. URL: http://www.pubmedcentral.nih.gov/articlerender.fcgi?artid=2671659\&tool=pmcentrez\&rendertype=abstract.

[56] Jared D Smith, Richard J Saykally, and Phillip L Geissler. "The effects of dissolved halide anions on hydrogen bonding in liquid water." In: *Journal of the American Chemical Society* 129.45 (Nov. 2007), pp. 13847–56. ISSN: 0002-7863. DOI: 10.1021/ja071933z. URL: http://www.ncbi.nlm.nih.gov/pubmed/17958418.

[57] Xueyu Song and David Chandler. "Dielectric solvation dynamics of molecules of arbitrary shape and charge distribution". In: *Journal of Chemical Physics* 108.6 (1998), pp. 4–10.

[58] Xueyu Song, David Chandler, and R. a. Marcus. "Gaussian Field Model of Dielectric Solvation Dynamics". In: *The Journal of Physical Chemistry* 100.29 (Jan. 1996), pp. 11954–11959. ISSN: 0022-3654. DOI: 10.1021/jp960887e. URL: http://pubs.acs.org/doi/abs/10.1021/jp960887e.

[59] Abraham C Stern et al. "Thermodynamics of iodide adsorption at the instantaneous air-water interface." In: *The Journal of chemical physics* 138.11 (Mar. 2013), p. 114709. ISSN: 1089-7690. DOI: 10.1063/1.4794688. URL: http://www.ncbi.nlm.nih.gov/pubmed/23534655.

[60] Suriyanarayanan Vaikuntanathan, Patrick R. Shaffer, and Phillip L. Geissler. "Adsorption of solutes at liquidvapor interfaces: insights from lattice gas models". In: *Faraday Discussions* 160 (2013), p. 63. ISSN: 1359-6640. DOI: 10.1039/c2fd20106b. URL: http://xlink.rsc.org/?DOI=c2fd20106b.

[61] Patrick Stephen Varilly. "Fluctuations in Water and their RElation to the Hydrophobic Effect". PhD thesis. University of California, Berkeley, 2011.

[62] Lubos Vrbka et al. "Propensity of soft ions for the air/water interface". In: *Current Opinion in Colloid & Interface Science* 9.1-2 (Aug. 2004), pp. 67–73. ISSN: 13590294. DOI: 10.1016/j.cocis.2004.05.028. URL: http://linkinghub.elsevier.com/retrieve/pii/S1359029404000330.

[63] Adam P Willard and David Chandler. "Instantaneous liquid interfaces." In: *The journal of physical chemistry. B* 114.5 (Feb. 2010), pp. 1954–8. ISSN: 1520-5207. DOI: 10.1021/jp909219k. URL: http://www.pubmedcentral.nih.gov/articlerender.fcgi?artid=2834420\&tool=pmcentrez\&rendertype=abstract.

[64] Michael a. Wilson, Andrew Pohorille, and Lawrence R. Pratt. "Comment on Study on the liquidvapor interface of water. I. Simulation results of thermodynamic properties and orientational structure". In: *The Journal of Chemical Physics* 90.9 (1989), p. 5211. ISSN: 00219606. DOI: 10.1063/1.456536. URL: http://link.aip.org/link/JCPSA6/v90/i9/p5211/s1\&Agg=doi.

[65] Yanjie Zhang and Paul S Cremer. "Interactions between macromolecules and ions: The Hofmeister series." In: *Current opinion in chemical biology* 10.6 (Dec. 2006), pp. 658–63. ISSN: 1367-5931. DOI: 10.1016/j.cbpa.2006.09.020. URL: http://www.ncbi.nlm.nih.gov/pubmed/17035073.